2023

A Theoretical Study of Elementary Processes in Interstellar Plasma

Joshua Forer
University of Central Florida

A THEORETICAL STUDY OF ELEMENTARY PROCESSES IN INTERSTELLAR PLASMA

by

JOSHUA FORER
B.S. University of Miami, 2017

A dissertation submitted in fulfilment of the requirements
for the degree of Doctor of Philosophy
in the Department of Physics
in the College of Sciences
at the Universty of Central Florida
in Orlando, FL, USA
and
in the Institut des Sciences Moléculaires
in the École Doctorale des Sciences Chimiques
at the Universté de Bordeaux
in Talence, France

Fall Term
2023

Major Professors: Viatcheslav Kokoouline and Thierry Stoecklin

ABSTRACT

Interstellar plasma — interstellar clouds in particular — play an important role in determining the structure and evolution of galaxies. Understanding the time evolution of such plasmas requires knowledge of the chemical processes that drive their dynamics. Two processes are studied in this dissertation: radiative electron attachment (REA) via dipole-bound states (DBSs) and dissociative recombination (DR). Of the several hundred molecules detected in the interstellar medium, only eight anions have been detected: CN^-, C_3N^-, C_5N^-, C_7N^-, C_4H^-, C_6H^-, C_8H^-, and $C_{10}H^-$. Their production mechanism is not well known; REA was suggested as a possible formation pathway, but previous theoretical studies have found that REA rate coefficients were too low to explain the formation of CN^-, C_3N^-, and C_5N^-. It was later suggested that including DBSs — an electron weakly bound at a large distance to the large dipole moment of a neutral molecule — could appreciably enhance the REA rate coefficients. The first portion of this study is dedicated to investigating the role of the large dipole moment of rotating C_3N using an accurate *ab initio* approach with electronic and rotational resolution. DBS wavefunctions of C_3N^- are calculated and used to obtain REA cross sections that produce even smaller rate coefficients, suggesting that C_3N^- is efficiently formed by a different process. The second part of this study investigates DR in the difficult case of molecules with low-lying eletronic resonances, although these are not necessary for the approach. An approach to treat both direct and indirect mechanisms of DR in a diatomic ion with electronic, vibrational, and rotational resolution using R-matrix scattering calculations, frame transformation theory, and multichannel quantum defect theory is presented and applied to the CH^+ and CF^+ molecular ions at low collision energies. The calculated CH^+ cross sections agree well with recent rotationally state-resolved experimental results and overall better than previous theoretical results. The calculated CF^+ cross sections agree well with experimental results, although these do not have rotational resolution, and overall better than previous theoretical results at low energies. Additionally, the method can study rovibronic (de-)excitation — a process in compe-

tition with DR. These are calculated and compared to previous theoretical calculations for CH^+, which which our results agree well with the exception of dipole-driven rotational excitation cross sections. This discrepancy is tentatively attibuted to negelcting the contribution of higher partial waves in the description of the incident electron, which will be incorporated in future studies.

ACKNOWLEDGEMENTS

Committee members:

Prof. Viatcheslav Kokoouline	Dr. Thierry Stoecklin
Prof. Luca Argenti	Prof. Mehdi Ayouz
Prof. Li Fang	Dr. Alexandre Faure
Prof. Ann E. Orel	Prof. Dr. Roland Wester

To my committee members for agreeing to be a part of this, for reading and re-reading my drafts, and for their helpful feedback. To OldA Novotný, Holger Kreckel, and Andreas Wolf from the Max-Planck-Institut für Kernphysik (MPIK) in Heidelberg, to Abel Kalosi and Daniel Paul, from the MPIK and Columbia University for providing us with experimental data as well as for helpful discussions with them and with Ioan F. Schneider (Le Havre) and Zsolt J. Mezei (Debrecen). To Esperanza Soto Arcino and Nikitta Campbell at UCF for basically preventing me from accidentally un-enrolling myself, for keeping me and so many grad students on track to graduate, and to the rest of the administration at UCF and the University of Bordeaux that helped me formalize my joint tutelage between the two schools and made this possible for future students at UCF to pursue. To Isaac Yuen, Nicolas Douguet, and Samantha Fonseca dos Santos for helping me get started with my research and get over the initial roadblocks I encountered. To Conner Penson for taking the lead on the photoionization project I was supposed to do, collaborating with me, providing useful feedback on my code and my dissertation. To Philippe Halvick and Miguel Lara-Moreno for helping me get used running `Molpro` and Thierry's many F77 codes. I would have spent a lot more time during my year in Bordeaux figuring some of that out on my own. To all the other members of the Institut des Sciences Moléculaires at the University of Bordeaux for all the time we spent together and insightful conversations about research perspectives and their experiences in Europe and abroad. To Jeoffrey Boffelli for managing to work with my code to study CF^+ and helping me slowly change it for the better so that others might use it more easily. To Daniel Wolf

Savin helping me scramble to write the proposal that would win me an NSF postdoctoral fellowship at Columbia University in the city of New York. To Andrea Prestwich for helping me figure out all of the NSF fellowship details and looking out for me before a looming government shutdown. To the support from the National Science Foundation, Grant Nos. 2110279 (UCF) and 2102187 (Purdue). To the Fulbright-University of Bordeaux Doctoral Research Award and the team at the Franco-American Fulbright commission. To all the friends I made in Orlando, in Bordeaux, and at the many conferences I attended. To all the students I had the (mostly) pleasure of teaching in Orlando who helped me become a better communicator, mentor, and teacher. Even when it was challenging, it was worth it to me. To all the other graduate students in the my class, as well as those above and below me at both Universities, many of whom have become some of my best friends. To Andrew Leeds for helping me find such a great place to live in NYC for my postdoc appointment with Daniel Savin. To Slava Kokoouline and Thierry Stoecklin especially for being excellent supervisors, letting me work in a way that I like, and for telling me about opportunities like the Fulbright and NSF fellowships I received (all 25 other graduate programs I applied to over a semester and a half rejected me so, at the time, I never imagined I'd have as good of an experience as I've had, and I can't really imagine my experience having been much better. Thanks again to Slava for asking me to do research with him despite not responding to my initial email that I sent when I was scoping out the UCF grad program before attending). To Eric Rende and Tyler Campbell for being great friends and roomates across my many housing situations. To Nadia Lezzar for helping guarantee my amazing apartment in Bordeaux when no one else could help me. To Ashlyn Schwartz and her family inviting me in, making me feel like family, and helping me out with general PhD issues and the complicated French administration. To Adri Messineo for letting me stay over for weeks in Bordeaux when I didn't have my own appartment there anymore. To Rachel Weinstein and her family for having me over for months during the pandemic, so that I could more easily focus on my classes, teaching, and research. I hear that it cost more than a grant just to feed me. To Elizabeth Knapp for helping me stay sane during the pandemic with our

weekly online TTRPG meetups. To Anna-Lane Moerland for housing me for months when Eric and I lost our apartment that he was mostly paying for. To Alex Rimany for supporting me during all of my crazy housing moves in the few months in Orlando leading up to my dissertation defense. To my family in the US, France, and Switzerland for all of the help and support they've given and continue to give me.

Thank you all so much.

TABLE OF CONTENTS

LIST OF FIGURES

LIST OF TABLES

LIST OF ACRONYMS, INITIALISMS, AND TRUNCATED WORDS

Acronym / Initialism / Word	Name
CAP	complex absorbing potential
CB	Coulomb-Born
CCEP	[MQDT] closed-channel elimination procedure
CRIR	cosmic-ray ionization rate of atomic hydrogen
CSR	Cryogenic Storage Ring
DBS	dipole-bound state
DR	dissociative recombination
DSS	dipole scattering state
FCI	full configuration interaction
ISM	interstellar medium
ISRF	interstellar radiation field
LHS	left-hand-side
MQDT	multichannel quantum defect theory
MRCI	multireference configuration interaction
REA	radiative electron attachment
RFT	rotational frame transformation
RHS	right-hand-side
TSR	Test Storage Ring
VFT	vibrational frame transformation
WKB	Wentzel-Kramers-Brillouin [approximation]
irrep	irreducible representation

LIST OF UNITS

Symbol	Name	Value	Units	Type
Å	ångström	10^{-10}	m	distance
eV	electron volt	$1.602\ 176\ 634 \times 10^{-19}$	J	energy
E_h	Hartree energy	$4.359\ 744\ 722\ 2071(85) \times 10^{-18}$	J	energy
		27.211 386 245 988(53)	eV	energy
Ry	Rydberg	$E_h/2$ = 13.605 693 122 944(26)	eV	energy

All values sourced from the 2018 CODATA recommended values.

LIST OF PHYSICAL CONSTANTS

Symbol	Name	Value	Units
ϵ_0	permittivity of free space	8.854 187 8128(13)$\times 10^{-17}$	F·m^{-1}
h	Planck constant	6.626 070 15$\times 10^{-34}$	J·s
$\hbar$	reduced Planck constant	$h/(2\pi)$ = 1.054 571 817$\cdots \times 10^{-34}$	J·s
m_e	electron mass	$9.1093837015(28) \times 10^{-31}$	kg
e	electron/elementary charge	1.602 176 634$\times 10^{-19}$	C
c	speed of light in a vacuum	299 792 458	m·s
$\mathcal{R}$	Rydberg constant	$\frac{m_e e^4}{8\varepsilon_0^2 h^2 n^2}$ =10 973 731.568 160(21)	m^{-1}
k_B, k	Boltzmann constant	1.380649×10^{-23}	m^2·kg· s^{-2}·K^{-1}
a_0	Bohr radius	5.291 772 109 03(80)$\times 10^{-11}$	m

All values sourced from the 2018 CODATA recommended values.

CHAPTER 1: INTRODUCTION

Of the four fundamental phases of matter, *plasma* is the most commonly occurring in the universe. The term plasma can be somewhat context-dependent, but a general definition of plasma is a phase of matter in which there is a significant proportion of charged particles — it is appreciably ionized. Stars, solar wind, and the interstellar medium (ISM), the matter between the star systems of a galaxy, are considered plasmas. As plasmas become increasingly charged, they are governed more and more by electromagnetic fields at microscopic and macroscopic levels. While there are naturally occurring plasmas on our planet, e.g., the appropriately named ionosphere, plasma has become an increasingly prevalent aspect of our everyday lives. Plasma technologies are rapidly developing; this includes plasma etching used in microelectronics fabrication, fusion reactor development for sustainable energy, environmental pollutant removal, plasma televisions, and even lights to name a few. Although aspects of the theory and work presented in this dissertation are applicable to other plasmas, the main focus here is on interstellar plasma. In particular, two processes are studied in this dissertation that take place in interstellar clouds — clouds of gas and dust with varying degrees of ionization found in the ISM spanning several orders of magnitude in size. These processes are dissociative recombination (DR) and radiative electron attachment (REA), both described later.

Interstellar clouds can collapse — an early process in star formation, which determines the structure and evolution of galaxies[1]. Such gas clouds must be cold enough to allow their self-gravity to overcome their thermal pressure. Much like how the Earth as its own magnetic field, galaxies have their own magnetic field. Interstellar clouds must also have a low enough ionization fraction such that they are significantly decoupled from the Galactic magnetic field so that they may collapse to form stars[2]. Diffuse interstellar clouds are an important early stage in star formation.

Diffuse clouds can transition from being mostly atomic to being increasingly molecular.

This transition is mapped by the abundance of H_2, which is expressed as the *molecular fraction*,

$$f_{H_2} = \frac{2n(H_2)}{2n(H_2) + n(H)}, \tag{1.1}$$

where $n(H)$ and $n(H_2)$ are the number densities of H and H_2, respectively[3]. H_2, however, is a neutral and symmetric molecule. Despite being the most abundant molecule in the ISM, its lack of a permanent dipole moment makes it difficult to detect[4]. Therefore, tracer molecules are used to infer f_{H_2} indirectly. To interpret the observed column densities of any species, one must understand its chemical network within diffuse interstellar clouds.

Diffuse interstellar clouds typically have a temperature between 40 K and 130 K[5]. At such low temperature, species do not collide with enough energy to overcome typical neutral-neutral potential energy collision barriers. Instead, barrierless ion-neutral collisions drive the chemical evolution of diffuse interstellar clouds. The presence of ionized species in diffuse clouds can be traced back to ionization of atomic (H) or molecular (H_2) hydrogen by cosmic rays — high-energy particles travelling at relativistic speeds, or by the ionization of heavier species photons from the interstellar radiation field (ISRF). Because of this, the abundance of various tracer molecules can be used to constraint the cosmic-ray ionization rate (CRIR) of atomic hydrogen (ζ_H) and the ISRF. The relative abundances of OH^+, H_2O^+, and H_3O^+, for example, can be used to constrain ζ_H, while the ISRF could be constrained by observations of HCl and some of its associated ions, HCl^+ and H_2Cl^+.

Exothermic neutral-neutral reactions still exist. Atomic fluorine (F) collides exothermically with molecular hydrogen, creating HF which is dominant fluorine reservoir in molecular clouds[6,7]. The main destruction mechanism of interstellar HF is collisions with C^+:

$$HF + C^+ \longrightarrow CF^+ H. \tag{1.2}$$

One of the important destruction mechanisms for the above-mentioned ions is DR.

As molecular clouds become more molecular, they can become more dense as they collapse. Such clouds typically have much lower temperatures — around 10 K — and have much more complex chemical networks[8]. Of the multitude of detected molecules in the ISM, only eight are negatively charged[9–15]: CN^-, C_3N^-, C_5N^-, C_7N^-, C_4H^-, C_6H^-, C_8H^-, and $C_{10}H^-$. Negative molecular ions can react with, e.g., hydrogen, via associative detachment[16], e.g.

$$C_nN^- + H \longrightarrow HC_nN + e^- \tag{1.3}$$

The formation mechanism of negative molecular ions in interstellar clouds is still unknown.

This dissertation (i) investigates the plausibility of low-energy REA forming negative molecule ions in the case of C_3N to form C_3N^- and (ii) describes a new method to study low-energy DR, applied to CH^+ and CF^+, that is suitable for several diatomic molecules and will be developed further to be applicable to polyatomic species.

Negative molecular ions

Negative molecular ions have been proposed[17–21] among several candidates as being, at least partially, responsible responsible for the diffuse interstellar bands — broad absorption-spectrum features of astronomical bodies of generally unknown origin. The destruction of negative molecular ions is better understood than their formation in interstellar media. The rate coefficients of collisions between observed C_nH^- anions and atomic hydrogen, nitrogen, and oxygen has been studied experimentally[21]: collisions with atomic hydrogen are very efficient, whereas collisions with atomic nitrogen could form observed C_nN^- ions. Although carbon chains tend to be more reactive in collision with O than N, production of CO is much more favorable than any C_nO^- (still unobserved) production pathway.

Another proposed formation pathway of C_nN^- is radiative electron attachment,

$$C_nN + e^- \longrightarrow C_nN^- + \hbar\omega. \tag{1.4}$$

An electron encounters a neutral molecule, after which the complex may release energy via photon emission to relax to a low-energy state of the molecular anion. Previous calculations[22–25], however, have demonstrated that REA rates are too low to explain the observed abundance of CN^-, C_3N^-, and C_5N^-. It was then suggested that REA could occur via a "doorway" weakly bound dipole state[26] — also known as dipole-bound states (DBSs). Fermi and Teller[27] showed that the interaction between a point charge and a point-dipole for dipole values larger than the critical value of $\sim$ 0.65 atomic units (au) supports infinitely many DBSs. Molecular effects increase the critical value required to support DBSs and reduce the number of DBSs to a small, finite amount — often just one electronic state, which of course can host several vibrational or rotational levels. The minimum dipole moment required to form stable dipole-bound anions of common closed-shell molecules has been experimentally observed to range between $\sim$0.79–0.98 au.

Over time, the effects of vibration[28] and rotation[29,30] of the neutral molecule on the DBS have been investigated, showing that the critical moment for a rotating dipole is larger than that of a stationary dipole. This suggest that CN, with a dipole moment of $\sim$0.57 au[31], is not expected to produce CN^- via REA through DBSs. C_3N and C_3N^- were selected to be the subjects of this study because C_3N^- has been detected in the ISM[9] and a DBS of C_3N^- was observed experimentally in the ion-trap experiment of Simpson et al.[26]. A fully quantum study of REA through a DBS that includes both the rotation of the molecule and the short-range part of the electron-molecule potential is missing in the literature. This study aims to fill this void and determine if including C_3N^- DBSs significantly enhances the REA rate coefficients to explain the perplexing abundance of C_3N^- in interstellar media.

Dissociative recombination

DR describes the process whereby a molecular cation collides with an electron and dissociates. It is often the main destruction mechanism of molecular cations in the ISM. Laboratory measurements, in general, are quite limited and can only produce a small amount of the data needed to model interstellar chemistry. Hence, theoretical methods can often fill the gaps left from experimental results or lack thereof. Only recently has the Cryogenic Storage Ring (CSR, 2016[32]) come online, carrying out groundbreaking experiments that can measure the DR rate coefficient for ions in their ground state. Previous measurements, at best, were made at higher temperatures where the target ions populated several excited states. Other experiments were carried out at temperatures where the ions are expected to have been rotationally and vibrationally excited. This is an important distinction because the collisional rates in interstellar clouds are so low compared to the spontaneous radiative decay rate of these molecular ions that electrons are expected to collide with molecular ions in their ground rotational, vibrational, and electronic states. Measurements of the DR of HeH^+ made at the CSR found a discrepancy of about an order of magnitude at lower electron energies relevant for diffuse interstellar clouds[33]. An order-of-magnitude difference in the DR rate of OH^+, for example, would result in an order-of-magnitude difference in the inferred value of ζ_H[34].

Despite recent experimental advances, however, there still remain several challenges in obtaining experimental ground-state DR rate coefficients. Cooling some molecules with small dipole moments or rotational constants becomes difficult because the ions can only be stored for a finite amount of time, during which they are expected to cool radiatively. In cases like these, theory may be used to deconvolve experimental rate coefficient measurements or may even be used instead of experimental measurements.

Theoretical DR treatments, however, also have significant limitations. Two DR mechanisms exist: the *direct* mechanism and the *indirect* mechanism. In direct DR, the incident electron is captured into a dissociative states of the neutral molecule. Indirect DR describes the process by

which an electron is captured into a Rydberg states of the neutral molecule and then transitions to a dissociative resonant state. Either the indirect or the direct mechanism dominates the DR process in many cases for some given energy range. Their relative importance, however, is often not known *a priori*, although investigating the electronic structure of the target ion may give some insight. Additionally, both mechanisms may interfere and have a significant impact on the observed rate coefficients.

Most theoretical DR treatments do not include both mechanisms simultaneously or do not have rotational resolution. For gas-phase chemistry in diffuse interstellar clouds, these approximations may not be justified. The low kinetic temperatures of diffuse clouds (40–130 K) translates to electrons impinging on molecular ions with kinetic energies of about 3.5×10^{-3}–1.1×10^{-2} eV[5]), which is typically considered low-energy. At and below such low energies, the rotational structure of the target ion may be the most important in determining DR cross sections and, therefore, rate coefficients. Systems that host a dominant indirect mechanism are typically most influenced by the rotational structure of the target ion[35,36].

The DR of two molecular ions will be presented: the DR of CH^+, first detected in the ISM by Douglas and Herzberg[37], and CF^+, first detected in the ISM by Neufeld et al.[38]. The former is an excellent candidate for our developed method. It is an open shell ion with low-lying electronic resonances, yet its electronic structure is not as complex as other diatomics. The DR of such ions is typically difficult to study theoretically. Additionally, accurate state-resolved measurements of the DR of CH^+ were made at the CSR by Paul et al.[39], who were able to resolve DR rate coefficients from the ground rotational, vibrational, and electronic state of CH^+. Their results can serve as a benchmark to our theoretical method applied to CH^+. CF^+ has a similar electronic structure to that of CH^+, although it is slightly more complicated. Potential energy curves of both ions are shown in Figure 1.1 This molecule has no recent experimental measurements that are comparable to those of CH^+Paul et al.[39], yet its gas-phase chemistry is important to the fluorine chemistry of interstellar clouds. Applying our method to CF^+ will serve as a good test case for a similar molecular ion with

a slightly more complicated electronic structure.

First-principles fully quantum DR theories have only recently been able to accurately describe the DR process accounting for all non-spin degrees of freedom: electronic, vibrational, and rotational. Recently, ab initio theory managed to successfully reproduce all details of the experimental DR cross sections measured at the CSR[33] for the benchmark system, HeH^+[40,41]. However, for diatomic ions with a more complex electronic structure, theory is still not as accurate as in the case of HeH^+. DR of molecular ions with no electronic resonances at low collision energies is dominated by the indirect mechanism. In such a case, theoretical approach based on quantum defect theory[42–44,41,40] offers a good description of the process. For molecular ions having one or just a few electronic resonances at low scattering energies — likely dominated by the direct DR mechanism — time-dependent[45–48] and time-independent[49–51,35,52–58] approaches represent the process well and provide generally accurate (relative to experimental results) rate coefficients, with the exception of certain molecular ions, e.g., CH^+.

CH^+ belongs to a class of ions with low-lying electronic states — creating low-energy electronic resonances that are excitable by low-energy electrons — for which the above-referenced theoretical methods are less appropriate. This dissertation describes a method that can treat such molecular ions, simultaneously including the direct and indirect mechanisms, although it can also be applied to other ions where the relevant importance of the DR mechanisms are already known. It implements the R-matrix method to perform electron-ion scattering calculations; rotational and vibrational frame transformations to include electronic, vibrational, and rotational degrees of freedom; and multichannel quantum-defect theory (MQDT) to implicitly include Rydberg resonances produced by closed excitation channels.

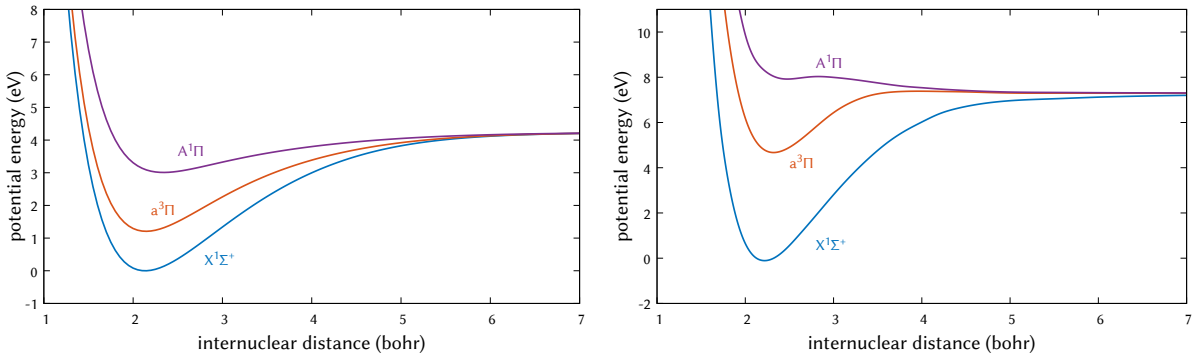

Figure 1.1: Lowest three potential energy curves of the CH^+ (left) and CF^+ (right) ions.

Terminology — atomic units

Atomic units, also known as Hartree atomic units, will be denoted as "au". This is a system of units defined by setting the reduced Planck constant ($\hbar = h/2\pi$), the electron charge (e), the electron rest mass (m_e), and the Coulomb constant ($k_e = (4\pi\epsilon_0)^{-1}$) to unity (1). The bohr radius, a_0, is the atomic unit of length and will often be referred to as a "bohr". As an example, the time-dependent Schrödinger equation in SI units,

$$-\frac{\hbar^2}{2m_e}\nabla^2\phi(\vec{r},t) + V(\vec{r})\phi(\vec{r},t) = i\hbar\frac{\partial\phi}{\partial t}(\vec{r},t), \tag{1.5}$$

takes the following form in atomic units,

$$-\frac{1}{2}\nabla^2\phi(\vec{r},t) + V(\vec{r})\phi(\vec{r},t) = i\frac{\partial\phi}{\partial t}(\vec{r},t). \tag{1.6}$$

Atomic units are assumed for the remainder of this manuscript, unless otherwise specified.

CHAPTER 2: PRELIMINARY THEORY

Scattering equations

Scattering theory, for collisions between non-classical objects like electrons and molecules, determines the probability that certain processes will occur and the final internal states of the collision partners. Classically, scattering theory is deterministic — the final states of the colliding particles are determined entirely by the initial conditions of the system. We can determine the size of classical objects by measuring them, but this concept is somewhat lost in the quantum regime. Instead, we use another concept that exists in classical mechanics: the *cross section*. Cross sections, classically, are the area that two colliding bodies must intersect to hit each other. In the context of electron-molecule collisions, cross sections are an area measurement of the probability rate of a process occurring, given some initial configuration of the collision partners.

The possible processes can be separated into two categories: *elastic* and *inelastic* collisions. The internal states of the electron and the molecule are both left unchanged in elastic collisions. Inelastic collisions define the case where the internal states of the colliders are altered. This could mean just a change in energy of each collider ((de-)excitation) or even a change in particle (e.g., photoionization).

Elastic scattering of neutral particles — single channel

Suppose some particle of mass m experiences a short-range potential $V(\vec{r})$, typically given by the constraint

$$\lim_{r\to\infty} r^2 V(\vec{r}) = 0. \tag{2.1}$$

The solution to the time-independent Schrödinger equation (given in atomic units),

$$\left[\frac{-1}{2m}\nabla^2 + V(\vec{r})\right]\psi_k(\vec{r}) = E_k\psi_k(\vec{r}), \tag{2.2}$$

can be chosen to behave asymptotically as

$$\psi(\vec{r}) \xrightarrow{r\to\infty} e^{ikz} + f(\theta,\phi)\frac{e^{ikr}}{r}, \tag{2.3}$$

i.e., the typical superposition of an incoming plane-wave moving along $\hat{z}$ and an outgoing spherical wave modulated by some *scattering amplitude* $f(\theta,\phi)$ (as shown in Figure. 2.1), where θ and ϕ are the polar and azimuthal angles, respectively. If the potential is radially symmetric, i.e. $V(\vec{r}) =$

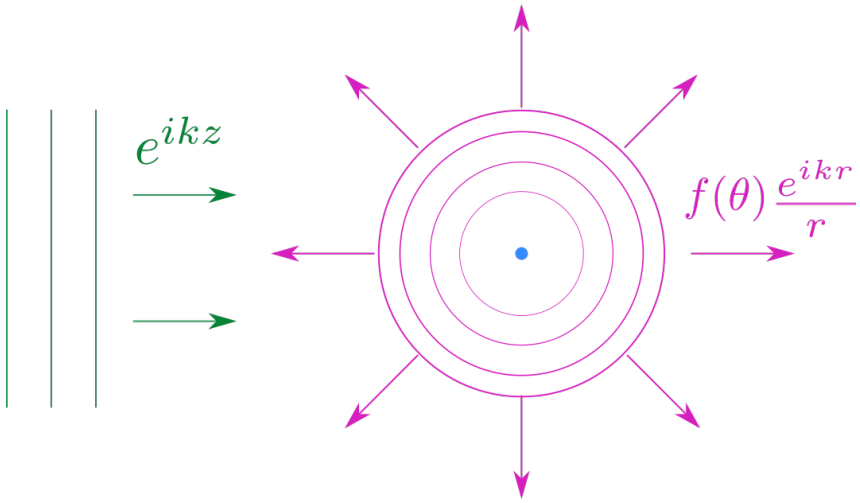

Figure 2.1: Sketch of the incoming plane-wave and outgoing spherical-wave describing the asymptotic behavior of a collision.

$V(r)$, the orbital angular momentum,

$$\begin{aligned} \hat{L} &= \vec{r} \times \hat{p}, \\ \hat{L}^2 Y_l^m(\theta,\phi) &= l(l+1)Y_l^m(\theta,\phi), && l \in \mathbb{N}_0 \\ \hat{L}_z Y_l^m(\theta,\phi) &= m Y_l^m(\theta,\phi) && m \in \mathbb{Z},\ |m| \le l \end{aligned} \tag{2.4}$$

is conserved and the asymptotic form of the wavefunction (2.3) can be expanded in the complete orthonormal basis of *spherical harmonics* $\left(Y_l^m(\theta,\phi)\right)$, which are the simultaneous eigenfunctions

of $\widehat{L}^2$ and one of its components ($\widehat{L}_z$ in this case, chosen to align with the incoming plane wave).

The spherical harmonics have the well-known form, given by (B.21). The orbital angular momentum quantum number (l) and the its projection on the $\widehat{z}$ axis (m), together, define each *partial wave* used in the expansion of (2.3):

$$\psi(\vec{r}) = \sum_{l=0}^{\infty} A_l \frac{\phi_l(r)}{r} P_l(cos(\theta)), \tag{2.5}$$

where $\phi(r)$ is a radial wavefunction, and $P_l(cos(\theta))$ are the *Legendre polynomials* (associated Legendre polynomials of order 0, given in B.10), and A_l is an expansion coefficient. Partial wave expansions typically converge quickly for low-energy electron-molecule collisions, except for cases where the target has a large permanent dipole moment that strongly couples channels differing in l by unity. Dealing with such cases for, e.g., rotational excitation calculations, will be briefly discussed later. The expression in equation (2.5) has no azimuthal dependence because both the Schrödinger equation and the scattering wavefunction's boundary conditions have azimuthal symmetry. The scattering wavefunction has no dependence on ϕ, i.e., $m = 0$, so the spherical harmonics reduce to Legendre polynomials multiplied by the $\sqrt{(2l+1)/(4\pi)}$ normalization factor. The time-independent Schrödinger equation (2.2) for a solution of the form given by (2.5), in spherical coordinates, reduces to the following, in atomic units

$$\left[-\frac{d}{dr^2} + \frac{l(l+1)}{r^2} + V(r)\right] \phi(r) = k^2 \phi(r), \quad k = \sqrt{2mE}. \tag{2.6}$$

Two linearly independent solutions to (2.6) in the event that $V(r) = 0$ are the *Riccati-Bessel functions* (B.8) of the first and second kind. If we suppose that the potential falls off faster than 1/r, i.e. $(V(r) \propto 1/r^{\alpha}, \alpha > 1)$, and is nonzero, the solution to (2.6) takes the form[59]

$$\phi(r) \overset{r\to\infty}{\propto} \sin\left(kr - \frac{l\pi}{2} + \delta_l\right). \tag{2.7}$$

The expansion coefficients, A_l, of (2.5) must allow for the solution to maintain the form (2.3) at large distances. Given that the incoming wave e^{ikz} has no azimuthal dependence, it can also be expressed in terms of partial waves[60]

$$e^{ikz} = \sum_{l=0}^{\infty}(2l+1)i^l j_l(kr)P_l(cos(\theta)). \tag{2.8}$$

Looking at the form of (B.8, 2.7, 2.8), we can determine the form of the expansion coefficients in (2.5)

$$A_l \propto \frac{1}{k}(2l+1)i^l e^{i\delta_l}, \tag{2.9}$$

where δ_l is the same constant as in (2.7): the *scattering phase shift*. These phase shifts, functions of l and k, are important quantities that contain information information about the collision. There is no general solution for δ_l; one must solve the specific Schrödinger equation to obtain them. Combining (2.5), (2.7), and (2.9), the full wavefunction for each partial wave takes the following asymptotic form

$$\begin{aligned}\psi_l(\vec{r}) &\overset{r\to\infty}{\propto} \frac{(2l+1)}{kr}P_l(cos(\theta))i^l e^{i\delta_l}\sin\left(kr - \frac{l\pi}{2} + \delta_l\right) \\ &\overset{r\to\infty}{\propto} \frac{(2l+1)}{2ikr}P_l(cos(\theta))\left(e^{2i\delta_l}e^{ikr} + (-1)^{l+1}e^{-ikr}\right),\end{aligned} \tag{2.10}$$

where $\psi(\vec{r}) = \sum_{l=0}^{\infty}\psi_l(\vec{r})$. The quantity

$$S_{ll'} = \delta_{ll'}e^{2i\delta_l} \tag{2.11}$$

in (2.10) is known as the *scattering matrix* or S-matrix. By construction, for $\delta_l \in \mathbb{R}$, then the S-matrix is unitary, i.e.,$SS^\dagger = S^\dagger S = I$, where I is the *identity matrix*. The conservation of l during a collision with a radial potential, as we have so far considered, is reflected in the S-matrix; it is diagonal with respect to l. For elastic scattering, the scattering phases *must* be real so that S

is unitary and the particle flux is conserved, i.e. the incoming (e^{-ikr}) and outgoing (e^{+ikr}) waves must have the same normalization.

Inelastic scattering of neutral particles — multiple channels

The different internal states of an electron-molecule system are known as *channels*. In the event of elastic scattering, the system is restricted to one channel; the internal states of the electron and molecule are left unchanged and different values of l are left uncoupled. A system's total wavefunction can be described as a product of a wavefunctions describing the internal state of the colliders and a wavefunction describing the relative motion of the colliders. Neglecting symmetrization/antisymmetrization of identical fermions/bosons, it takes the following form:

$$\Psi(\vec{r},\omega) = \sum_i \psi_i(\vec{r})\phi_i(\omega). \tag{2.12}$$

In (2.12), ω represents the internal coordinates of freedom of both colliders, $\phi_i(\omega)$ are wavefunctions defining the channel $|i\rangle$, and $\psi_i(\vec{r})$ are the *channel wavefunctions*. The $\phi_i(\omega)$ solve the Schrödinger equation for the internal degrees of freedom ω,

$$\widehat{H}_\omega \phi_i(\omega) = E_i \phi_i(\omega). \tag{2.13}$$

The total Schrödinger equation for the system, in atomic units,

$$\begin{aligned}
\widehat{H}\Psi(\vec{r},\omega) &= E\Psi(\vec{r},\omega) \\
\left[-\frac{1}{2}\nabla^2 + \widehat{H}_\omega + V(\vec{r},\omega)\right]\Psi(\vec{r},\omega) &= E\Psi(\vec{r},\omega) \\
\sum_i \left[-\frac{1}{2}\nabla^2\psi_i(\vec{r})\phi_i(\omega) + E_i\psi_i(\vec{r})\phi_i(\omega) + \widehat{V}(\vec{r},\omega)\psi_i(\vec{r})\phi_i(\omega)\right] &= E\sum_i \psi_i(\vec{r})\phi_i(\omega),
\end{aligned} \tag{2.14}$$

where $\widehat{V}(\vec{r},\omega)$ is a coupling operator that acts on both functions of $\vec{r}$ and ω. Projecting (2.14) onto some internal state $\phi_j(\omega)$ and expanding the full Hamiltonian,

$$\sum_i \int d\omega\ \phi_j^*(\omega)\widehat{H}\psi_i(\vec{r})\phi_i(\omega) = E\sum_i \psi_i(\vec{r})\overbrace{\int d\omega \phi_j^*(\omega)\phi_i(\omega)}^{\delta_{j,i}}$$

$$-\frac{1}{2}\nabla^2\psi_j(\vec{r}) + \sum_i \underbrace{\int d\omega\ \phi_j(\omega)\widehat{V}(\vec{r},\omega)\phi_i(\omega)}_{V_{j,i}(\vec{r})}\psi_i(\vec{r}) = (E-E_j)\psi_j(\vec{r})$$

$$-\frac{1}{2}\nabla^2\psi_j(\vec{r}) + \sum_i V_{j,i}(\vec{r})\psi_i(\vec{r}) = (E-E_j)\psi_j(\vec{r}), \tag{2.15}$$

we obtain the *coupled-channel equation* for the j^{th} channel. The quantities E_j define *channel energies*. A channel is *open* if the total energy of the system, E, is larger than the channel energy E_j. If $E_j < E$, then the channel j is *closed*. The total wavefunction (2.12) takes the following asymptotic form

$$\Psi(\vec{r},\omega) \xrightarrow{r\to\infty} e^{ik_j z}\phi_j(\omega) + \sum_i f_{ji}(\theta,\phi)\frac{e^{ik_i z}}{r}\phi_i(\omega) \tag{2.16}$$

As before, the channel wavefunctions can be expanded in a basis of partial waves

$$\psi_i(\vec{r}) = \sum_{l=0}^{\infty}\sum_{m=-l}^{l}\frac{\phi_{ilm}(r)}{r}Y_l^m(\theta,\phi). \tag{2.17}$$

The expansion (2.17) allows us to separate the radial and angular components of the coupled-channel equation (2.15), in atomic units,

$$\left(-\frac{d}{dr^2} + \frac{l(l+1)}{r^2}\right)\phi_{i,l,m}(r) + \sum_{i'l'm'} V_{ilm,i'l'm'}(\vec{r})\phi_{i',l',m'}(r) = E\phi_{i,l,m}(r) \tag{2.18}$$

where i and i' index initial and final internal channels of the target, respectively. This notation, with primed (') variables denoting final quantities and unprimed variables denoting initial quantities, will be used hereafter. This multichannel partial-wave expansion (2.17) reduces to (2.5) in the case

of a single channel with azimuthal symmetry ($m = 0$). Now that we consider multiple channels, the free-particle solutions to the uncoupled radial equation (2.6) depend on the channel via the channel wavenumber, $k_i = \sqrt{2(E_i - E)}$

$$\phi_l^{reg}(k_i r) \overset{k_i r \to \infty}{\propto} S_l(k_i r) = \sin\left(k_i r - \frac{l\pi}{2}\right), \quad \phi_l^{irr}(k_i r) \overset{k_i r \to \infty}{\propto} C_l(k_i r) = \cos\left(k_i r - \frac{l\pi}{2}\right) \tag{2.19}$$

for the ith channel.

Consequently, the normalization of these radial wavefunctions depends on the channel. This leads to the solutions not being normalized at all in the multichannel case, but they can instead be normalized in energy, picking up a multiplicative factor:

$$\phi_{E,l}^{reg}(k_i r) \to \sqrt{\frac{2m}{\pi k_i}}\phi_{E,l}^{reg}(k_i r), \quad \phi_{E,l}^{irr}(k_i r) \to \sqrt{\frac{2m}{\pi k_i}}\phi_{E,l}^{irr}(k_i r). \tag{2.20}$$

Should the colliding particle be an electron, $m = 0$.

The regular and irregular solutions form a basis (C.6) of the vector space $\mathbb{C}^{n_o}$, where n_o is the number of open channels $|ilm\rangle$ considered. The elements of the basis vectors are given, asymptotically, by

$$\phi_{ilm}^{i'l'm'}(r) \xrightarrow{r\to\infty} \delta_{ii'}\delta_{ll'}\delta_{mm'}\phi_{E,l}^{reg}(k_{i'} r) + K_{ilm,i'l'm'}\phi_{E,l}^{irr}(k_{i'} r), \tag{2.21}$$

which can be transformed into a basis of incoming ($\phi^{(-)}$) and outgoing ($\phi^{(+)}$) spherical waves (C.9):

$$\begin{aligned} \chi^{(\pm)}(k_i r) &= \phi_{E,l}^{irr}(k_i r) \pm i\phi_{E,l}^{reg}(k_i r) \xrightarrow{r\to\infty} \sqrt{\frac{2m}{\pi k_i}} e^{\pm(k_i r - l\frac{\pi}{2})} \\ \chi_{ilm}^{i'l'm'}(r) &\xrightarrow{r\to\infty} \delta_{ii'}\delta_{ll'}\delta_{mm'}\chi_{E,l}^{(-)}(k_{i'} r) - S_{ilm,i'l'm'}\chi_{E,l}^{(+)}(k_{i'} r). \end{aligned} \tag{2.22}$$

The relation between the two bases help us define a relation between the K-matrix in (2.21) and

the S-matrix in (2.22):

$$\underline{S} = (\underline{I} - i\underline{K})^{-1}(\underline{I} + i\underline{K}), \tag{2.23}$$

$$\underline{S} = \underline{U}e^{2i\underline{\delta}}\underline{U}^{\dagger}. \tag{2.24}$$

Here and throughout, any underlined variable will represent a matrix; the matrix $\underline{I}$ will always refer to the *identity matrix*. In (2.24), the matrix $\underline{\delta}$ is a diagonal matrix of asymptotic scattering associated with each channel $|il\lambda\rangle$. Comparing (2.22) with (2.16), we can define the scattering amplitude

$$f_{ii'}(\theta,\phi) = \sum_{l=0}^{\infty}\sum_{l'=0}^{\infty}\sum_{m'=l'}^{l'} Y_{l'}^{m'}(\theta,\phi) i^{l-l'-1}\sqrt{\frac{\pi(2l+1)}{k_i k_{i'}}}\left(S_{il0,i'l'm'} - \delta_{ii'}\delta_{ll'}\delta_{0m'}\right), \tag{2.25}$$

which will be useful in connecting the S-matrix to the observable cross section. More details on this subsection are available in Appendix C.

Collisions of charged particles

Unlike in the previous subsections, a collision between two charged particles is subject to the Coulomb potential. Here, we consider an electron interacting with a positively charged target. The Coulomb potential,

$$V_{Coulomb}(r) = \frac{V_0}{r}, \quad V_0 = \text{constant}, \tag{2.26}$$

is a long-ranger potential, falling off slower than $1/r^2$. In this case, the coupled-channel equation (2.15) includes the added term (2.26),

$$\left[-\frac{1}{2}\nabla^2 + \frac{V_0}{r}\right]\psi_j(\vec{r}) + \sum_i V_{j,i}(\vec{r})\psi_i(\vec{r}) = (E - E_j)\psi_j(\vec{r}), \tag{2.27}$$

where the total wavefunction, $\Psi(\vec{r},\omega)$ is defined as in (2.12). The electron-molecule collisions discussed later in this dissertation only involve neutral or positively charged target molecules. Because the target is positively charged, V_0 is negative, i.e. an attractive Coulomb potential. Expanding $\psi(\vec{r})$ again in a basis of partial waves, the addition of the Coulomb potential modifies the radial coupled-channel equation (2.18),

$$\left[-\frac{d}{dr^2}+\frac{l(l+1)}{r^2}+\frac{V_0}{r}\right]\phi_{i,l,m}(r)+\sum_{i'l'm'}V_{ilm,i'l'm'}(\vec{r})\phi_{i',l',m'}(r)=k_i^2\phi_{i,l,m}(r). \tag{2.28}$$

The two independent solutions, for positive scattering energies $k^2/2$, are known as the f and g Coulomb functions. The energy-normalized f and g functions exhibit similar behavior as the regular and irregular solutions (2.19) to the radial coupled-channel equation in the neutral case (2.18):

$$\begin{aligned} f_l(k_ir) &\rightarrow \begin{cases} 0 & r\rightarrow 0 \\ \sqrt{\frac{2}{\pi k_i}}\sin\left(k_ir-\eta_0^i\ln(r)+\eta^i\right) & r\rightarrow\infty \end{cases} \\ g_l(k_ir) &\xrightarrow{r\rightarrow\infty} \sqrt{\frac{2}{\pi k_i}}\cos\left(k_ir-\eta_0^i\ln(r)+\eta^i\right) \quad r\rightarrow\infty, \end{aligned} \tag{2.29}$$

where the long-range phase shift η^i and *Sommerfeld parameter* η_0^i are given by

$$\begin{aligned} \eta^i &= -\eta_0^i\ln(2k_i)+\arg\left(\Gamma(l+1+i\eta_0^i)\right)-\frac{l\pi}{2}, \\ \eta_0^i &= \frac{V_0}{k_i}. \end{aligned} \tag{2.30}$$

For clarity, the energy-normalized f and g Coulomb functions are related to the regular (B.29) and irregular (B.30) Coulomb functions by

$$f_l(kr) \equiv \sqrt{\frac{2}{\pi k}} F_l\left(\eta_0^i, kr\right) \tag{2.31}$$

$$g_l(kr) \equiv \sqrt{\frac{2}{\pi k}} G_l\left(\eta_0^i, kr\right). \tag{2.32}$$

The procedure for scattering amplitudes in terms of the S-matrix is very similar to that of the previous subsection. The energy-normalized f and g functions are used to construct the basis of asymptotic sine/cosine solutions to (2.28),

$$\phi^{ilm}_{i'l'm'}(r) \xrightarrow{r\to\infty} \delta_{ii'}\delta_{ll'}\delta_{mm'} f_l(k_{i'}r) + K_{ilm,i'l'm'} g_l(k_{i'}r), \tag{2.33}$$

which can be transformed into the basis of incoming (f^-) and outgoing (f^+) spherical waves,

$$\chi^{ilm}_{i'l'm'}(r) \xrightarrow{r\to\infty} \delta_{ii'}\delta_{ll'}\delta_{mm'} f^-(k_{i'}r) - S_{ilm,i'l'm'} f^+(k_{i'}r), \tag{2.34}$$

$$f^{\pm}(k_i r) = g_l(k_i r) \pm i f_l(k_i r) \xrightarrow{r\to\infty} \sqrt{\frac{2}{\pi k_i}} e^{\pm i\left(k_i r - \eta_0^i \ln(r) + \eta^i\right)}. \tag{2.35}$$

The S-matrix, through similar manipulations to those in (C.10), is still related to the K-matrix by (2.23), i.e. $\underline{S} = (\underline{S} - i\underline{K})^{-1}(\underline{S} + i\underline{K})$.

The process of expressing the sine/cosine solutions in terms of the ingoing/outgoing spherical-wave basis is slightly modified by the addition of the Coulomb potential, but remains similar. The asymptotic behavior of the channel wavefunctions $\psi_{i'}(\vec{r})$,

$$\psi_{i'}(\vec{r}) \xrightarrow{r\to\infty} \delta_{ii'} e^{i\left(k_{i'}z + \eta_0^{i'}\ln(k_{i'}(r-z))\right)} + \left(\delta_{ii'} f_{ii}^C(\theta) + f_{ii'}(\theta,\phi)\right) r^{-1} e^{i\left(k_{i'}r - \eta_o^{i'}\ln(2k_{i'}r)\right)} \tag{2.36}$$

takes a similar form, but includes the *Coulomb scattering amplitude*,

$$f_i^C(\theta) = -\frac{\eta_0^i}{2\sin^2(\theta/2)} e^{-i\left(\eta_0^i \ln\left[\sin^2(\theta/2)\right] - 2\arg(\Gamma(1+i\eta_0^i))\right)}. \tag{2.37}$$

The process for obtaining the scattering amplitudes $f_{ii'}(\theta,\phi)$ in terms of the S-matrix is similar to that of the previous subsection. Doing so, we arrive at

$$\begin{aligned} f_{ii'}(\theta,\phi) = \sum_{ll'm'} Y_{l'}^{m'}(\theta,\phi) \frac{\sqrt{\pi(2l+1)}}{k_i k_{i'}} i^{l-l'-1} e^{i\arg\left(\Gamma\left(1+l+i\eta_0^i\right)\Gamma\left(1+l'+i\eta_0^{i'}\right)\right)} \\ \times \quad \left(S_{il0,i'l'm'} - \delta_{ii'}\delta'_{ll'}\delta_{0m'}\right), \end{aligned} \tag{2.38}$$

which, again, will allow us to determine scattering cross sections in terms of the S-matrix.

Cross sections

For electron-molecule scattering with a neutral molecule, i.e. the electron's wavefunction behaves asymptotically as (2.3), the differential scattering cross section from the channel i to the channel i' is given by

$$\frac{d\sigma_{i\to i'}}{d\Omega} = \frac{k_{i'}}{k_i} \left|f_{ii'}(\theta,\phi)\right|^2, \tag{2.39}$$

where Ω is the solid angle and $d\Omega = \sin(\theta) d\theta d\phi$ and $f_{ii'}(\theta,\phi)$ is given by (2.25). Similarly, for a collision between an electron and a charged molecule, i.e. the electron's wavefunction obeys the boundary condition (2.36),

$$\frac{d\sigma_{i\to i'}}{d\Omega} = \frac{k_{i'}}{k_i} \left|\delta_{ii'} f_i^C(\theta) + f_{ii'}(\theta,\phi)\right|^2, \tag{2.40}$$

where the scattering amplitudes $f_i^C(\theta)$ and $f_{ii'}(\theta,\phi)$ are given by (2.37, 2.38). The total cross section from channel i to channel i', then, is given by the integral over all solid angles:

$$\begin{aligned}\sigma_{i\to i'} &= \int_0^{\pi} \sin(\theta) d\theta \int_0^{2\pi} d\phi \, \frac{d\sigma_{i\to i'}}{d\Omega}, \\ \sigma_i &= \sum_{i'} \sigma_{i\to i'}.\end{aligned} \tag{2.41}$$

The sum over i' is taken over all open channels i' . The total scattering cross section from channel i is σ_i.

Analyzing the form of (2.37, 2.38, 2.25), the low-energy behavior of the cross sections will follow the behavior $(k_{i'}/k_i)/(k_{i'}k_i) = k_i^{-2} \propto (E - E_i)^{-1}$. Cross sections following such a $1/E$ relationship diverge at $E = E_i$ and are, of course, not defined for negative $E < E_i$. More details of scattering theory are available in several works, such as those of Seaton[61], Friedrich[60,62] and Landau & Lifshitz[59].

Quantum defect theory

The concept of a *channel*, described in the previous sections, is important in the formulation of *multichannel quantum defect theory* (MQDT). MQDT, also referred to as multichannel spectroscopy, has roots in the works of Wigner[63,64] and Seaton[65,66]. To discuss MQDT, we will first introduce the concept of the quantum defect.

One channel

Within the nonrelativistic formulation of quantum mechanics, the energy levels of the hydrogen atom are given by

$$E_n^{\mathrm{H}} = -\frac{m_e e^4}{8\varepsilon_0^2 h^2 n^2} = -\frac{1}{2n^2} \equiv -\frac{\mathcal{R}}{n^2}, \tag{2.42}$$

where e is the charge of an electron, ε_0 is the permittivity of free space, n is the principal quantum number, and $\mathcal{R}$ is the *Rydberg constant*. The value E_1^{H} defines the Rydberg unit of energy, $\sim$13.6 eV. The threshold here is at $E = 0$, above which no bound states exist. A similar formula holds for the bound states of the atoms belonging to the alkali metal group, i.e., The energy levels, however, are still comparable to (2.42):

$$E_n = E_{th} - \frac{\mathcal{R}}{(n - \mu_{nl})^2}, \tag{2.43}$$

where E_{th} is energy threshold for ionization and μ_{nl} is known as the *quantum defect*, which is dependent on n and l. As $n \to \infty$, the quantum defects converge to a finite value:

$$\mu_l \equiv \lim_{n\to\infty} \mu_{nl}. \tag{2.44}$$

One can define the *effective quantum number*:

$$n_l^* \equiv n - \mu_{nl}. \tag{2.45}$$

Considering again the radial time-independent Schrödinger equation (2.6) with an atomic potential $V(r) \xrightarrow{r\to\infty} -Z/r$, Z being the screened charge of the nucleus at large distances, the solutions are the Coulomb f and g functions (2.29). For negative scattering energies, i.e. bound states, the energy levels follow (2.43). The infinite series given by (2.43) is known as a *Rydberg series*. The density of states increases as $n \to \infty$, i.e. $E_n \to 0^-$.

It is important to mention Levinson's theorem, which connects energy-dependent scattering phase-shifts $\delta_l(k)$ to the number of bound states:

$$\lim_{k\to 0} \delta_l(k) - \lim_{k\to\infty} \delta_l(k) = (n_l + N)\pi, \tag{2.46}$$

where n_l is the number of bound states with orbital angular momentum l, and N can be either 0 or 1/2. The case $N = 1/2$ corresponds to a bound state with l orbital angular momentum at $k = -0$. Such bound states — asymptotically sinusoidal and therefore not square-integrable — have been referred to as *half bound* states. Square-integrable bound states with $l > 0$, then, are represented by $N = 0$. $\delta_l(0)$ the zero-energy phase-shift for some l. For such a short-range potential, or any asymptotically bounded potential, the high-energy phase shift us negligible, i.e.

$$\lim_{k\to\infty} \delta_l(k) = 0 \implies \lim_{k\to 0} \delta_l(k) = (n_l + N)\pi. \tag{2.47}$$

Levinson's theorem (2.46, 2.47) can be extended to a potential with Coulombic asymptotic behavior:

$$\lim_{k\to 0^+} \delta_l(k) (\mathrm{mod}\ \pi) = \mu_l. \tag{2.48}$$

Such a potential hosts an infinite number of bound states, but the quantum defect for some small energy below threshold, ε, is equal to the number of bound states with lower energy than ε. As described by Seaton[67], this can be viewed as a generalization of (2.46). The ambiguity of a branch choice in (2.48) may be removed by requiring $\delta_l(k)$ to be continuous functions of energy[68], which is related to the analytic continuation of the phase shifts negative energies[67]:

$$\delta_l(k) = \pi\mu_l(k). \tag{2.49}$$

The quantum defect function $\mu_l(k)$ is continuous, depends only weakly on k, and coincides with the discrete quantum defects μ_{nl} introduced in (2.43). The analytic continuation (2.49) connects the below-threshold quantum defects to the single-channel S-matrix (2.11).

Multiple channels

The effective quantum number has already been defined in terms of the quantum defect and the principal quantum number (2.45). The analytic continuation of the quantum defect to above-threshold energies suggests we might also define the effective quantum number above and below threshold. Above threshold, the principal quantum number n is not defined, leaving us to define the effective quantum number as

$$n_l^*(k) = \mu_l^0(k) = -\frac{\delta_l^0(k)}{\pi}. \tag{2.50}$$

Defining the threshold energy, below which bound states are possible, as E_{th}, the effective quantum number can be defined as a continuous function that is an extension of its previous definition (2.45):

$$\begin{aligned} E_{th} - E &= \frac{\mathcal{R}}{n_l^{*^2}} \\ n_l^* &= \sqrt{\frac{\mathcal{R}}{E_{th} - E}}. \end{aligned} \tag{2.51}$$

This new definition below threshold (2.51) coincides with (2.45) at energies $E_n^{Rydberg}$ given by (2.43). Considering, now, two thresholds of energy E_{th}^1 and E_{th}^2 that are uncoupled, such that $E_{th}^1 < E_{th}^2$, the energies of the infinite bound states converging to each threshold is given, respectively, by E_{bound}^1 and E_{bound}^2,

$$E_{bound}^1 = E_{th}^1 - \frac{\mathcal{R}}{n_{l1}^{*^2}} \qquad E_{bound}^2 = E_{th}^2 - \frac{\mathcal{R}}{n_{l2}^{*^2}} \tag{2.52}$$

where $n_{l1}^{*^2}$ and $n_{l2}^{*^2}$ are the effective quantum numbers associated with the two channels. Channel coupling, however, changes the Rydberg series converging to each threshold. There are three cases to consider for some arbitrary energy E:

$\underline{E < E_{th}^1 < E_{th}^2}$: both channels are closed. The effective quantum number in channel i is

given by

$$n_{li}^{*}(E) = \sqrt{\frac{\mathcal{R}}{E_{th}^{i} - E}}. \tag{2.53}$$

Although energy eigenstates correspond only to bound states in this regime, their positions are slightly modified by the influence of the second threshold. Considering the positions of uncoupled bound states converging to E_{th}^{2} with positions E_{B}^{2}, the width of this state if it were a resonance[69], $\Gamma_{B}^{2} \approx 4\mathcal{R}\mathfrak{Im}(\mu_{l}^{0})/[n - \mathfrak{Re}(\mu_{l}^{0})]^{3}$, determines which bound states converging to E_{th}^{1} near E_{B}^{2} will be shifted. States around a half-width $\Gamma_{B}^{2}/2$ above or below E_{B}^{2} will be shifted. Shifting bound levels corresponds to a rise in their effective quantum defect relative to E_{th}^{1}, n_{l1}^{*}, by one; channel coupling effectively perturbs the resonances.

$\underline{E_{th}^{1} < E < E_{th}^{2}}$: only the first channel is open. The second channel still supports an infinite number of Rydberg states converging to E_{2}. These manifest as Feshbach resonances, which have resonance positions that approximately follow

$$E_{R} = E_{th}^{2} - \frac{\mathcal{R}}{n_{li}^{*2}}. \tag{2.54}$$

As $E \to E_{th}^{2}$, the density of these resonances increase inversely with their widths, as illustrated by Figure 2.2.

$\underline{E_{th}^{1} < E_{th}^{2} < E}$: both channels are open. Above all thresholds, the continuum does not have any Feshbach resonances, although other resonances, e.g., shape resonances, may be present. Figure 2.2 also illustrates this, to an extent. Although higher channel threshold were present in the calculation, the resonances appear only at higher energies.

For multiple channels, the quantum defects associated with certain channels can be encapsulated in the $n \times n$ S-matrix using (2.24, 2.49) — n being the number of included channels. As the scattering energy approaches a channel threshold from below, the cross sections oscillate with increasing frequency until the channel threshold, as shown in Figure 2.2.

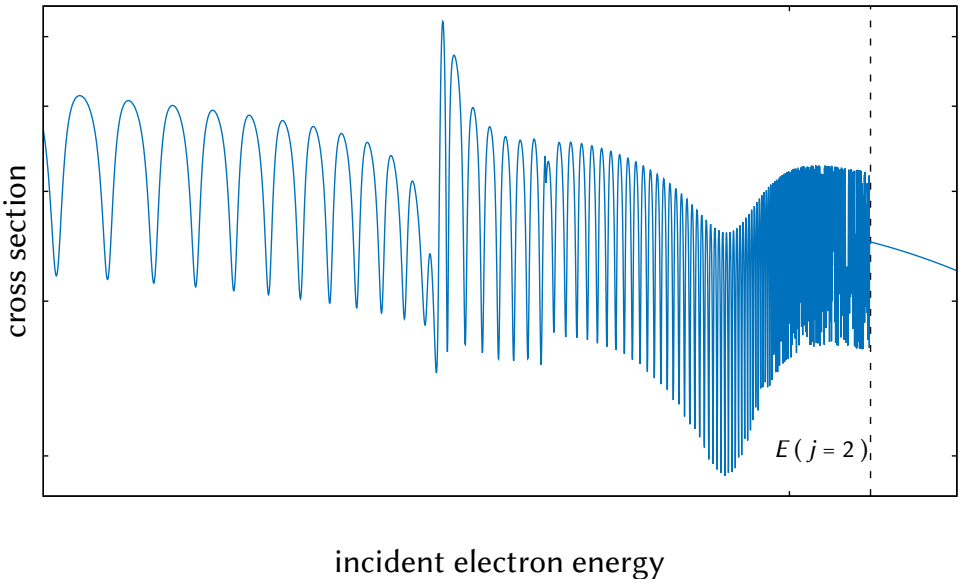

Figure 2.2: Rotational de-excitation cross section for an electron colliding with CH^+ in its first rotationally excited level of its ground vibronic state ($j = 1, v = 0, X^1\Sigma^+$). The channel threshold for excitation to the next rotational channel ($j = 2, v = 0, X^1\Sigma^+$) is shown as a vertical dashed line.

Resonances

Resonances are perhaps the most identifiable feature in observable signals, and are extremely important in describing certain physical phenomena, e.g., resonant dissociative recombination. Also known as *unstable* or *metastable* states. They have various shapes, contain a wealth of information about a collision. Resonances are characterized by a width Γ (energy units), not to be confused with the gamma function, a position in an energy domain, E_R, and a lifetime :

$$\tau = \frac{1}{\Gamma}. \tag{2.55}$$

Resonances may be defined in several ways, but these definitions become ambiguous as the resonance lifetime (2.55) decreases. Above-threshold phase-shifts are affected by resonances in the

following way:

$$\delta_l(E) = \delta_l^0(E) + \delta^{res}(E), \quad \tan(\delta^{res}(E)) = -\frac{\Gamma/2}{E - E_R}. \tag{2.56}$$

The phase shift $\delta_l^0(E)$ can be interpreted as a nearly constant background phase shift. The branch choice of the tangent is ambiguous, but can be chosen such that $\delta_l(E)$ remains a continuous function to avoid the restriction to a modulus of π. Applying (2.49), we can re-express (2.56) in terms of quantum defects,

$$\mu_l(E) = \frac{\delta_l(E)}{\pi} = \mu_l^0 + \mu_l^{res}, \quad \mu_l^0 = \frac{\delta_l^0(E)}{\pi}, \quad \mu_l^{res}(E) = -\frac{1}{\pi}\arctan\left(\frac{\Gamma/2}{E - E_R}\right). \tag{2.57}$$

The quantum defect μ_l^0 is, by definition, also very weakly energy dependent.

Two common resonances will be briefly introduced: *shape resonances* and *Feshbach resonances*. Shape resonances are also known as *potential resonances* due to their nature — these are almost-bound (not to be confused with half-bound) continuum states that decay only slowly due to the centrifugal barrier of the potential. They are often clearly identifiable, short-lived (wide) resonances. The centrifugal barrier, as the name implies, comes from the centrifugal term in (2.6): $l(l+1)/r^2$.

Feshbach resonances have a much sharper profile, i.e. are much longer-lived states, than than that of shape resonances. They exist only if the system has more than one degree of freedom. These resonances are bound in one degree of freedom, but can decay in another, where they lie in the continuum. This is an inherently multichannel phenomenon, arising due to couplings between channels. Eliminating this coupling would yield true bound states, which is perhaps one distinction between these resonances and shape resonances.

Channel elimination

The asymptotic basis of incoming and outgoing wavefunction (2.22) can be used to construct the outer-region matrix

$$i\sqrt{2}M_{il\lambda,i'l'\lambda'}(r) = f_l^-(k_i r)\delta_{ii'} - f_l^+(k_i r)S_{il\lambda,i'l'\lambda'}. \tag{2.58}$$

The term "outer-region" will be briefly discussed in the next section. For closed channels, the functions $f^\pm$ diverge as $r \to \infty$. If there are a total of N considered channels $|il\lambda\rangle$, then the number of closed channels N_c and open channels N_o always add to N, i.e. $N = N_o + N_c$. A suitable map can be chosen, transforming the matrix $\underline{M}$ with closed channels to the matrix $\underline{M^-}$ of open-channel incoming-wave solutions:

$$\underline{M}^-(r) = \begin{pmatrix} \underline{M}^-_{oo}(r) \\ \underline{M}^-_{co}(r) \end{pmatrix} = \underline{M}(r)\underline{B}, \qquad \underline{B} = \begin{pmatrix} \underline{I} \\ \underline{B}_{co} \end{pmatrix}. \tag{2.59}$$

The matrices $\underline{B}$ and $\underline{M^-}$ have dimensions $N \times N_o$.

Before applying this transformation, the matrices $\underline{M}$ and $\underline{S}$ should be partitioned into sub-blocks of open (o) and closed (c) channels,

$$\underline{M} = \begin{pmatrix} \underline{M}_{oo}(r) & \underline{M}_{oc}(r) \\ \underline{M}_{cc}(r) & \underline{M}_{cc}(r) \end{pmatrix}, \qquad \underline{S} = \begin{pmatrix} \underline{S}_{oo} & \underline{S}_{oc} \\ \underline{S}_{cc} & \underline{S}_{cc} \end{pmatrix}, \tag{2.60}$$

so that the exponential growth in the closed channels — for which $f^\pm$ are defined differently — is eliminated. For negative energies, we define the quantity $\kappa_i = \sqrt{-2m_e E_i}$ and observe the asymptotic form of $f^\pm$ (in atomic units) for closed channels,

$$f_c^\pm(\kappa r) \xrightarrow{r\to\infty} \frac{1}{2\pi\kappa_i} e^{\pm i\beta_i}\left[\frac{1}{Dr^{n_l^*}}e^{\kappa r} \mp iDr^{n_l^*}e^{-\kappa r}\right], \tag{2.61}$$

where D depends on the energy and l, and $\beta_i = \pi/\sqrt{2(E_i - E)}$. As $r \to \infty$, the leading $e^{\kappa r}$ term in (2.61) dominates is eliminated in (2.59) by an appropriate choice of $\underline{B}_c$,

$$\underline{B}_c = -\left(\underline{S}_{cc} - e^{-2i\underline{\beta}}\right)^{-1} \underline{S}_{co}, \tag{2.62}$$

where $\underline{\beta}$ is a diagonal matrix whose entries are given by the quantity β_i in channel i (for closed channels). The resulting open-channel submatrix of $\underline{M}^-(r)$ then becomes

$$-\frac{i}{\sqrt{2}}\left[f_o^-(k_i r) - f_o^+(k_i r)\left(\underline{S}_{oo} + \underline{S}_{oc}\underline{B}_c\right)\right], \tag{2.63}$$

which allows us to define the *physical* $N_o \times N_o$ S-matrix

$$\underline{S}^{phys} = \underline{S_{oo}} - \underline{S_{oc}}\left(\underline{S_{cc}} - e^{-2i\underline{\beta}}\right)^{-1} \underline{S_{co}}. \tag{2.64}$$

The RHS of (2.64) is also referred to as the MQDT *closed-channel elimination procedure* (CCEP), while the LHS is called the *physical* S-matrix because it is expressed in a basis of physically allowed (open) channels. The physical S-matrix will be used to calculate rovibronic (de-)excitation and DR cross sections. Resonances in the observable cross section for DR, which will be calculated in terms of the physical S-matrix (2.64), come from the near-singularity of the matrix $\underline{S}_{cc} - e^{-2i\underline{\beta}}$. This matrix is singular at energies of bound states, but is never singular when there are no completely uncoupled closed channels (more details in Appendix C).

Closed channels can be further divided into *weakly* and *strongly* closed channels. Weakly closed channels, typically close to the total energy of the system, are treated as open. Strongly closed channels have a much larger difference between their channel energy (E_i) and the total energy (E), and are eliminated via (2.64)

The f and g functions of some weakly closed channels exhibit problematic behavior due to

the factor[61]

$$A(\varepsilon, l) = \prod_{n=0}^{l} (1 + n^2 \varepsilon), \tag{2.65}$$

which appears as $\sqrt{A(2E_i, l)}$ and $1/\sqrt{A(2E_i, l)}$ in the closed-channel f and g functions, respectively[61]. An alternative normalization for these channels can be obtained by

$$\begin{aligned} \tilde{f}_i(\kappa_i r) &= f_i(\kappa_i r)/\sqrt{A(2E_i, l)}, \\ \tilde{g}_i(\kappa_i r) &= g_i(\kappa_i r)\sqrt{A(2E_i, l)}, \end{aligned} \tag{2.66}$$

where $\tilde{f}$ and $\tilde{g}$ are given explicitly as f^0 and $\overline{g}$ by Greene et al.[70]. Typically, this alternate normalization is used if $E - E_i > -1/(2(l_i + 2)^2)$ in au. For example, if $E - E_i = 0.034$ au (slightly above 1 eV), then one could consider the channels attached to the $l \geq 2$ partial waves as weakly open, normalized according to (2.66).

The CCEP (2.64), however, assume that the f and g functions for different channels all have the same normalization. Defining the diagonal matrix $\underline{q}$ whose elements are given by

$$q_{il} = \begin{cases} 1 & \text{normalization: (2.29)} \\ \sqrt{A(2E_i, l)} & \text{normalization: (2.66), closed during CCEP} \\ \sqrt{A(2E_i, l)/\left(1 - e^{-2\pi/\sqrt{2(E_i - E)}}\right)} & \text{normalization: (2.66), open during CCEP} \end{cases} \tag{2.67}$$

the CCEP becomes

$$\begin{aligned} \underline{S}^{CE} &= \underline{S}_{oo} - \underline{S}_{co}\left[\underline{S}_{cc} - \left(\underline{q}\cos(\underline{\beta}) + i\underline{q}^{-1}\sin(\underline{\beta})\right)^{-1}\left(\underline{q}\cos(\underline{\beta}) - i\underline{q}^{-1}\sin(\underline{\beta})\right)\right]^{-1}\underline{S}_{co}, \\ \underline{S}^{phys} &= \left[(\underline{q}^{-1} - \underline{q}) + (\underline{q}^{-1} + \underline{q})\underline{S}^{CE}\right]\left[(\underline{q}^{-1} + \underline{q}) + (\underline{q}^{-1} - \underline{q})\underline{S}^{CE}\right]^{-1}. \end{aligned} \tag{2.68}$$

If this normalization procedure is not performed for any channel, then $\underline{q} = \underline{I}$ and (2.68) reduces to (2.64). Channels defined as closed during the calculation of the f and g functions may be

open at some other energy during the channel elimination procedure, hence the distinction in 2.67. More details on quantum-defect theory are available in several reviews, such as the works of Seaton[65–67,71] and Aymar et al.[69].

R-matrix

R-matrix theory, developed to study resonant reactions[72–75], is used to study electron-atom and electron-molecule collisions. A key aspect of R-matrix theory is the division of space ($\mathbb{R}^3$) into an *inner region* and an *outer region*, separated by a bounding spherical shell of radius a. The inner region ($S_{in} \subset \mathbb{R}^3$, $r < a$) contains the N-electron wavefunction, i.e. the wavefunction of the target atom/molecule containing N electrons; the scattering electron can also exist in this region. S_{in} can be centered anywhere, but is usually centered on the target's center of mass (CoM) or even center of charge (CoC).

In the outer region, ($S_{out} = \mathbb{R}^3 \setminus \overline{S_{in}}$), there is only the wavefunction of the scattering electron. In practice, of course, S_{out} does not extend to infinity. The scattering electron is considered distinguishable. In the inner region, all $N + 1$ electrons of the scattering problem may be present. The more complicated physics of S_{in} is governed by an interaction potential that includes nonlocal effects, but must only be solved once for each considered value of the total energy. The simpler physics of S_{out}, however, is solved for each total energy. Channels in S_{out} are coupled by the different terms in the multipole expansion of the interaction potential, which is easily solved by outwards integration from $r = a$, the sphere on which the outer- and inner-region solutions are matched.

Today, quantum chemistry codes allow us to calculate the many-electron inner region, but early R-matrix work did not aim to obtain inner region solutions. The R-matrix, unsurprisingly key to the approach, was defined by its value on the bounding sphere and the energy dependence of the reaction was determined by the outer-region physics. The R-matrix is still defined by its

value on the matching surface. Considering again the multichannel time-independent Schrödinger equation (2.14) and partial-wave expansion (2.17), the radial component of the total wavefunction can be re-expressed as

$$\phi_i(r) = \sum_k a R_{ik}(a, E) \frac{d\phi_k}{dr}\Big|_{r=a}, \tag{2.69}$$

where i and k identify channels, which include the quantum numbers l and m for each channel. Considering all channels in the basis, (2.69) can be re-written as a matrix equation

$$\vec{\phi}(r) = a\underline{R}(a, E) \frac{d\vec{\phi}}{dr}\Big|_{r=a}, \tag{2.70}$$

where $\vec{\phi}(r)$ is a vector and $\underline{R}(a, E)$ is now a matrix. The matrix $\underline{R}(a, E)$ is known as the R-matrix and can be propagated as $\underline{R}(r, E)$ to larger values of r. R-matrix calculations are done assuming that the target nuclei do not move.

The R-matrix can also be defined, for $r = a$ and some total energy E, by

$$R_{ik} = \sum_\gamma \frac{\omega_{i\gamma}\omega_{k\gamma}}{E_\gamma - E}, \tag{2.71}$$

where E_γ are poles of the R-matrix and $\omega_{i\gamma}$ is the overlap integral between the i^{th} inner-region wavefunction and the γ^{th} outer-region wavefunction, taken over all angles and internal coordinates at $r = a$. The R-matrix poles are obtained by diagonalizing the inner-region Hamiltonian. At all other energies $E \neq E_\gamma$, the R-matrix is holomorphic.

R-matrix calculations can be performed to obtain the short-range reactance matrix, $\underline{K}$, for several energies. The K-matrix (2.33), at $r = a$ is related to the R-matrix by

$$\underline{K} = \left(\underline{f}(a) - \underline{R}\frac{d\underline{f}}{dr}\Big|_{r=a}\right)\left(\underline{g}(a) - \underline{R}\frac{d\underline{g}}{dr}\Big|_{r=a}\right)^{-1}, \tag{2.72}$$

where $\underline{f}$ and $\underline{g}$ are diagonal matrices, whose nonzero elements are given by the f and g energy-

normalized coulomb functions (2.29). Like $\underline{R}$, $\underline{K}$ is real and symmetric. Therefore, it is diagonalizable:

$$\underline{K} = U \tan(\pi \underline{\mu}) U^{\dagger}, \tag{2.73}$$

where $\underline{\mu}$ is a diagonal matrix of quantum defects and U is, of course, a unitary matrix. The K-matrix can then be converted to the S-matrix by (C.11), which is used to calculate reaction cross sections. As a reminder, the R- K-matrices are both expressed in the same finite basis of channels that are included by the user.

The R-matrix can also have its closed channels eliminated similarly to (2.64),

$$\underline{R}^{phys} = \underline{R}_{oo} - \underline{R}_{oc} \left[\underline{R}_{cc} - W(E) \left(\frac{dW}{dR}(E) \right)^{-1} \right]^{-1} \underline{R}_{co}, \tag{2.74}$$

which is performed at the R-matrix radius $R = a$. The subscripts o and c have the same meaning as in, e.g., (2.64) — open and closed channels. W is the energy-normalized Whittaker Coulomb function[76] given in terms of (2.34) for closed channels, i.e. negative energies:

$$W_l(k_i r, n_i^*) = \frac{i}{\sqrt{2}} (e^{-i\beta_i f^+} - e^{i\beta_i f^-}). \tag{2.75}$$

Frame transformations

The interaction between an electron and a molecule can occur at several energy ranges, which all exhibit qualitatively different behavior. Fig 2.3 depicts such different regions one might consider when constructing a model to describe electron-molecule scattering. To begin any calculation, a *frame of reference* must be determined. The selection is arbitrary, but common choices simplify the physics for various systems. Two common reference frames are the *lab(oratory) frame* (AKA the space-fixed frame) and the *molecular frame* (AKA the body frame).

In the lab frame the laboratory in which an experiment is conducted is at rest. Experimental

measurement are typically made in this frame. In the molecular frame, the molecule is at rest. The molecular frame is often centered on the target molecule's CoM or CoC and aligned, conventionally, such that the $\widehat{z}$-axis coincides with the highest symmetry axis of the molecule. The CoM, if chosen as the origin of a reference frame, is defined as the point where, for a point-mass system, the position vectors ($\vec{r}_i$) multiplied by their respective point mass (m_i) add to $\vec{0}$:

$$\sum_i m_i \vec{r}_i = \vec{0}. \tag{2.76}$$

In the CoM, the translational motion of the molecule can be separated from the other degrees of freedom. As a possible analogue to the CoM, the CoC, when chosen as the origin of a reference frame, is the point where the electric dipole moment $\left(\vec{p}(\vec{r})\right)$ is $\vec{0}$. For a point-charge system,

$$\vec{p}(\vec{r}) = \sum_i q_i(\vec{r}_i - \vec{r}), \tag{2.77}$$

where q_i is the charge of the point charge i and $\vec{r}_i$ is its position vector. For neutral systems, $\sum_i q_i \vec{r} = 0$ in (2.77), i.e. the dipole moment of neutral systems is invariant in space. Therefore, as an important distinction between the CoM and CoC, the CoC cannot be defined for neutral systems. Depending on the type of model being used and calculations being performed, one might be preferable over the other if they are different.

While experimental measurements are typically performed in the lab frame, theoretical and computational approaches have been developed in both. The lab frame and the molecular frame are appropriate for different regimes, as depicted by Figure 2.3. The molecular frame is good at smaller distances r between the scattering electron and the molecule, where the projection of the system's total angular moment is a conserved quantum number. At small distances, the interaction between and electron and a molecule can be well described within the frozen-nuclei or Born-Oppenheimer approximation. The mass of a nucleon is almost 2000 times that of an electron.

Therefore, electronic motion happens on significantly smaller time scales than nuclear motion, i.e. molecular vibration and rotation. As the distance between the electron and the molecule increases, the internuclear distance R can no longer be treated as a constant with the same accuracy as when the electron interacts with the molecule at short distances. The electron is far away enough for the molecule to vibrate on the time scale of the collision. The molecular frame is still appropriate for describing an electron impinging on a vibrating target. For an electron at large distances impinging on a rotating molecule, the rotating molecular frame is no longer the appropriate choice. The lab frame is then an appropriate choice to describe, asymptotically, an electron colliding with a rotating and vibrating molecule.

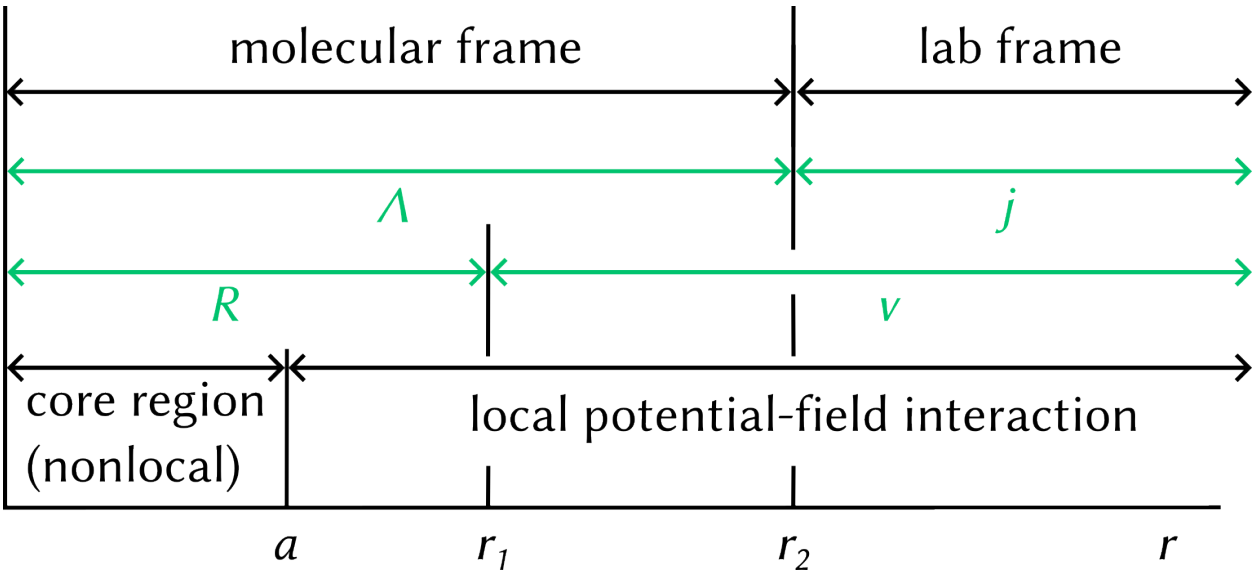

Figure 2.3: Figure 1 from Chang and Fano[77] redrawn here. Different regions of an electron-molecule collisions system, showing relevant quantities in each region. The numbers Λ, j, v, and R represent, respectively, the projection of the system's total angular momentum on the molecular axis, the angular momentum of the target, the vibrational quantum number of the target, and the internuclear distance. The bottom axis represents r, the distance between the scattering electron and the system's coordinate origin. a is the R-matrix radius.

The lab and molecular frames can be related through a *frame transformation*[77,78]. One reason for the practicality of frame transformations is that quantum chemistry calculations, now ubiq-

uitous in theoretical developments to study electron-molecule collisions, are typically performed in the molecular frame, but experimental measurements are made in the lab frame. Additionally, increasing experimental technicality and precision allow for state-selected reaction cross sections with electronic, vibrational, and rotational, i.e. *rovibronic*, resolution. Frame transformations allow us to pass from short-range interactions that are diagonal in R to a long-distance regime where the rotation and vibration of the molecule are coupled. This is related to l-uncoupling[79], where the orbital angular momentum of the scattering electron (l), coupled to that of the molecule at small distances where the electron essentially rotates with the molecule, is uncoupled from that of the molecule.

Frame transformations can be applied to various quantities, but they are only applied to the S-matrix in the work presented in this manuscript. Hence, the frame transformations will be shown applied to the S-matrix. The rovibrational frame transformation produces, from an S-matrix that is a function of R in a basis of electronic channels, an S-matrix that is expressed in a basis of rovibronic channels. This is done in two steps: the vibrational frame transformation and the rotational frame transformation. Additionally, frame transformations are only applied in the case of non-symmetric diatomic molecules. Hence, the theory will be presented under this assumption.

Vibrational frame transformation

To pass between regimes in which the *mutually incompatible* variables R and v are sensible, the vibrational frame transformation is used. R and v (and j and Λ) being mutually incompatible means that their respective operators do not commute. The vibrational frame transformation takes as input the electronic S-matrix in a basis of electronic channels $|nl\lambda\rangle$, i.e.

$$S^{\Lambda}_{n'l'\lambda',nl\lambda}(R) \equiv \langle n'l'\lambda'|\widehat{S}(R)|nl\lambda\rangle \tag{2.78}$$

where n identifies the electronic state of the target, l is the magnitude of the orbital angular momentum quantum number of the scattering electron, and λ is the projection of $\vec{l}$ on the molecular axis. The superscript Λ indicates that the S-matrix is block diagonal with respect to Λ. Before proceeding with the frame transformation, the vibrational wavefunctions of the target need to be calculated. This is be done by solving the vibrational Schrödinger equation for a diatomic molecule,

$$\left(-\frac{1}{2}\frac{M_1+M_2}{M_1M_2}\frac{d^2}{dR^2}+V(R)\right)\phi_{nv}(R)=E_{nv}\phi_{nv}(R), \tag{2.79}$$

where the masses of the nuclei are M_1 and M_2 and $\phi_{nv}(R)$ are wavefunctions describing the molecule in the state $|nv\rangle$ and the scattering electron in the state $|l\lambda\rangle$. v is, of course, the vibrational quantum number of the molecule. The potential $V(R)$ is the internuclear potential. More details will be provided about the calculation of these vibrational wave function later on.

With the vibrational wavefunctions obtained for each electronic state of the target, the vibrational frame transformation can be carried out. It is given by

$$S^{\Lambda}_{n'v'l'\lambda',nvl\lambda}\equiv\int dR\phi_{n'v'}(R)S^{\Lambda}_{n'l'\lambda',nl\lambda}(R)\phi_{nv}(R). \tag{2.80}$$

The S-matrix is still block diagonal with respect to Λ in this regime, but is no longer a function of R. Instead, it expressed in a basis of body-frame *vibronic* channels $|nvl\lambda\rangle$.

Rotational frame transformation

We now consider the mutually incompatible quantum numbers j and Λ, ignoring electron spin. The rotational frame transformation is performed on the vibronic S-matrix as follows[80,81]:

$$S^{J}_{n'v'j'\mu'l',nvj\mu l}=\sum_{\Lambda}\sum_{\lambda\lambda'}(-1)^{l+\lambda+l'+\lambda'}C^{j'\mu'}_{l'-\lambda',J\Lambda}S^{\Lambda}_{n'v'l'\lambda',nvl\lambda}C^{j\mu}_{l-\lambda,J\Lambda}. \tag{2.81}$$

In (2.81), the $C^{j\mu}_{l-\lambda,J\Lambda}$ are the Clebsch-Gordan coefficients. The total angular momentum of the system is $\vec{J} = \vec{j} + \vec{l}$, where $\vec{j}$ is the total angular momentum of the target. μ is the projection of $\vec{j}$ on the molecular axis. For diatomics, μ is given entirely by the orbital angular momentum of the target's electronic state because the rotational angular momentum of the target is perpendicular to the molecular axis. During the collision, J and M, the projection of J on the lab frame, are conserved. $\Lambda = \lambda + \mu$, however, is not necessarily conserved during a collision. Hence, the S-matrix is now block diagonal with respect to J and not Λ. It should be stressed that this transformation is unitary, i.e. $S^J S^{J\dagger} = I$.

CHAPTER 3: REA VIA DIPOLE-BOUND STATES, C_3N

Radiative electron attachment,

$$M + e^- \rightarrow M^- + \hbar\omega. \tag{3.1}$$

is the process by which an electron encounters a neutral molecule and forms a resonant state that relaxes via photon emission. The system could relax to any state of M^- allowed by angular momentum selection rules, including DBSs. The DBSs converge to the potential surface of the neutral molecule, much like how Rydberg states converge to the potential surface of the cation. Given that the target is a neutral molecule, the long-range interactions are dominated by non-Coulomb interactions. Although the dipole term in the expansion of the interaction potential is typically the strongest, other authors ave investigated quadrupole-bound and polarization-bound states[82,83]. The effect of vibration and rotation[28–30] have also been studied, showing that the critical dipole moment is larger for rotating dipoles than stationary dipoles. However, no fully quantum study of REA through a DBS including rotation and short-range interactions has been carried out.

Theoretical model

The neutral molecule of interest here is C_3N. Most theoretical approaches for studying REA are fairly straightforward: calculate bound-state anionic wavefunctions (ψ_f), continuum wavefunctions (ψ_i), and the dipole transition operator between the two ($\widehat{d}_{i\rightarrow f}$). The approach described here is essentially the same. To obtain these quantities, the potential energy operator of the e^- – C_3N system is calculated in molecular frame with the origin at the CoM of the molecule and the $\widehat{z}$-axis aligned with the molecular axis pointing towards the N atom. For a system of point charges q_i with

position vectors $\vec{r}_i$, it is possible to define a CoC as

$$\vec{R}_C = \frac{\sum_i q_i \vec{r}_i}{\sum_i q_i}. \tag{3.2}$$

The dipole moment with respect to the CoC is zero. For neutral systems, on the other hand, the CoC is not defined because the dipole moment is invariant with respect to the choice of origin:

$$\sum_i q_i \left(\vec{r}_i - \vec{R}\right) = \sum_i q_i \vec{r}_i - \vec{R}\cancelto{0}{\sum_i q_i} = \sum_i q_i \vec{r}_i. \tag{3.3}$$

For the C_3N molecule, therefore, the CoM is the most natural choice. The scattering electron's polar coordinates are given by (r, θ).

Two different potentials are calculated to highlight the effects of the short-range interactions. The first potential, V_{dip}, is entirely given by the interaction between a point charge and a dipole,

$$V_{dip} = -\frac{\mu e}{r^2} P_1\left(cos(\theta)\right), \tag{3.4}$$

where μ is the dipole moment of C_3N ($\mu = 1.3$ au) and $P_1\left(cos(\theta)\right)$ is a Legendre polynomial. The second potential, V_{ai}, is an *ab initio* potential comprised of four contributions and is a function of the electronic wavefunction of C_3N, ψ^e:

$$V_{ai}(\psi^e) = V_{elec}(\psi^e) + V_{nuc} + V_{ex}^{HFEGE}(\psi^e) + V_{copol}(\psi^e). \tag{3.5}$$

The potentials V_{elec} and V_{nuc} are the electronic and nuclear contributions of the electrostatic potential between C_3N and the scattering electron. The terms $V_{ex}^{HFEGE}(\psi^e)$ and V_{copol} are density-functional expressions representing the electron exchange and correlation-polarization contributions, respectively[84,85]. The perpendicular ($\alpha_\perp$) and parallel ($\alpha_\parallel$) polarizabilities, and the ionization potential (IP) of C_3N are needed for the potential of (3.5). Their values are $\alpha_\perp = 27.11$,

$\alpha_{\|} = 60.35$, and IP = 0.53 au. The wavefunction ψ^e represents the ground electronic state of C_3N ($X^2\Sigma^+$) in its equilibrium geometry with the following three internuclear distances in the C-C-C-N arrangement from left to right: 2.30, 2.62, and 2.13 au (see supplementary material of Lara-Moreno et al.[25]). This same geometry is used within the Born-Oppenheimer approximation for all calculations described herein. The calculated dipole moment of C_3N, 1.3 au, is in very good agreement with the complete active space-configuration (CAS-CI) value of 1.4 au by Harrison and Tennyson[23]. This suggests that the long-range e^- – C_3N potential, dominated by the dipole term, is well described.

Each contribution to the potential V_{ai} is expanded into a series of Legendre polynomials to obtain an expansion of the total potential in Legendre polynomials:

$$V_{ai} = \sum_{\lambda=0}^{80} C_\lambda(r) P_\lambda \left(cos(\theta)\right). \tag{3.6}$$

This is accomplished by first shifting the *ab initio* multi-centered Gaussian basis set and analytically expanding it around the neutral molecule's CoM in a symmetrized basis of real spherical harmonics[86] for values of l from 0 to 80. The Legendre polynomial expansion coefficients of the potentials $V_{elec}(\psi^e)$ and V_{nuc} are obtained with the standard procedure for $\left|\vec{r} - \vec{r}'\right|^{-1}$ potentials, described, for example, by Gianturco and Stoecklin[87]. The *ab initio* calculations were performed using the `MOLPRO` software suite[88,89] at the multi-configurational self-consistent field (MCSCF) level using the correlation-consistent polarized valence sextuple-zeta with diffuse augmenting functions (`aug-cc-pV6Z`) atomic orbital basis set. Calculations were performed in the C_{2v} point group (A.2). The number of occupied orbitals in the irreps A_1, B_1, B_2, and A_2 was 13, 3, 3, and 0. Of these occupied orbitals, the lowest 6 A_1 orbitals were considered closed.

The electronic and nuclear contributions to the local electrostatic interaction potential are

given, respectively, by

$$V_{elec}(\vec{r}\,') = 2\sum_i \int d\vec{r}\, \frac{\left|\phi_i(\vec{r})\right|^2}{\left|\vec{r} - \vec{r}\,'\right|} \tag{3.7}$$

and

$$V_{nuc}(\vec{r}\,') = -2\sum_i \int d\vec{r} \sum_j \frac{Z_j}{\left|\vec{r} - \vec{R}_j\right|} \tag{3.8}$$

in atomic units. $\phi_i(\vec{r})$ is the i^{th} target orbital, $\vec{r}$ is the position vector of an electron belonging to the target, $\vec{r}\,'$ is the position vector of the incident (scattering) electron, Z_j is the charge of the j^{th} nucleus, and $\vec{R}_j$ is the position vector of the j^{th} nucleus.

The exchange contribution to (3.5), $V_{ex}^{HFEGE}(\psi^e)$, is given, in atomic units, by

$$\begin{gathered} V_{ex}^{HFEGE}(\vec{r}) = -\frac{2}{\pi} k_F(\vec{r}) F(\eta) \\ F(\eta) = \frac{1}{2} + \frac{1-\eta^2}{4\eta} \ln\left(\frac{1+\eta}{1-\eta}\right) \\ \eta \equiv \eta(\vec{r}) = \frac{k_F(\vec{r})}{\sqrt{k_F^2(\vec{r}) + (E_{el} + \text{IP})}}, \quad k_F(\vec{r}) = \left(3\pi^2 \rho(\vec{r})\right)^{1/3}, \end{gathered} \tag{3.9}$$

where $\rho(\vec{r})$ is the charge distribution of the initial (ground) state of the target, E_{el} is the energy of the incident electron, and IP is the ionization potential of the target. The correlation-polarization contribution to (3.5), V_{copol}, is a piecewise potential made of the correlation potential V_{co} and the long-range polarization potential V_{pol}. The latter is given, in atomic units, by

$$V_{pol}(\vec{r}) = -\frac{1}{2r^4}\left(\alpha_{\parallel} + \alpha_{\perp} P_2(cos(\theta))\right), \tag{3.10}$$

while the former is given by

$$V_{co}(\vec{r}) = \begin{cases} 0.0311\ln(r_s) - 0.0584 + 0.00133 r_s \ln(r_s) - 0.0084 r_s & r < 1 \\ -0.1423(1 + \frac{7}{6}\beta_1 r_s^{1/2} + \frac{4}{3}\beta_2 r_s)/(1 + \beta_1 r_2^{1/2} + \beta_2 r_2)^2 & r_s \geq 1, \end{cases} \tag{3.11}$$

where $\beta_1 = 1.0529$, $\beta_2 = 0.3334$, and $r_s = (3/(4\pi\rho(\vec{r})))^{1/3}$. $\rho(\vec{r})$ is still the charge distribution of the target's ground state. The correlation-polarization potential is given by (3.11) at shorter distances and (3.10) at distances larger than the distance at which both intersect.

Figure 3.1 compares the two potentials, which are significantly different at small distances. The point dipole on its own, therefore, may not accurately describe the C_3N DBS. The *ab initio* potential, however, includes short- and long-range contributions. The nuclear potential V_{nuc} is strongly attractive near the nuclei, where it dominates the interaction. For slightly larger values of r, the repulsive $V_{elec}(\psi^e)$ potential and attractive $V_{ex}^{HFEGE}(\psi^e)$ and $V_{copol}(\psi^e)$ terms add to make an overall less attractive potential than the pure charge-dipole potential V_{dip}. The high energy continuum states states and resonances are not expected to be accurately represented by the *ab initio* potential, but it should describe the process qualitatively well at low collision energies where the long- and mid-range contributions control the dynamics.

Dipole-bound states

First, the final (DBS) wavefunctions are calculated by solving the Schrödinger equation

$$\left[-\frac{1}{2m}\left(\frac{1}{r}\frac{d^2}{dr^2}\right)\frac{\vec{L}\cdot\vec{L}}{2mr^2} + B\vec{J}\cdot\vec{J} + V(r,\widehat{Z})\right]\psi^i(\vec{r},\widehat{Z}) = (E - E_\alpha)\psi^i(\vec{r},\widehat{Z}), \tag{3.12}$$

where $\vec{r}$ and $\widehat{Z}$ are, respectively, the position vector of the scattering electron and the unit vector representing the orientation of the molecular axis in the lab frame, and B is the rotational constant of C_3N (linear). m is the reduced mass of the e^- – C_3N system, $\vec{L}$ is the orbital angular momentum

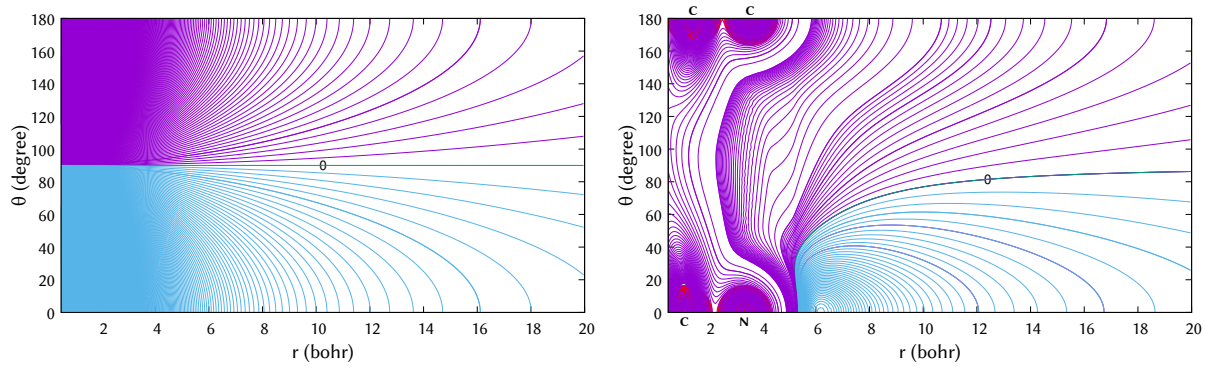

Figure 3.1: The two potentials used in the study, V_{dip} (left panel) and V_{ai} (right panel), shown as a function of the Jacobi coordinates r and θ. The energy-dependent potential V_{ai} is represented at an electron scattering energy -0.1 eV ($\sim$-806.5 cm^{-1}). The origin of the figure is the C_3N CoM. The positions of the four atoms are also shown on the right panel.

operator, $\vec{J}$ is the total angular momentum operator, and E_α is the energy of the molecule. A simple basis set to describe the free molecule, $\phi_\alpha = |Jm_J\rangle$, is comprised of the eigenfunctions of (J^2, m_J), m_J being the projection of J onto the lab-frame $\widehat{z}$-axis. The resulting radial coupled-channel equation to solve is then

$$\left[\frac{d^2}{dr^2} - \frac{l(l+1)}{r^2} + 2m(E - E_\alpha)\right] \psi_{\alpha,m_l(\alpha),l}(r) = 2m \sum_{\alpha' m_l' l'} \left(B\vec{J}\cdot\vec{J} + V(r,\widehat{Z})\right)^{\alpha l m_l}_{\alpha' l' m_l'} \psi_{\alpha',m_l',l'}(r) \tag{3.13}$$

We propagate solutions with the Magnus propagator as described in the work of Heather and Light[90,91], and Guillon and Stoecklin[92]. The solutions are propagated from the classically forbidden small-r, where the solution and its coordinate derivatives are assumed to be zero. The propagation continues to some boundary value in the potential well r_b, at which the R-matrix is calculated according to (2.69). A solution second propagation is done from large distances where the solution obeys asymptotic boundary conditions given by the Wentzel-Kramers-Brillouin (WKB) approximation to $r = r_b$, where a second R-matrix is calculated. A third matrix R_{diff}, equal to the difference of the two R-matrices from each propagation, is constructed and diagonalized. This

Table 3.1: DBS energies (cm^{-1}) obtained for the two potentials for different values of J.

J	$E(V_{ai})$	$E(V_{dip})$
0	-6.87	-22.13
1	-6.57	-21.80
2	-5.87	-21.14
3	-4.90	-20.15
4	-3.51	-18.84
5	-1.87	-17.19
6		-15.21
7		-12.91
8		-10.27
9		-7.30
10		-4.01
11		-0.38

procedure is repeated for several energies, varied from near the bottom of the potential well to the continuum, to search for bound states at which at least one eigenvalue of R_{diff} is zero.

40 rotational states of C_3N were used, the wavefunctions were propagated from $r = 0.1$ to $r = 300$ bohr, and the boundary between propagation and counter-propagation was fixed at $r_b = 3.2$ bohr. The energies of the DBSs obtained using each of the two potentials are given in Table 3.1 for different values of the total angular momentum J. The potential V_{dip} supports bound states for $J = 0$ to $J = 11$, while V_{ai} only supports bound states up to $J = 5$ due to the less attractive mid-range part of V_{ai} . For either potential, even-parity $J > 0$ states exist only for odd values of J and odd-parity states exist only for even values of J. Successive rotational levels in both cases follow the usual law for a rigid linear molecule with a rotational constant B:

$$E_{rot} = E_{ground} + BJ(J + 1), \tag{3.14}$$

where E_{ground} is given by the $J = 0$ value of each potential in Table 3.1. The rotational constant of Gottlieb et al.[93] agrees well with the energy splittings in Table 3.1. Taking a Boltzmann average

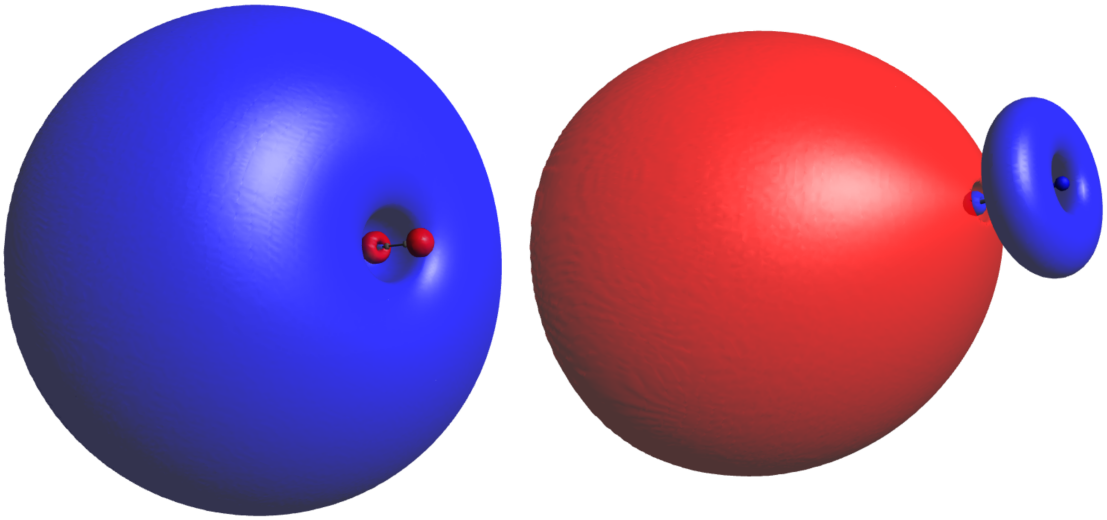

Figure 3.2: Dipole-bound states of C_3N^- for $J = 0$ with energy -6.87 cm^{-1}(left) and $J = 1$ with energy -6.57 cm^{-1}(right)

over the DBS energies obtained with the V_{ai} potential,

$$E_{avg} = \frac{\sum_{J=0}^{5} E_J(2J+1)e^{-E_J/kT}}{\sum_{J=0}^{5}(2J+1)e^{-E_J/kT}}, \tag{3.15}$$

where E_J is the energy in Table 3.1 relative to the $J = 0$ value, we find an average value of 2.66 cm^{-1} at the experimental temperature of 16 K, which is in good agreement with the experimental estimate (-2$\pm$1 cm^{-1}) of Simpson et al.[26] and the theoretical value (-2 cm^{-1}) obtained by the multireference configuration interaction (MRCI) calculation of Jerosimić et al.[94], who neglected rotation.

Figure 3.2 shows contour plots of the two lowest-energy DBS wavefunctions obtained for the V_{ai} potential. Wavefunctions with larger J look qualitatively similar, but with additional nodes along the $\widehat{z}$-axis. Wavefunctions associated with the V_{dip} potential qualitatively similar long-distance forms, but lack the short-range features of the V_{ai} wavefunctions.

Continuum states and REA cross sections

Initial (continuum-state) wavefunctions for the e^- – C_3N system are also needed. One major difference between this approach and that of Lara-Moreno et al.[24] is that we take into account the effect of rotation on the REA process. As discussed in the previous chapter, the lab frame is more appropriate for such a description than the molecular frame used in that study. Furthermore, we take advantage of our local model of the interaction potential and use a method that was initially developed for radiative association[95,96] and later adapted to REA[97,98].

Vibration, however, is not resolved. The scattering wavefunctions, in the rigid rotor approximation, take the following form in Jacobi coordinates:

$$\psi^i(\vec{r},\widehat{Z}) = \frac{1}{r}\sum_{jl}\chi^{JM}_{jl}(r)Y^{JM}_{jl}(\widehat{r},\widehat{Z}). \tag{3.16}$$

$\vec{l}$ is the orbital angular momentum of the electron, $\vec{j}$ is the total angular momentum of the neutral target, and $\vec{J} = \vec{j} + \vec{l}$ is the total angular momentum of the system. M, m_l, and m_j are, respectively, the projections of $\vec{J}$, $\vec{l}$, and $\vec{j}$ on the lab-frame $\widehat{z}$-axis. The superscript i denotes that this is an initial state of the system. The angular functions $Y^{JM}_{jl}(\widehat{r},\widehat{Z})$ are given by

$$Y^{JM}_{jl}(\widehat{r},\widehat{Z}) = \sum_{m_j m_l}\langle jm_j lm_l|JM\rangle\, Y_{lm_l}(\widehat{r})Y_{jm_j}(\widehat{Z}),. \tag{3.17}$$

where $Y_{l\lambda}$ are the real-valued spherical harmonics (B.24). It should be noted that, as per conventional notation, any two vectors $\widehat{a}$ and $\vec{a}$ have the same orientation, but $\widehat{a}$ has unit length.

The radial part of the scattering wavefunction, $\chi^J_{jl}(r)$, solves the driven differential equation[96]

$$\left[\frac{d^2}{dr^2} - \frac{l(l+1)}{r^2} + k^2_j(E) - 2m_r V^J_{j'l',jl}(r)\right]\chi^J_{jl}(r) = \lambda^{\alpha J}_{jl}(r), \tag{3.18}$$

where $V^J_{j'l',jl}(r)$ is the potential matrix in the basis (3.17). The term on the right-hand-side of

(3.18) is the *driving term* for a given initial (scattering) and final (bound) state of the system, each respectively characterized by the quantum numbers (j, l) and (α, J), where α is a channel index. The driving term is a real quantity resulting from the dipolar coupling of the initial and final states within the dipolar approximation, given by

$$\lambda_{jl}^{\alpha J}(r) = -2m \int d\widehat{r}\, d\widehat{Z}\; Y_{jl}^{JM}(\widehat{r}, \widehat{Z}) \mu(\overrightarrow{r}, \widehat{Z}) \psi_{\alpha J}^{f}(\overrightarrow{r}, \widehat{Z}), \tag{3.19}$$

where m is the reduced mass of the system. The final wavefunctions of the system are calculated in the lab frame and expanded in the basis (3.17):

$$\psi_{\alpha J}^{f}(\overrightarrow{r}, \widehat{Z}) = \frac{1}{r} \sum_{jl} \omega_{jl}^{JM}(r)\; Y_{jl}^{JM}(\widehat{r}, \widehat{Z}). \tag{3.20}$$

The superscript f indicated that this is a final state of the system and $\omega_{jl}^{JM}(r)$ is the radial part of the final wavefunction.

The two sets of DBS wavefunctions — obtained with the potentials V_{ai} and V_{dip} — are then used to calculated REA cross sections in the same basis of 40 rotational levels. The REA cross sections are given by the following:

$$\sigma_f^{\text{REA}} = \frac{g_a}{g_n} \frac{8\pi^2}{3k_e^2 c^3} \sum_{J,\alpha} \omega_\alpha^3 |d_{j,J}^{\alpha J'}|^2, \tag{3.21}$$

where $d_{j,J}^{\alpha J}$ — obtained from the driving term[96] — is the transition dipole moment, ω_α is the frequency of the emitted photon (not to be confused with the radial part of (3.20)), and g_a and g_n are, respectively, the spin degeneracy factors of the anion and the neutral.

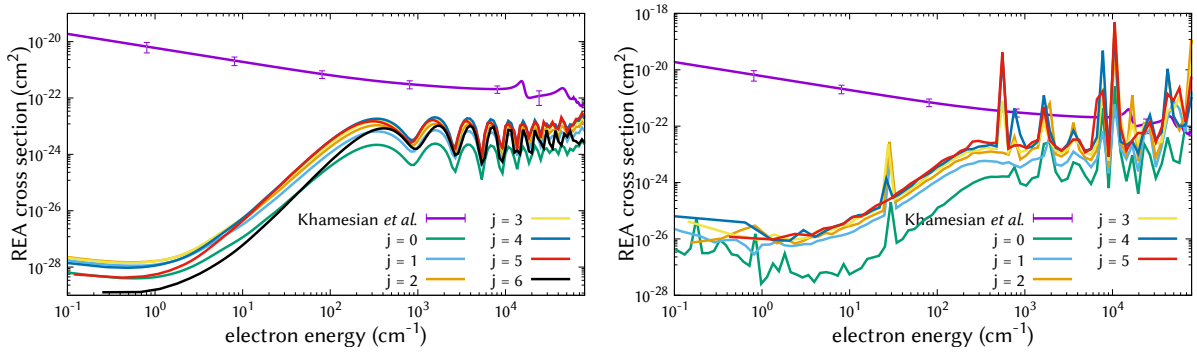

Figure 3.3: The REA cross sections for different initial rotational states j of C_3N^- using the V_{ai} (left) and V_{dip} (right) potentials. The figures show the result (purple curve with error bars) of the previous REA study[22]. The error bars on the curve represent the uncertainty of the model used in that study.

Results

The cross section is summed over J, i.e. over the possible DBSs. Figure 3.3 shows the REA cross sections for different initial rotational states of C_3N using both potentials and the result of the previous REA investigation[22], which considered the ground electronic state of C_3N^- to be the final state. For scattering energies below 0.1 eV, the present cross sections are much smaller than those of Khamesian et al.[22], which is expected for low collisions where the overall magnitude of the cross section is dominated by the ω_α^3 term in (3.21). ω_α is much smaller for a transition to a DBS than for a transition to the ground anionic state. While the DBSs sit a few wavenumbers below the neutral's potential energy surface, the electron affinity of C_3N^- was determined experimentally to be $\sim$34727 cm^{-1} [26]. The present cross sections approach that of Khamesian et al.[22], approximately, at larger scattering energies.

Figure 3.4 shows a subset of the driving terms included in the present calculations. The oscillatory nature of the driving terms at smaller r manifest as the high-energy oscillations of the REA cross sections (see Figure 3.3).

The present cross sections are even smaller at energies relevant for dense interstellar cloud

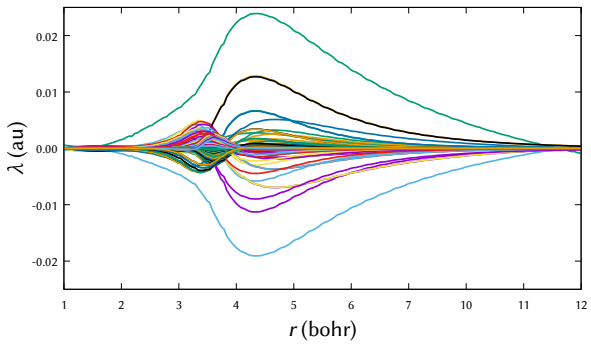

Figure 3.4: Driving terms between various initial and final states of the system.

chemistry than those of Khamesian et al.[22]. The present study does consider dipole scattering states (DSSs, dipole states with energies just above the ionization threshold), which suggested by Carelli et al.[99] to enhance REA cross sections because of their large overlap with DBSs and small dissipation energies. However, the emitted photon's frequency remains small and may not be enough to compensate for the larger transition dipole moment one might obtain by starting from a DSS. Nonetheless, such an investigation is beyond the scope of the current study and should be investigated to draw any conclusions more tentative than this.

The work detailed here on REA has been published:

- Joshua Forer, Viatcheslav Kokoouline, and Thierry Stoecklin. Radiative electron attachment to rotating C_3N through dipole-bound states. *Physical Review A*, 107(4):043117, 2023

CHAPTER 4: DISSOCIATIVE RECOMBINATION AND ROVIBRONIC EXCITATION

Of the multitude of processes that can occur when an electron collides with a molecule, DR of molecular cations is among the most complicated to study, if not the most complicated, due to the different available breakup modes and how Rydberg series drive the reaction. The total energy of the electron-ion system is the sum of the incident electron's kinetic energy E_{el} and the channel energy of the ion E_i, the latter of which is determined by the initial state i of the ion, i.e.

$$E_{tot} = E_i + E_{el}. \tag{4.1}$$

Depending on the theoretical treatment, the channels could have any combination of electronic, vibrational, or rotational resolution. Molecular ions found in diffuse clouds are expected to be in the ground rovibronic state due to *radiative cooling*, where a molecule loses energy via spontaneous photoemission.

Upon collision, assuming DR takes place, potential energy binding the ion is transferred to kinetic energy as it fragments. The asymptotic limit of the potential energy curve through which the system dissociates is know as the *dissociation energy*, E_{diss}, which is the difference between E_{tot} and the kinetic energy of the products, E_{kin}:

$$E_{tot} = E_{diss} + E_{kin}. \tag{4.2}$$

DR, of course, is not the only process that can occur during an electron-molecule collision. The main competitor, at low energies, is *autoionization*, an electron escapes from the neutral molecule formed by the electron-ion system during the collision. This could be elastic scattering or inelastic scattering, where the target ion is (de-)excited by transferring energy to the scattered electron.

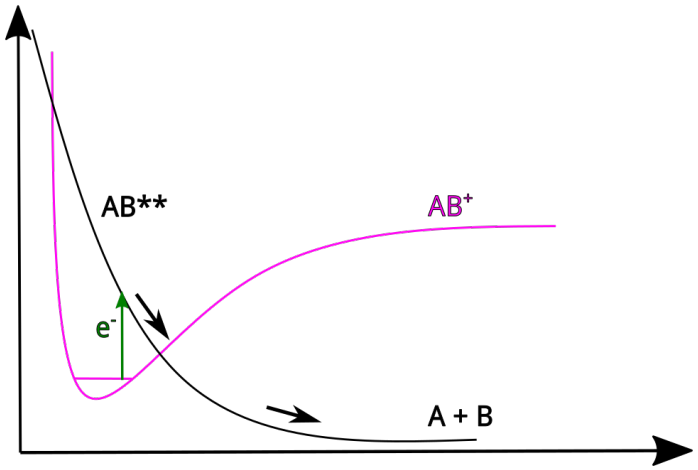

Figure 4.1: Sketch of the direct DR mechanism.

DR — resonant and nonresonant

DR is often separated into two mechanisms: *direct* and *indirect* or, respectively, *resonant* and *nonresonant* DR. In the direct mechanism, the electron is captured adiabatically into a dissociative state (resonance) of the neutral, as depicted by Figure 4.1. Direct DR is more likely to take place in systems where the dissociative resonance crosses the relevant initial potential energy curve in or slightly to the right of the Franck-Cordon region, and typically at higher electron energies. Indirect DR described the non-adiabatic process by which an electron is captured into a Rydberg state of the neutral, after which the system transitions to the above-mentioned resonance. Indirect DR can be further separated into the *core-unexcited* and *core-excited* indirect mechanisms, as shown in Figure. 4.2 The term "core" refers to the target ion in the sense that the singly excited Rydberg state is made up of the ionic core and the captured Rydberg electron. For systems with low-lying electronic states like CH^+, these core-excited states become more important at low electron energies. In the case of CH^+, core-excited states were found to have a significant effect on the experimental[101]

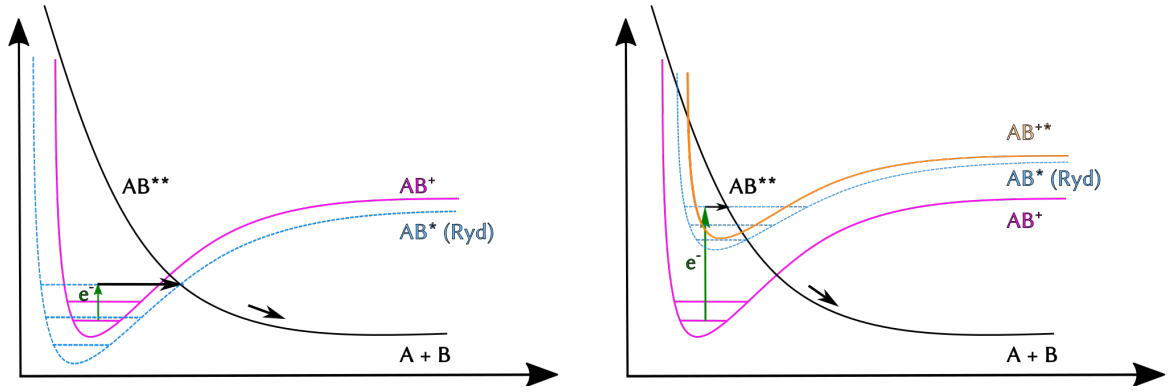

Figure 4.2: Sketch of the core-unexcited (left) and core-excited (right) indirect DR mechanisms.

and theoretical[54,57] cross sections. The Rydberg state in which the incoming electron could be captured can belong to any of the ion's electronic states that are energetically accessible. These could be vibrationally or rotationally excited cores in the ground or excited electronic states. The incoming electron imparts some of its energy to the ionic core, exciting it in some combination of its electronic, vibrational, or rotational degrees of freedom. Once the electron is captured, it continues to exchange energy with the ionic core until the system either autoionizes or proceeds to the dissociative resonant state. For completely or near-completely indirect DR, i.e. where the indirect mechanism's contribution is negligible, rotation dominates low-energy DR[35,36].

Low-energy DR of diatomic ions

To study low-energy DR in systems with low-lying electronic states, which is generally difficult due to the many low-lying electronic resonances, we have developed a method that incorporates R-matrix theory, frame transformations with a complex absorbing potential (CAP), and MQDT. The method will be presented generally, then molecule-specific details will be mentioned.

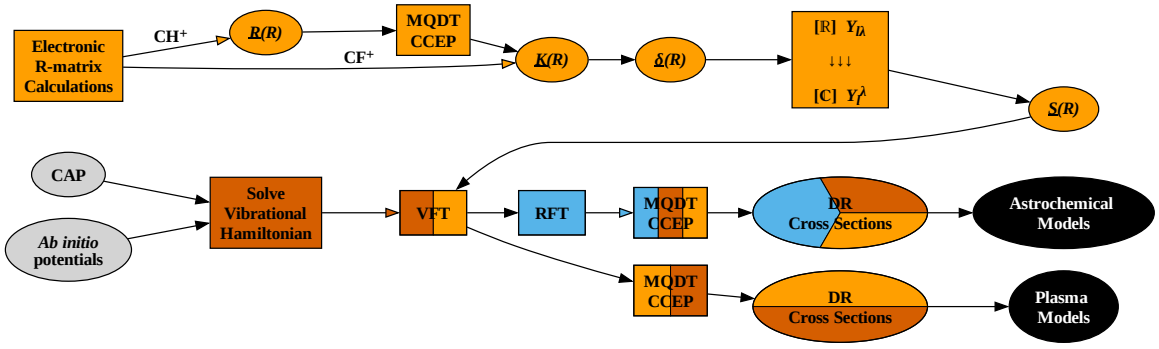

Figure 4.3: Procedure flowchart of the present diatomic DR method. The different colors represent the degrees of freedom included at different steps in the method: electronic (**orange**), vibrational (**vermillion**), and rotational (**blue**). The boxes represent various procedures applied to their input matrices. The **MQDT** procedure applied to the R-matrix is given by (2.74). The other MQDT (**rovibronic** and **vibronic**) procedures applied to the S-matrix after frame transformations are given by (4.23, 4.24) for CH^+ and (4.25, 4.26) for CF^+. The transformation of the δ-matrix from a basis of real spherical harmonics to complex spherical harmonics $\left(\mathbf{Y}_{l\lambda} \rightarrow \mathbf{Y}_l^{\lambda}\right)$ is given by (B.24). **VFT** is the vibrational frame transformation (2.80). **RFT** is the rotational frame transformation (4.16, 4.17). The incorporation of the present DR data into plasma and astrochemical models does not fall within the scope of this study; their inclusion in the diagram is simply to suggest how the present method might be interfaced with other applications.

Fixed-nuclei electronic-scattering matrix

The first steps in the approach are to identify which electronic states of the ion we want to include in the approach and then perform R-matrix scattering calculations at several values of the internuclear distance (R) such that these states are included in the calculations. The R-matrix calculations produce K-matrices, as per (2.72), in a basis of open channels at some scattering energy. Details on obtaining the K-matrices differ for CH^+ and CF^+, so they will be discussed in the relevant molecule-specific subsections that follow. The approach assumes an energy-independent K-matrix $\underline{K}^{\Lambda}(R)$ and, therefore, an energy-independent S-matrix $\underline{S}^{\Lambda}(R)$ (2.23). The matrices are in a basis of electronic channels $|nl\lambda\rangle$, where n identifies the electronic state of the target, l is the orbital

angular momentum quantum number of the scattering electron, and λ is the projection of $\vec{l}$ on the molecular frame. We consider $l = 0 - 2$ for both CH^+ and CF^+, yielding up to (some channels are eliminated in the CH^+ R-matrix before obtaining the K-matrix) 9 partial waves attached to each electronic state n.

Elements of the K-matrix, however, exhibit strong discontinuities as functions of R when the eigenphase-shifts $\pi\mu$ approach $\pm\pi/2$ (mod π) because the K-matrix eigenvalues behave as $tan(\pi\mu)$ (4.4). From the discontinuous K-matrix, we construct the continuous matrix of scattering phase-shifts, the δ-matrix, whose eigenvalues are the phases in the argument of the S-matrix in (2.24). The K-matrix and δ-matrix are formally related by

$$\underline{K}^{\Lambda}(R) = \tan\left(\underline{\delta}^{\Lambda}(R)\right). \tag{4.3}$$

In practice, we first diagonalize $\underline{K}(R)$ across all considered values of R,

$$\underline{K}^{\Lambda}(R) = \underline{U}(R)\underline{K}^{diag}(R)\underline{U}(R)^{\dagger} = \underline{U}(R)\tan\left(\pi\underline{\mu}^{diag}\right)(R)\underline{U}(R)^{\dagger}, \tag{4.4}$$

where $\underline{K}^{diag}$ is the diagonal matrix whose nonzero entries are the eigenvalues of $\underline{K}(R)$. The superscript Λ is again used to indicated that the electronic matrices $\underline{K}^{\Lambda}(R)$, $\underline{\delta}^{\Lambda}(R)$, and $\underline{S}^{\Lambda}(R)$ are block diagonal with respect to Λ. We then construct $\underline{\delta}^{\Lambda}$ by taking the arctangent of $\underline{K}^{diag}(R)$ and the using the same unitary matrices $\underline{U}(R)$ in (4.4):

$$\underline{\delta}^{\Lambda}(R) = \underline{U}^{\dagger}(R)\arctan\left(\underline{K}^{diag}(R)\right)U(R) = \underline{U}^{\dagger}(R)\pi\underline{\mu}^{diag}(R)U(R). \tag{4.5}$$

With appropriate branch choices in (4.5), the matrix $\underline{\delta}^{\Lambda}(R)$ is continuous as a function of R. Figure 4.4 compares K-matrix elements with some of the δ-matrix elements to illustrate this.

The K-matrices, and therefore the δ-matrices, are calculated in the Abelian C_{2v} point group in a basis of real spherical harmonics $Y_{l\lambda}$. We transform the δ-matrix from this basis to the basis

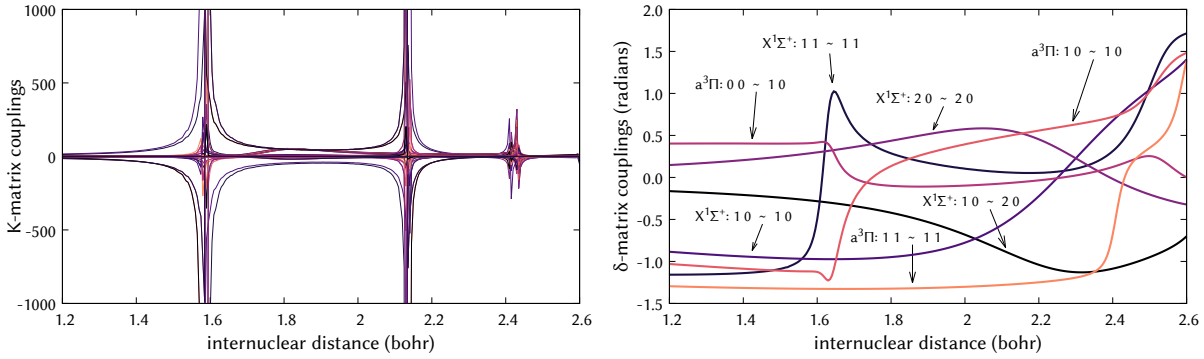

Figure 4.4: K-matrix couplings and scattering phase-shifts plotted as a function of the internuclear distance R for CH^+. The notation for each coupling's partial waves takes the form $l\lambda \sim l'\lambda'$. All K-matrix couplings are shown, but only some δ-matrix couplings are plotted. Large jumps in the scattering phase-shifts occur around the same positions of the K-matrix discontinuities.

of complex spherical harmonics Y_l^λ, which are better adapted for the natural non-Abelian $C_{\infty v}$ point group of heteronuclear diatomic ions, such that the electronic channels $|nl\lambda\rangle$ have a definite projection of the total angular momentum. Before applying the frame transformations, we apply a basis transformation to the δ-matrix. The channel functions of the incident electron and channel functions of the target electronic state undergo the same basis transformation; both basis transformations commute. The channel functions for the incident electron, given entirely by l and λ, are transformed from $Y_{l\lambda}$ to Y_l^λ, as per (B.24). Before the transformation, they belong to the following irreps in the C_{2v} point group:

$$Y_{l\lambda} \begin{cases} A_1: & \lambda \geq 0, & \lambda \text{ even} \\ A_2: & \lambda < 0, & \lambda \text{ even} \\ B_1: & \lambda > 0, & \lambda \text{ odd} \\ B_2: & \lambda \geq 0, & \lambda \text{ odd} \end{cases} \tag{4.6}$$

The incident electron channel functions transformation is block diagonal over l, i.e. each $Y_{l\lambda}$ is transformed into Y_l^λ only for the same value of l. The electronic states considered in the case

of CH^+ and CF^+ are of Σ^+ (ground state) or Π (excited states) symmetry. The Σ states behave behave as Y_{00} and, therefore, undergo only an identity transformation. The Π states, however, are doubly degenerate in the $C_{\infty v}$ point group and are considered separately in the C_{2v} point group as *irreducible representations* (irreps) B_1 and B_2 with, respectively, $\Lambda = 1$ and $\Lambda = -1$, chosen to be consistent with (4.6). Similarly to the incident electron channel function transformation being transformed according to (B.24), the transformation is only carried out between corresponding degenerate target states:

$$\begin{pmatrix} \Pi^+ \\ \Pi^- \end{pmatrix} = \frac{1}{\sqrt{2}} \begin{pmatrix} -1 & -i \\ 1 & -i \end{pmatrix} \begin{pmatrix} \Pi_{B_1} \\ \Pi_{B_2}, \end{pmatrix} \tag{4.7}$$

where $\Pi^{\pm}$ are the complex-values channel functions for the target electronic states with projection ± 1, and Π_{B_1} and Π_{B_2} are, respectively, the real-values channel functions for the target electronic states of B_1 and B_2 symmetry. It should be noted that (4.7) is just a specific case of (B.24).

After this transformation is performed on $\underline{\delta}^{\Lambda}(R)$, we convert it to the S-matrix via the formal relation

$$\underline{S}^{\Lambda}(R) = e^{2i\pi\underline{\delta}^{\Lambda}(R)}, \tag{4.8}$$

in a similar manner as before. We diagonalize $\underline{\delta}^{\Lambda}(R)$,

$$\underline{\delta}^{\Lambda}(R) = \underline{U}(R)\underline{\delta}^{diag}(R)\underline{U}^{\dagger}(R), \tag{4.9}$$

to obtain the unitary matrices $\underline{U}(R)$. These $\underline{U}(R)$ diagonalize $\underline{K}^{\Lambda}(R)$, $\underline{\delta}^{\Lambda}(R)$, and $\underline{S}^{\Lambda}(R)$ if they are in the same basis of complex-valued spherical harmonics, and are used to obtain $\underline{S}^{\Lambda}(R)$ in a similar manner to that of (4.5):

$$\underline{S}^{\Lambda}(R) = \underline{U}^{\dagger}(R)e^{2i\pi\underline{\delta}^{diag}(R)}\underline{U}(R), \tag{4.10}$$

which is unitary by construction. The form of (4.10) is reminiscent of the single-channel definition

of the S-matrix (2.11).

Rovibronic frame transformation

The electronic S-matrix, $\underline{S}^{\Lambda}(R)$, is expressed in the basis of electronic channels $|nl\lambda\rangle$, calculated in the body frame. Using frame transformations, the R-dependent body-frame S-matrix will be converted to an R-independent lab-frame S-matrix with additional vibrational and rotational channel indices. Two frame transformations are carried out in series: the vibrational frame transformation and then the rotational frame transformation.

Vibrational states of the ion must be calculated to carry out the vibrational frame transformation. In this approach, bound states and continuum states are needed. Bound states are exactly that — bound vibrational states within an electronic state of the ion with a vibrational energy that is lower than the dissociation limit of the attached electronic state. Continuum states — although still attached to an electronic state of the ion — have a vibrational energy that is above the respective state's dissociation limit. The boundary conditions for each type of vibrational state is important: bound states tend to 0 at the endpoints of the R interval while continuum states have outgoing-wave behavior, representing outgoing dissociative flux. To obtain vibrational states of the ion, the vibrational Schrödinger equation (2.79) needs to be solved. The potential, however, is non-real. In addition to the internuclear potential, a purely imaginary contribution is added of the form[102]

$$V_{CAP}(R) = i\eta N e^{-2L/(R-R_0)}, \tag{4.11}$$

where N is a normalization constant, η is the CAP strength, L is the CAP length (the length of the imaginary part), and R_0 is where the imaginary part of the CAP begins, (all chosen according to Vibok and Balint-Kurti[102]). CAP parameters used in the vibrational frame transformation of CH^+ and CF^+ are given in Table 4.1.

The vibrational Hamiltonian, then, is complex symmetric and **not** Hermitian. Therefore,

Table 4.1: CAP parameters used in the vibrational frame transformation in the DR of CH^+ (top) and CF^+ (bottom).

target	η (au)	N	L (bohr)	R_0 (bohr)
CH^+	0.060	13.22	1.2	4.8
CF^+	0.066	13.22	2.0	5.0

the eigenenergies (vibronic channel energies) are, in general, complex:

$$E_{nv} = \varepsilon_{nv} - i\frac{\Gamma}{2}, \tag{4.12}$$

,where ε_{nv} is the vibrational energy (real) of the ion and Γ is the width of the state. Γ is negligible only for bound vibrational states. The vibrational wavefunctions $\phi_{nv}(R)$, then, obey slightly different normalization:

$$\int dR \phi_{n'v'}(R)\phi_{nv}(R) = \delta_{nn'}\delta_{vv'}. \tag{4.13}$$

The eigenenergies are real for bound vibrational states, but have non-negligible imaginary components for continuum state. Because the functions $\phi_{nv}(R)$ obey the orthogonality condition (4.13) where neither wavefunction is complex-conjugated, we define unitarity for the vibronic S-matrix slightly differently (described in Appendix C). Given the electronic S-matrix $\underline{S}^{\Lambda}(R)$, we define two vibronic S-matrices:

$$\underline{S}^{\Lambda}_{n'v'l'\lambda',nvl\lambda} = \int dR \phi_{n'v'}(R)\underline{S}^{\Lambda}_{n'l'\lambda',nl\lambda}(R)\phi_{nv}(R) \tag{4.14}$$

and

$$\underline{S}^{\Lambda\ddagger}_{nvl\lambda,n'v'l'\lambda'} = \int dR \phi_{nv}(R)\underline{S}^{\Lambda\dagger}_{nl\lambda,n'l'\lambda'}(R)\phi_{n'v'}(R). \tag{4.15}$$

Unitary subblocks of $S^{\Lambda\dagger}$ (the Hermitian adjoint of the vibronic matrix S^{Λ} (4.14)) and $S^{\Lambda\ddagger}$ (the

matrix (4.15)) corresponding to such bound states are identical. The only differences arise for blocks corresponding to continuum-state wavefunctions. As detailed in (C), $S^{\Lambda}S^{\Lambda\ddagger} = I$. This marks the end of the vibrational frame transformation.

The next step is the rotational frame transformation (2.81), applied to both vibronic S-matrices (4.14) and (4.15):

$$\underline{S}^{J}_{n'v'j'\mu'l',nvj\mu l} = \sum_{\Lambda}\sum_{\lambda'\lambda}(-1)^{l+l'+\lambda+\lambda'}C^{j'\mu'}_{l'-\lambda',J\Lambda}\underline{S}^{\Lambda}_{n'v'l'\lambda',nvl\lambda}C^{j\mu}_{l-\lambda,J\Lambda}, \tag{4.16}$$

$$\underline{S}^{J\ddagger}_{nvj\mu l,n'v'j'\mu'l'} = \sum_{\Lambda}\sum_{\lambda'\lambda}(-1)^{l+l'+\lambda+\lambda'}C^{j'\mu'}_{l'-\lambda',J\Lambda}\underline{S}^{\Lambda\ddagger}_{n'v'l'\lambda',nvl\lambda}C^{j\mu}_{l-\lambda,J\Lambda}. \tag{4.17}$$

The superscript J denotes that the rovibronic S-matrices on the left-hand-side of (4.16) and (4.17) are block-diagonal with respect to the magnitude of the system's total angular momentum:

$$\vec{J} = \vec{j} + \vec{l}, \tag{4.18}$$

$$\Lambda = \mu + \lambda. \tag{4.19}$$

where $\vec{j}$ is the total angular momentum of the target ion and Λ, λ, and μ are the projections of $\vec{J}$, $\vec{l}$ and $\vec{j}$ on the molecular axis. The rotational frame transformation is still unitary, i.e. $S^{J}S^{J\ddagger} = I$. The rovibronic channels E_{nvj} energies are related to the vibronic channels energies by

$$E_{nvj} = E_{nv} + B_{nv}j(j+1), \tag{4.20}$$

where B_{nv} is the rotational constant of the ion, calculated for the vibronic state $|nv\rangle$.

DR cross sections and rate coefficients

Cross sections for DR from some initial channel are calculated for several electron energies (and therefore values of E_{tot}) (4.1). The rovibronic S-matrices S^{J} and $S^{J\ddagger}$ are in a basis of asymptoti-

cally open channels, but the number of open channels may change as a function of E_{tot}. In the even where at least one channel is asymptotically closed, which is the case for low-energy collisions, we use the channel-elimination procedure (2.68, 2.64), applied separately to S^J and $S^{J\ddagger}$. They are first partitioned into blocks defined by n_o open (o) channels and n_c closed (c) channels:

$$\underline{S}^J = \begin{pmatrix} \underline{S}_{oo} & \underline{S}_{oc} \\ \underline{S}_{co} & \underline{S}_{cc} \end{pmatrix}, \quad \underline{S}^{J\ddagger} = \begin{pmatrix} \underline{S}^\ddagger_{oo} & \underline{S}^\ddagger_{oc} \\ \underline{S}^\ddagger_{co} & \underline{S}^\ddagger_{cc} \end{pmatrix}. \tag{4.21}$$

Then, the diagonal $n_c \times n_c$ eigen-quantum-defect matrix $\underline{\beta}(E_{tot})$ is constructed in the same basis of channels as $\underline{S}_{cc}$ and $\underline{S}^\ddagger_{cc}$ as

$$\underline{\beta}_{i'i}(E_{tot}) = \frac{\pi}{\sqrt{2\left(E_i - E_{tot}\right)}}\delta_{ii'}, \tag{4.22}$$

where i and i' run over closed channels, and E_i is the channel energy E_{nvj} (4.20). We can then proceed with the closed-channel elimination procedure (2.68), applied to both S-matrices:

$$\begin{aligned} \underline{S}^{J,CE}(E_{tot}) &= \underline{S}_{oo} - \underline{S}_{co}\left[\underline{S}_{cc} - \left(\underline{q}\cos(\underline{\beta}) + i\underline{q}^{-1}\sin(\underline{\beta})\right)^{-1}\left(\underline{q}\cos(\underline{\beta}) - i\underline{q}^{-1}\sin(\underline{\beta})\right)\right]^{-1}\underline{S}_{co} \\ \underline{S}^{J,phys}(E_{tot}) &= \left[(\underline{q}^{-1} - \underline{q}) + (\underline{q}^{-1} + \underline{q})\underline{S}^{J,CE}\right]\left[(\underline{q}^{-1} + \underline{q}) + (\underline{q}^{-1} - \underline{q})\underline{S}^{J,CE}\right]^{-1}, \end{aligned} \tag{4.23}$$

and

$$\begin{aligned} \underline{S}^{J,CE\ddagger}(E_{tot}) &= \underline{S}^\ddagger_{oo} - \underline{S}^\ddagger_{co}\left[\underline{S}^\ddagger_{cc} - \left(\underline{q}\cos(\underline{\beta^*}) - i\underline{q}^{-1}\sin(\underline{\beta^*})\right)^{-1}\left(\underline{q}\cos(\underline{\beta^*}) + i\underline{q}^{-1}\sin(\underline{\beta^*})\right)\right]^{-1}\underline{S}^\ddagger_{co}, \\ \underline{S}^{J,phys\ddagger}(E_{tot}) &= \left[(\underline{q}^{-1} - \underline{q}) + (\underline{q}^{-1} + \underline{q})\underline{S}^{J,CE\ddagger}\right]\left[(\underline{q}^{-1} + \underline{q}) + (\underline{q}^{-1} - \underline{q})\underline{S}^{J,CE\ddagger}\right]^{-1}. \end{aligned} \tag{4.24}$$

For $\underline{q} = \underline{I}$, (4.23) and (4.24) reduce, respectively, to

$$S^{J,phys}(E_{tot}) = \underline{S}_{oo} - \underline{S}_{oc}\left(\underline{S}_{cc} - e^{-2i\underline{\beta}}\right)^{-1}\underline{S}_{co} \tag{4.25}$$

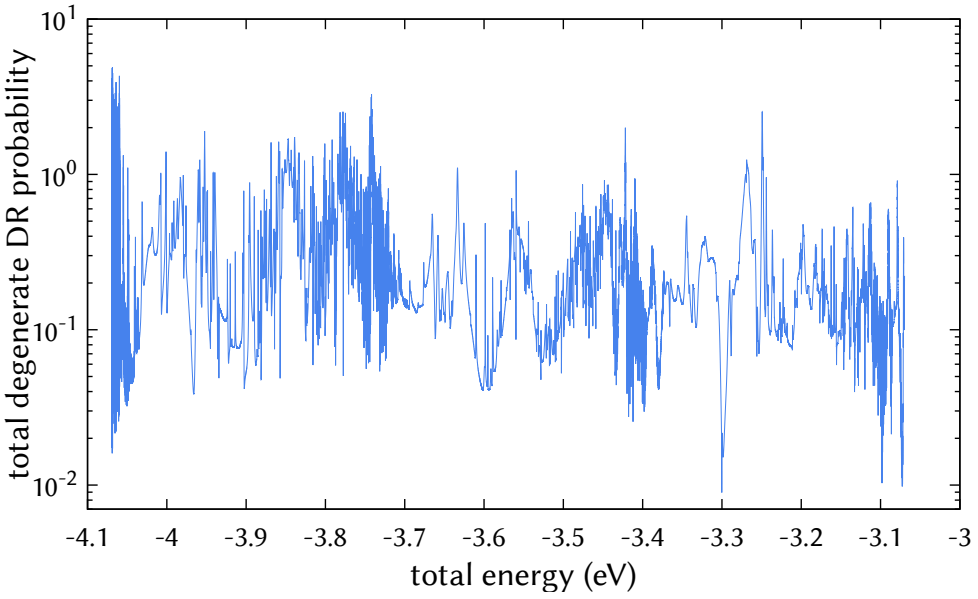

Figure 4.5: Sum of degenerate DR probabilities $P^J_{1000}(E_{tot})$ as a function of total energy from the ground rovibronic state of CH^+.

and

$$S^{J,phys\ddagger}(E_{tot}) = \underline{S}^{\ddagger}_{oo} - \underline{S}^{\ddagger}_{oc}\left(\underline{S}^{\ddagger}_{cc} - e^{2i\underline{\beta}^*}\right)^{-1}\underline{S}^{\ddagger}_{co} \tag{4.26}$$

just as (2.68) reduces to (2.64) under the same condition. It is important to note that between (4.23) and (4.24), as well as between (4.25) and (4.26), the sign of the real part of β changes. Details on $\underline{q}$ will be given for each target molecule.

The matrices $\underline{S}^{J,phys}(E_{tot})$ and $\underline{S}^{J,phys\ddagger}(E_{tot})$ are the physical S-matrices introduced in (2.64, 2.68). They are used to calculate the probability for DR to occur at that E_{tot}, starting from some initial state $|nvj\mu\rangle$ and a given J:

$$P^J_{nvj\mu}(E_{tot}) = (2J+1)\sum_l \left[1 - \sum_{l'}\sum_{n'v'j'\mu'} \underline{S}^{J,phys}_{n'v'j'\mu'l',nvj\mu l}(E_{tot})\underline{S}^{J,phys\ddagger}_{nvj\mu l,n'v'j'\mu'l'}(E_{tot})\right]. \tag{4.27}$$

The quantity $P^J(E_{tot})$ can exceed 1 for $J > 0$, as shown in Figure 4.5. It accounts for the rotational

degeneracy $(2J+1)$ and could be referred to as a degenerate probability. $P^J(E_{tot})/(2J+1)$ does not exceed 1 because the physical S-matrix is subunitary and the rotational degeneracy is not included. From (4.27), the DR cross section for each J from some initial channel $|nvj\mu\rangle$ can be calculated,

$$\sigma^J_{nvj\mu}(E_{el}) = \frac{\pi}{k^2}\frac{1}{2j+1}P^J_{nvj\mu}(E_{tot}), \tag{4.28}$$

where $k = \sqrt{2m_eE_{el}}$ is the magnitude of the incident electron's wave vector. Taking the sum over J of (4.28) gives us the total DR cross section from the initial channel $|nvj\mu\rangle$:

$$\sigma_{nvj\mu}(E_{el}) = \sum_J \sigma^J_{nvj\mu}(E_{el}). \tag{4.29}$$

In case the rotational frame transformation is not applied, which may be desirable when comparing to results that also lack rotational resolution, (4.27, 4.28, and 4.29) take on slightly different forms. Recalling that the vibronic S-matrices are in the basis of channels vibronic channels $|nvl\lambda\rangle$, the closed-channel elimination procedure (4.23 – 4.26) is applied in the same way to $\underline{S}^{\Lambda}$ and $\underline{S}^{\Lambda\ddagger}$ to produce, respectively, $\underline{S}^{\Lambda,phys}(E_{tot})$ and $\underline{S}^{\Lambda,phys\ddagger}(E_{tot})$. The vibronic DR cross section from some initial channel $|nv\rangle$, then, is given by

$$\sigma_{nv}(E_{el}) = \frac{\pi}{k^2}\sum_{l\lambda}\left[1 - \sum_{l'\lambda'}\sum_{n'v'}\underline{S}^{\Lambda,phys}_{n'v'l'\lambda',nvl\lambda}(E_{tot})\underline{S}^{\Lambda,phys\ddagger}_{nvl\lambda,n'v'l'\lambda'}(E_{tot})\right]. \tag{4.30}$$

Convolving and averaging theoretical results

Cross sections obtained from (4.30) or (4.29) benefit from computer precision, but experimental measurements, with which we should compare our results, typically have much larger uncertainties in their measurements. This is not to say that theoretical models and numerical methods do not have uncertainties in their accuracy, but that the theoretical results can be calculated for electron energies with precision down to the numerical precision of the data types used to hold such val-

ues. For example, Figure 4.11 shows DR cross sections from experimental measurements[39] and unconvolved theoretical results of the present study. The theoretical results have a large number of resonant structures, most of which are not present in the experimental data. It is difficult to compare the two without taking the difference in energy resolution into account — resonances in reaction cross sections can have peaks that are orders of magnitude apart.

Theoretical data, e.g. a cross section function $\sigma(E)$, can be *convolved* with a function $f(E)$ including experimental energy precision that takes into account neighboring values:

$$\sigma^{conv}(E) \equiv \frac{\int dE' \sigma(E') f(E - E')}{\int dE' f(E - E')}. \tag{4.31}$$

The popular choices for the function f are a Gaussian distribution,

$$\sigma^{conv}(E) = \frac{\int_0^\infty dE' \sigma(E') e^{-(E-E')^2/(2\gamma^2)}}{\int_0^\infty dE' e^{-(E-E')^2/(2\gamma^2)}}, \tag{4.32}$$

and a Lorentz or Cauchy distribution,

$$\sigma^{conv}(E) = \frac{\int_0^\infty dE' \sigma(E') \frac{1}{\pi} \frac{\gamma}{(E-E')^2+\gamma^2}}{\int dE' \frac{1}{\pi} \frac{\gamma}{(E-E')^2+\gamma^2}}. \tag{4.33}$$

In (4.33) and (4.32), γ is a convolution width in the same units of energy as E and E'. This can be chosen arbitrarily to smooth out resonances as the user wishes, but γ is often taken from an experiment against which theoretical results are compared. Common values for γ range from 0.1 to a few meV. As demonstrated by Figure 4.17, many resonant features are lost with increasing convolution width.

Additionally, the data could be convolved with a Maxwell-Boltzmann distribution to pro-

duce state-selected rate coefficients:

$$\alpha_i^{kin} = \frac{\int_0^\infty \sigma_i(E_{el}) e^{-E_{el}/(k_B T)} \sqrt{E_{el}} dE_{el}.}{\int_0^\infty e^{-E_{el}/(k_B T)} \sqrt{E_{el}} dE_{el}.} \tag{4.34}$$

This is relevant to a situation in in which the molecules and electrons are in thermal equilibrium, such as in diffuse interstellar clouds. For such a comparison, it is important to retain the cross sections from the ground rovibronic state, given that this is how the ions are expected to be found in diffuse clouds. However, one may still wish to average the data over initial states:

$$\alpha^{kin} = \frac{\sum_i \alpha_i(E_{el})(2j+1) e^{-E_i/(k_B T)}.}{\sum_i (2j+1) e^{-E_i/(k_B T)}.} \tag{4.35}$$

In (4.34, 4.35), i identifies initial channels and E_i are the corresponding channel energies, and $\sigma_i(E_{el})$ is the cross section for some reaction, e.g. DR or rotational excitation. As before, j in (4.35) can be taken to be zero for cross sections that are not rotationally resolved.

Storage ring beams, like at the CSR[39], may require a more complicated convolution and averaging procedure to account for experimental uncertainties. One such example is in merged-beam experiments, where different energy spreads parallel and perpendicular to the beam direction need to be considered. Additionally, the temperature T of the ion beam must be considered because some ions may be rovibronically excited, and their contribution may not be removable from the experimental results. An anisotropic Maxwell-Boltzmann convolution[103] for such a situation has

may be useful:

$$\sigma^{conv}(E_\parallel) = \frac{\sum_i \int_{-\infty}^{\infty} du_\parallel \int_0^\infty dE_\perp \sigma\left((v_\parallel + u_\parallel)^2/2 + E_\perp\right) w_i^{\gamma_\parallel,\gamma_\perp}\left(T, u_\parallel, E_\perp\right)}{\sum_i \int_{-\infty}^{\infty} du_\parallel \int_0^\infty dE_\perp w_i^{\gamma_\parallel,\gamma_\perp}\left(T, u_\parallel, E_\perp\right)} \tag{4.36}$$

$$w_i^{\gamma_\parallel,\gamma_\perp}(T, u, E) = (2j+1)e^{-E_i/(k_B T)} e^{-u^2/(2\gamma_\parallel)} e^{-E/\gamma_\perp}.$$

In (4.36), $\gamma_\parallel$ and $\gamma_\perp$ are the convolution widths for the parallel and perpendicular direction, respectively, and E_i is the energy of the i^{th} channel. The velocity of the electrons, relative to the molecule, is given by $\vec{v} = \vec{v}_\parallel + \vec{u}_\parallel + \vec{u}_\perp$. The measurements are made at the velocity $\vec{v}_\parallel$; $\vec{u}_\parallel$ and $\vec{u}_\perp$ are the parallel and perpendicular components of the energy spread that contribute to the actual velocity $\vec{v}$. The parallel and perpendicular energy components are $E_\parallel = m_e v_\parallel^2/2$ and $E_\perp = m_e u_\perp^2/2$ The summation runs over all considered initial states i. j can be taken to be zero for data that is not rotationally resolved.

Low-energy DR of CF^+

The major differences between the present method's application to study CF^+ and CF^+ lie in obtaining K-matrices from the fixed-nuclei R-matrix calculations. Figure 4.3 has two arrows (edges) coming from the R-matrix calculations. The edge labelled CF^+ bypasses the $\underline{\boldsymbol{R}}(\boldsymbol{R})$ and **MQDT CCEP** nodes, pointing directly to the $\underline{\boldsymbol{K}}(\boldsymbol{R})$ node. In a sense, this method is less advanced (developed earlier) than the one applied to CH^+, whose edge does not bypass the two former nodes.

Fixed-nuclei calculations

The lowest three potential energy curves of CF^+ were calculated with in the MRCI method and the correlation-consistent polarized valence double-zeta (`cc-pVDZ`) basis set for internuclear distances R from 2.20 bohr to 2.28 bohr using the `MOLPRO` software suite[88,89]. It should be stressed

that CF^+ is a closed-shell system. At the calculated equilibrium distance of 2.216 bohr, the two lowest states ($X^1\Sigma^+$ and $a^3\Pi$) are separated by $\sim$5 eV — a small enough difference to expect Rydberg states converging to the $a^3\Pi$ state to play an important role in low-energy scattering.

The R-matrix calculations were performed in the CoM frame of CF^+ with an R-matrix radius of $a = 10$ bohr — implemented in UKRMol[104,105,105], accessed via the Quantemol-N interface[106]. The full configuration interaction (FCI) method was used with `cc-pVDZ` basis set to represent the electronic wavefunction of the target. The lowest three electronic target states were considered: $X^1\Sigma^+$, $a^3\Pi$, and $A^1\Pi$. The $1\sigma^2$ and $2\sigma^2$ orbitals were frozen, while the active space contained the 3–8σ and 1–3π orbitals. Virtual orbitals 9–10σ and 4π were used as members of the continuum set in the inner-region calculations. R-matrix calculations were performed for 6 evenly-spaced values of the internuclear distance from $R = 2.20$–2.30 bohr. 25 partial waves (all projections of l =0–4) were used to represent the scattering electron.

The K-matrix is taken directly from the R-matrix calculations in a basis of open channels. To include the effect of the excited states, we evaluated the K-matrices at energies about 0.1 eV above the $A^1\Pi$ state. This is a relatively high energy at the internuclear distance of the $X^1\Sigma^+$ state — about 8 eV — and is a major limitation of this version of the approach. However, the eigenphases above the considered electronic states are almost energy-independent in the region just above the $A^1\Pi$ state, as demonstrated by Figure 4.6. This ensures we do not evaluate the K-matrices near a resonance, which could lead to significant inaccuracy in our energy-independent S-matrix approach.

The number of internuclear distances used in the R-matrix calculations of CF^+ is relatively small (6). The deep electronic potentials make identifying eigenphases from $\underline{K}^\Lambda(R)$ (to correct for branch jumps due to the tangent function (4.4)) difficult to identify across R by comparing inner products of the eigenvectors between geometries — the same method successfully employed for CH^+. A small number of points inside the Franck-Condon region where this procedure was feasible were identified and used to create a sparse grid upon which the matrix $\underline{\delta}^\Lambda(R)$ would be

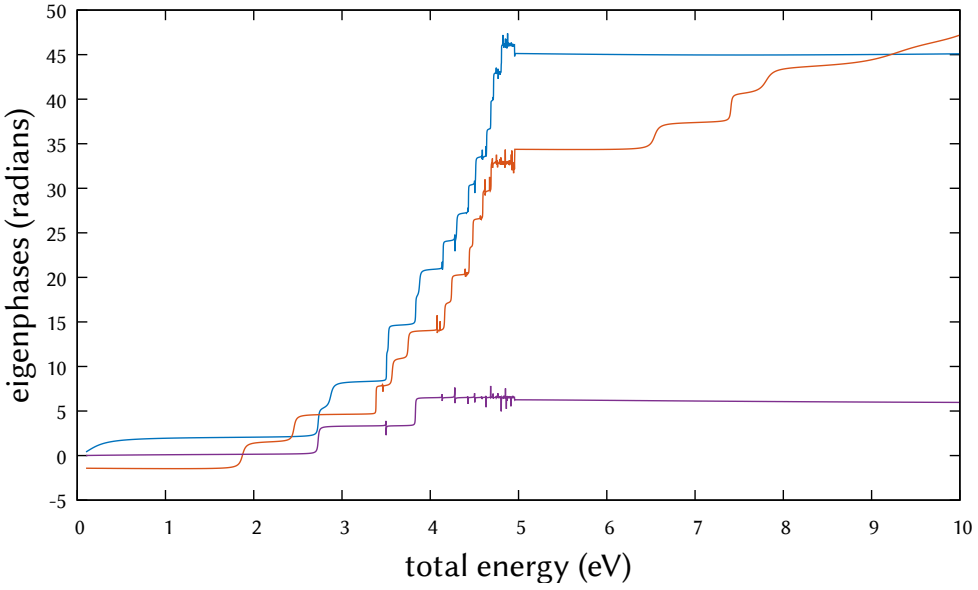

Figure 4.6: CF^+ scattering eigenphases for the different irreducible representations of the C_{2v} point group at $R = 2.20$ bohr.

interpolated to 20 points within the interval [2.20,2.30] bohr. The δ-matrix elements are then held constant at the endpoints and extrapolated outwards with an even spacing to 1.2 and 7.0 bohr so that the vibrational frame transformation (2.80) may be carried out on a sufficiently fine and expansive R-grid. A significant advantage of the δ-matrix is that it is smooth and relatively safe to interpolate (with respect to R) when compared to the K-matrix (after having corrected the branch jumps).

Results

DR cross sections were calculated with and without rotational resolution. Cross sections from the lowest three rovibronic states of CF^+ are compared to those obtained from the lowest vibronic states without rotational resolution in Figure 4.7. The major discrepancies are most evident at the lowest energies, which is unsurprising. The rotational constant of CF^+ in its ground vibronic state is $\sim$1.7 cm^{-1} or $\sim 2.1\times10^{-4}$. Hence, the rotationless cross sections are expected to be different at lower energies. However, major features retain their shape between the two, although major

resonance positions at lower scattering energies are shifted. Above $\sim 2 \times 10^{-2}$ eV, the cross sections from both calculations become much more similar. The first vibrational threshold is at about .21 eV — not shown in Figure 4.7.

Figure 4.8 compares the $v = 0$ (no rotational frame transformation) DR rate coefficients convolved according to (4.36) to a previous theoretical calculation[107] and experimental results from the Test Storage Ring[107] (TSR). Also plotted are our calculated results including the rotational structure via the rotational frame transformation ($j = 0$). These results, along with cross sections from other initial rotational states, are averaged at several rotational temperatures to demonstrate the difference between approaches with and without rotational structure over several energy ranges. At lower energies, the difference is significant because of the low rotational energies and especially small rotational constant of CF^+. At higher energies, however, the results are all very similar. This gives one an idea of the electron energy ranges in which the rotational structure of the ion can or can not be neglected without significantly reducing the accuracy of the calculation. The average over initial states was only taken up to 150 K, despite experimental measurements being taken with ions at approximately 700 K, because our rotational basis was not large enough to confidently converge thermal averages at higher temperatures.

Low-energy DR of CH^+

Fixed-nuclei calculations

Figure 4.10 shows the lowest potential energy curves of CH^+. In interstellar clouds and storage rings, CH^+ is observed in its ground state, $X^1\Sigma^+$. The two lowest excited states, $a^3\Pi$ and $A^1\Pi$, have relatively low energies of ~ 1 – 3 eV above the ground state. One would expect the Rydberg resonances associated with such low-lying electronic states to be important to the indirect DR mechanism, hence why we include these three states in our study. The potential energy curves of CH^+ were calculated in the C_{2v} group with the MRCI method and the correlation-consistent

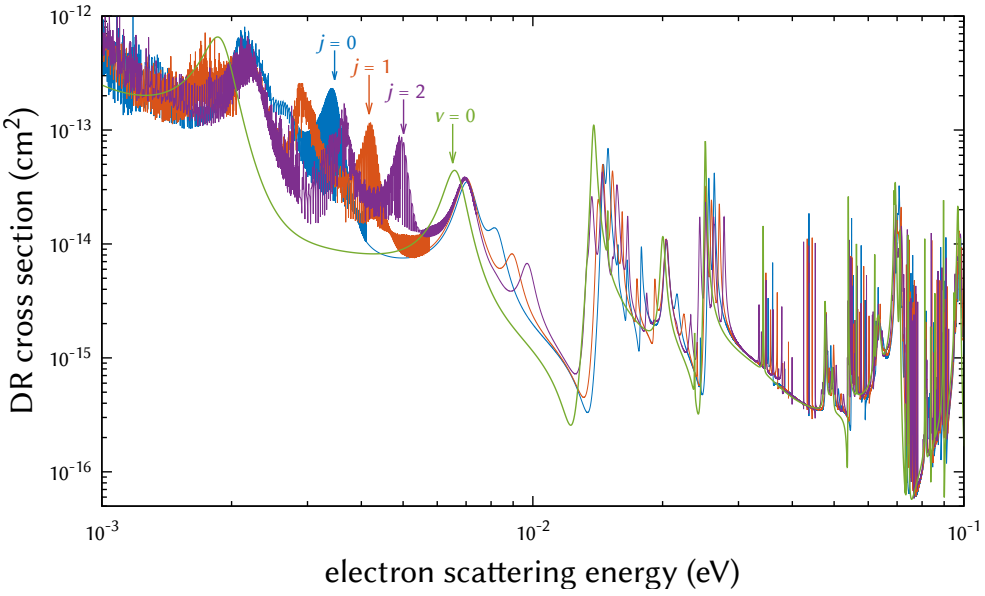

Figure 4.7: DR cross sections for CF^+ from its lowest three ($j = 0, 1, 2$) rovibronic states and from its lowest vibronic state ($v = 0$) without rotational resolution.

polarized valence quintuple-zeta (`cc-pV5Z`) basis set using the `MOLPRO` software suite[88,89].

The scattering calculations were done with the R-matrix method implemented in UKRMol[104,108,105], accessed via the Quantemol-N interface[106]. The full configuration interaction (FCI) method was used with the correlation-consistent polarized valence quadruple-zeta (`cc-pVQZ`) basis set to represent the electronic wavefunction of the ion. The $X^1\Sigma^+$, $a^3\Pi$, and $A^1\Pi$ electronic states of the ion were considered. The $1\sigma^2$ orbital was frozen; the active space was given by the 2–7σ, 1–3π, and 1δ orbitals; the 8–9σ and 4–5π virtual orbitals were used as members of the continuum set in the inner-region calculations. Calculations were performed in the C_{2v} Abelian point group for 300 evenly-spaced values of R between 1.200 and 2.695 bohr, with an R-matrix radius of $a = 13$ bohr, in the molecular CoM frame. 25 partial waves with $l = 0 - 4$ were included to represent the incident electron.

The K-matrix could be directly extracted from the R-matrix calculations at each R as in the case of CF^+. However, to include channels attached to the excited states, the K-matrices must

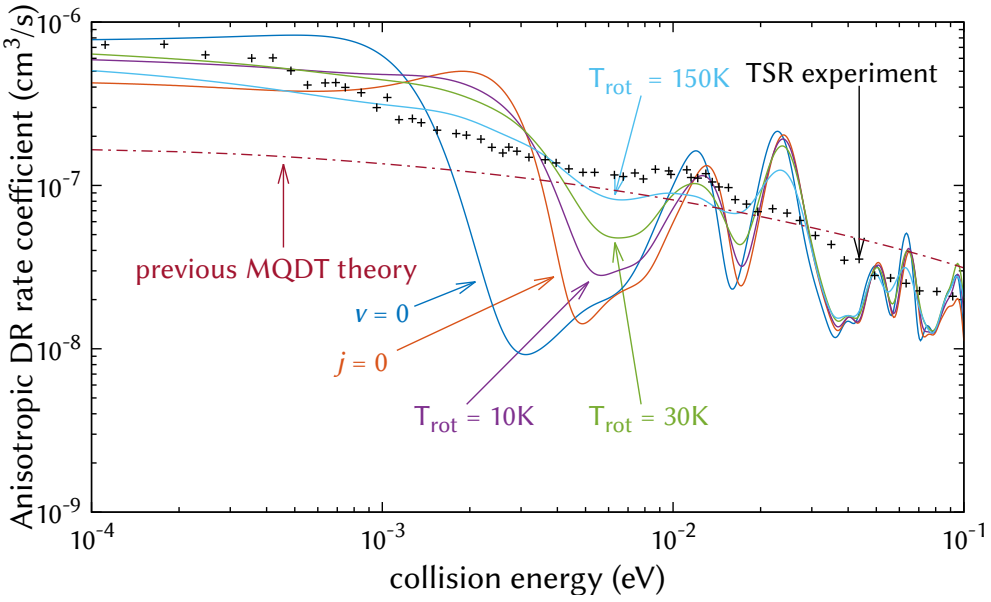

Figure 4.8: DR rate coefficients for CF^+. The present theoretical DR rate coefficients from the lowest vibronic state ($v = 0$, no rotational resolution) and rovibronic state ($j = 0$, rotational resolution) are compared to the previous MQDT treatment and experimental results from the TSR of Novotný et al. [107]. The rotationally resolved results were also averaged over several initial states at several rotational temperature of the ions (10, 30, and 150 K)

be calculated at total energies above that of the considered electronic states, i.e. $\sim 3-5$ eV above the ground electronic state of the ion, such that these channels are open. Figure 4.9 demonstrates how, above such energies, the eigenphase are smooth. The K-matrix, therefore, is not expected to have resonances as a function of energy. However, we do not expect the K-matrix to accurately reproduce low-energy ($E_{el} \lesssim 1$ eV) electron scattering.

To circumvent this issue, the energy-dependent R-matrix is extracted from the R-matrix calculations in the Wigner-Eisenbud form (2.71) at the R-matrix radius ($a = 13$ bohr) at some relatively smaller energy above the ground electronic state of the ion at each R (0.075 eV). Although the channels attached to the excited states are asymptotically closed at such energies in our considered range of R, some are treated as being open — these are considered weakly closed channels. After this identification, the channel elimination procedure (2.74) is applied to the R-matrix. The

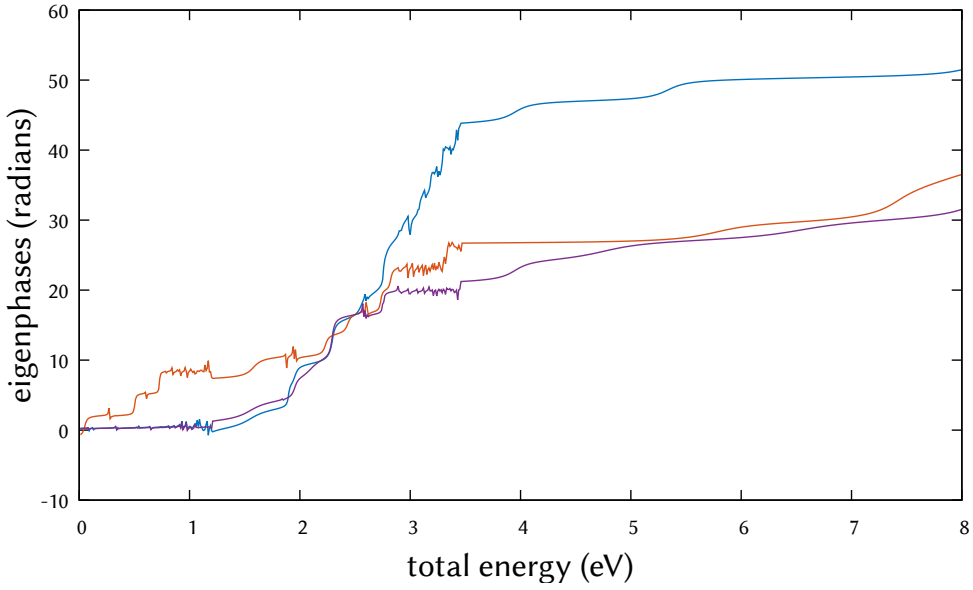

Figure 4.9: CH+ scattering eigenphases for the different irreducible representations of the C_{2v} point group at $R = 2.10$ bohr.

Table 4.2: Channel classification during the MQDT CCEP of the CH^+ R-matrix. All possible projections of l are implied for each value of l. The rightmost column gives the value of the matrix $\underline{q}$ used to normalize channel functions and used in the CCEP (4.23, 4.24).

electronic state	l	classification	q_{il}
$X^1\Sigma^+$	0 – 4	open	1
$a^3\Pi$	0 – 1	weakly closed	1
	2	weakly closed	$\sqrt{A(2E_i, 2)}$
	3 – 4	strongly closed	—
$A^3\Pi$	0 – 4	strongly closed	—

R-matrix is originally expressed in a basis of 125 channels: 25 partial waves l =0–4 attached to the ground $X^1\Sigma^+$ and the doubly degenerate $a^3\Pi$ and $A^1\Pi$ states. During the channel elimination procedure, the channels have the classification given by Table 4.2.

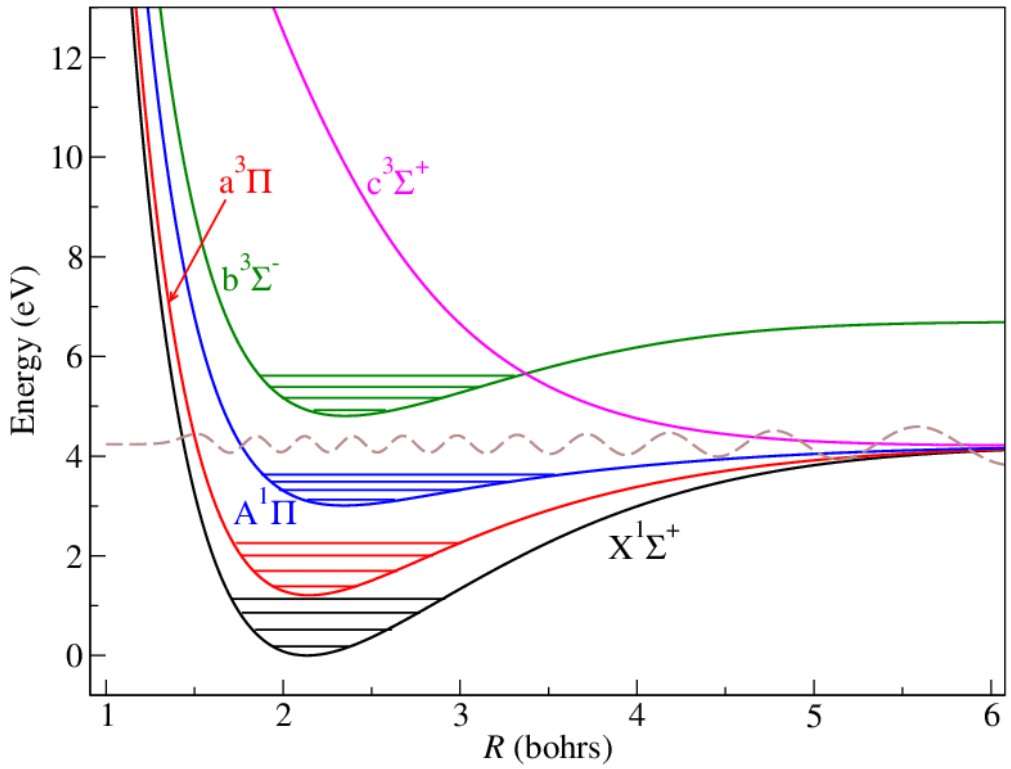

Figure 4.10: Lowest potential energy curves of CH^+ with various vibrational levels attached to each bound electronic state. The dashed line is one of the dissociative (continuum-state) wavefunctions.

The K-matrix is then obtained in the basis of open, weakly closed, and strongly closed channels from the R-matrix following their relation given in (2.72), where the R-matrix is actually the physical R-matrix after channel elimination (2.74). Such a K-matrix does not exhibit electronic Rydberg resonances from the ion's low-lying electronic states, but the is contained implicitly in the K-matrix. After closing the strongly closed channels, we are left with 27 channels $|il\lambda\rangle$. Hence, the real and symmetric electronic K-matrices belong to $\mathbb{R}^{27\times 27}$.

Results

DR cross sections from the lowest three rovibronic levels of CH^+ ($X^1\Sigma^+$ $v = 0$, $j = 0, 1, 2$) are shown in Figure 4.11. They are compared against recent experimental measurements made

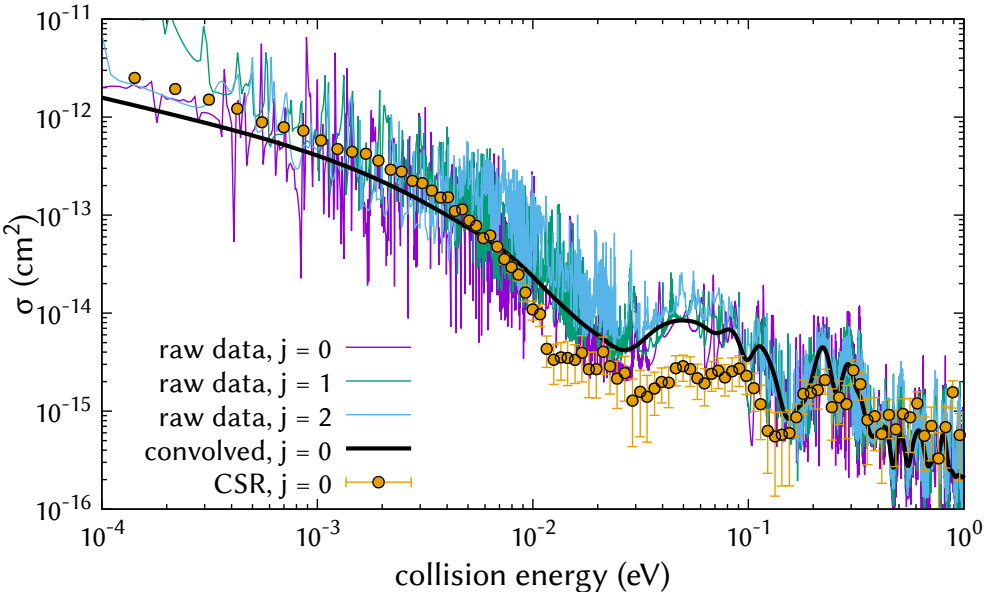

Figure 4.11: CH^+ DR cross sections as a function of collision energy for the first three rotational states within the ground vibronic channel $X^1\Sigma^+$, $v = 0$. The thin line represent raw or unconvolved theoretical cross sections from the present study ($j = 0 - 2$), the thick line is the current theoretical cross section for $j = 0$, and the circles are experimental DR measurements from the ground rovibronic state of CH^+ [39].

at the CSR by Paul et al. [39]. The abscissa in Figure 4.11 is $E_\parallel$, the same longitudinal collision energy as in (4.36). The ordinate values are the measured rate coefficients — **not** convolved or thermally averaged — divided by the electron $v_{el} = \sqrt{2E_{el}/m_e}$. The theoretical results have many resonances that are associated with energetically closed channels of the ion, but are convolved according to (4.36) to compare with the experimental CSR measurements. Energy uncertainties of $\gamma_\parallel = 0.27$ meV and $\gamma_\perp = 2.0$ eV [39] were used.

Figure 4.12 shows the same quantity as Figure 4.11 multiplied by the collision energy E_{el}. This eases the aggressive log scaling of the cross sections and makes it easier to compare results with more detail. The CSR experimental data [39], a previous room-temperature storage-ring experiment [101], and a single-pass merged-beam experiment [109] have their results displayed as points and compared against previous theoretical results [54,57,35,110] and the current convolved theoretical

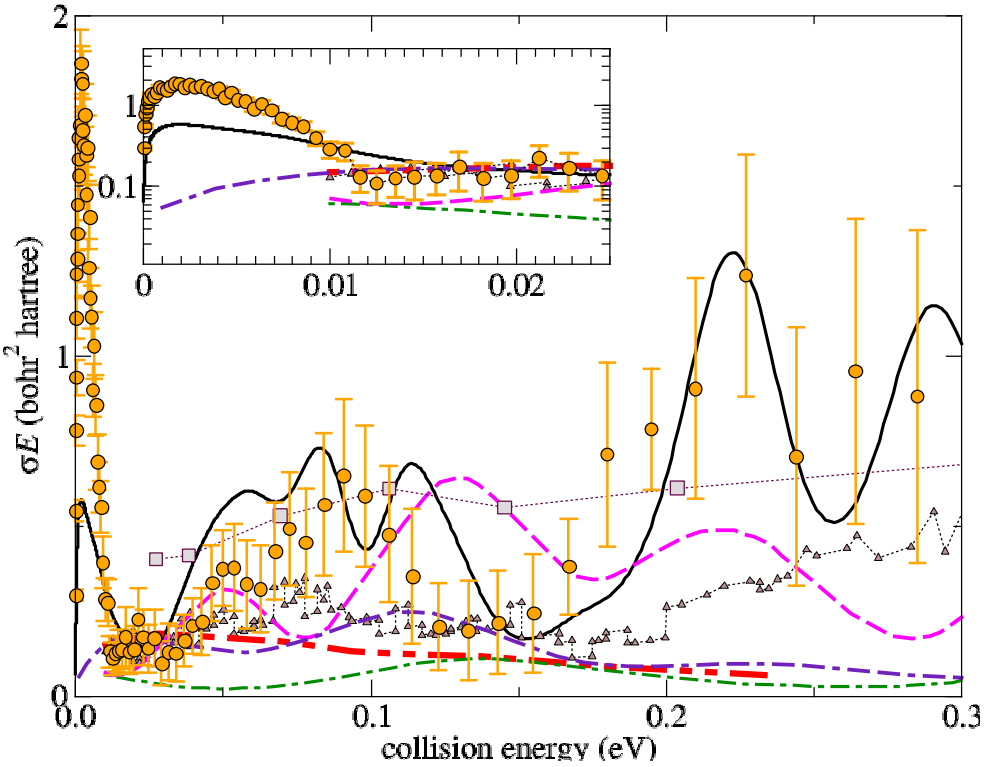

Figure 4.12: CH^+ DR cross sections multiplied by collision energy $E_{el} \cdot \sigma_i(E_{el})$ as a function of collision energy. The present theoretical DR cross section from the ground rovibronic state of CH^+, convolved according to (4.36) with $\gamma_{\|} = 0.27$ meV and $\gamma_{\perp} = 2.0$ meV. Experimental DR measurements are represented by circles[39], triangles[101], and squares[109]. Previous theoretical results are given by the dot-dashed[54], dashed[57], double-dot-dashed[35], and dot-double-dashed[110] lines.

results. The storage-ring and merged-beam experiments could not resolve DR cross sections to the ground rovibronic level of CH^+. The ions were likely had a significant population of rotationally[101] or even rovibrationally[109] levels. The storage-ring results agree well at low energies, although the merged-beam results are larger, possibly due to the vibrationally excited ions. At energies approaching 0.01 eV from above, the theoretical results of Takagi et al.[35] (rovibrational) and Mezei et al.[110] (vibrational) agree the best with the experimental CSR[39] data. However, the results of Mezei et al.[110] significantly underestimate the experimental data under 0.01 eV, possibly due to the omission of the rotational structure.

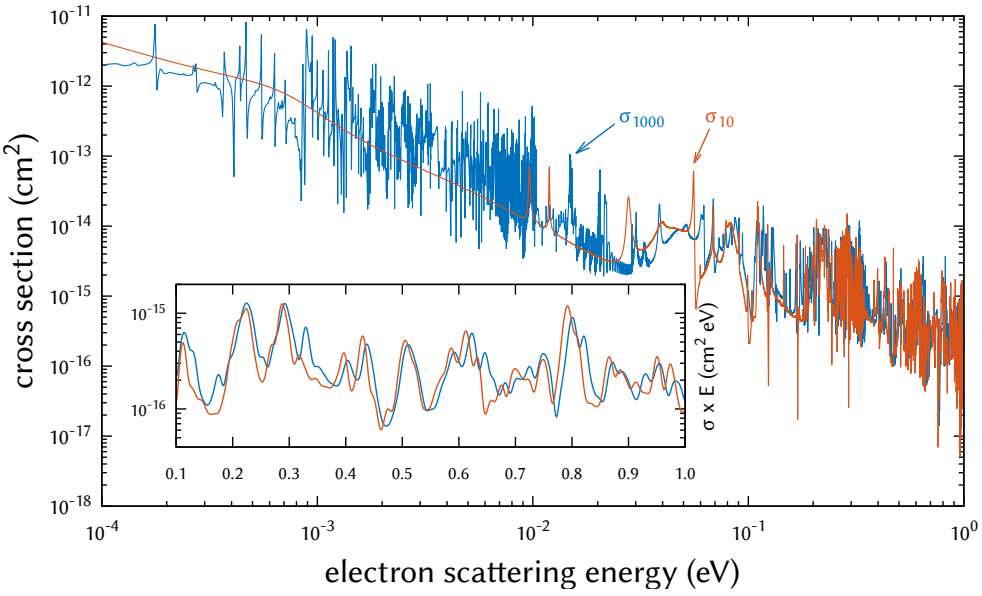

Figure 4.13: DR cross sections from the ground vibronic state of CH^+. Results from the calculation without rotational resolution, obtained according to (4.30) are labelled as σ_{10}. Results from the calculation with rotational resolution, obtained according to (4.30) from the ground rovibronic state of CH^+, are labelled as σ_{1000}. The inset compares the same results from each calculation, multiplied by the electron scattering energy E_{el} and convolved with a Gaussian distribution (4.32) with a width of $\gamma = 5$ meV.

Figure 4.13 compares DR cross sections with and without rotational resolution. There is, unsurprisingly, a lack of resonant structure at lower collision energies in the vibronic calculation. The first few resonance in the vibronic data seem to be shifted when compared to the rovibronic results. At larger energies, however, the overall structure of the vibronic and rovibronic data are similar. The discrepancies are on the order of magnitude of the rotational constant of CH^+, which was calculated to be 13.76 cm^{-1} ($\sim$1.7 meV) in its ground vibronic state.

Figure 4.14 shows the kinetic state-selected rate coefficients from the theoretical results of Mezei et al.[110], the experimental measurements at the CSR[39], and the current calculations convolved according to (4.34). Our convolved theoretical cross section and kinetic rate coefficients agrees with the experimental results well at most energies, especially when compared to previous

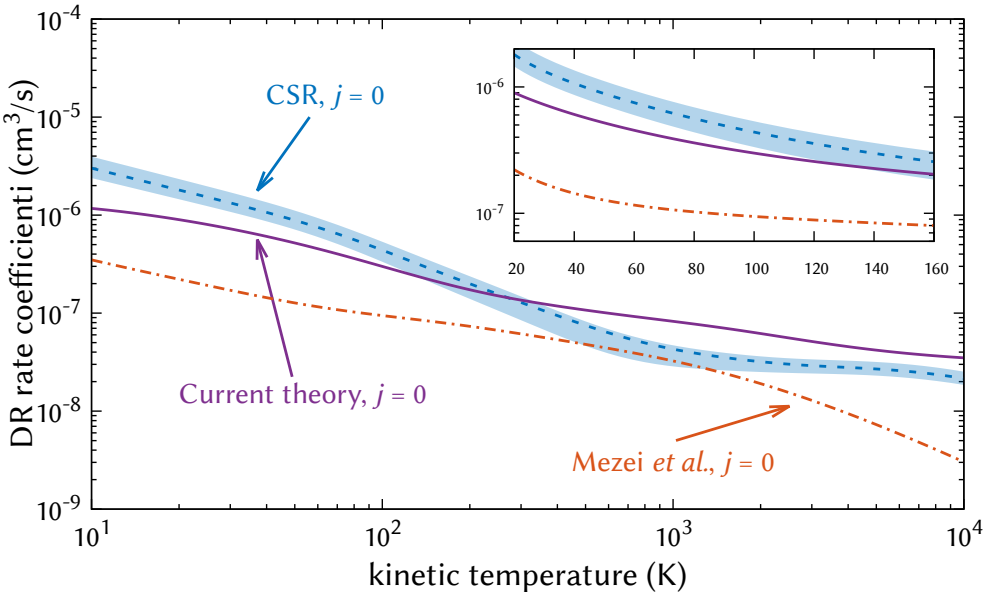

Figure 4.14: Kinetic state-selected CH^+ DR rate coefficients from the ground rotational state of the ion. The dashed curve with a filled error curve are from the recent experimental measurements made at the CSR[39], the dot-dashed curve is from previous theoretical calculations that do not resolve vibration[110], and the solid line represents the present theoretical results thermally averaged according to (4.34, 4.35).

theoretical results. At kinetic temperatures below ∼400 K, our kinetic rate coefficients are closer to those of the experimental CSR measurements[39].

Figure 4.15 shows convolved DR cross sections from the lowest rotational states of CH^+ where the K-matrices were evaluated at different energies above the ground electronic state of CH^+. For reference, the CSR results are also plotted. The largest difference is at low energies, where the energy dependence is not obvious. The lowest and highest evaluation energies agree very well, while intermediate energies fall anywhere between these two and the experimental results. Surprisingly, the highest evaluation energy resulted in the best agreement with the experiment around 1×10^{-2} eV. This suggests there may still be improvements to be made in the method. Above, $\sim 5 \times 10^{-2}$ eV, the difference is small. This does not necessarily mean that the evaluation energy of the K-matrix plays less of a role. Instead, some channels that were considered strongly

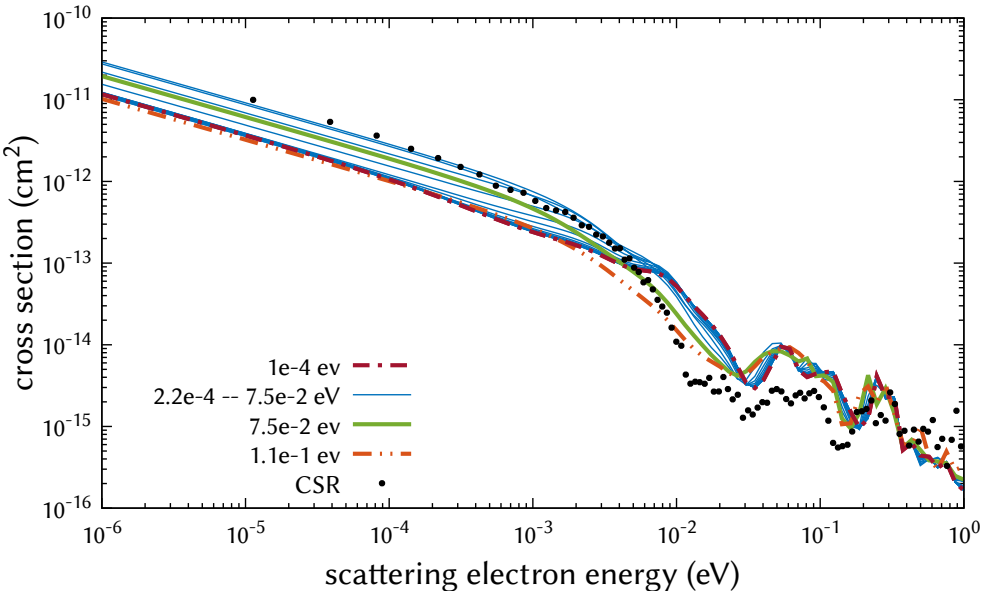

Figure 4.15: Convolved CH^+ DR cross sections (solid lines) compared with experimental DR cross sections measured at the CSR[39]. The convolved cross sections were calculated with S-matrices evaluated at various energies (given in the legend) above the ground electronic state of the CH^+.

closed for these evaluation energies could be considered weakly closed.

Rovibronic excitation of CH^+

The present method can also be used calculate rovibronic (de-)excitation cross sections and rate coefficients. All elements of the approach described above are the same, except the differences described in this section. One major difference is that there is no CAP (4.11); dissociative flux is not being considered in this approach. The vibrational Hamiltonian is Hermitian, so we only need one S-matrix for the calculations. Unitarity of the S-matrix is again defined by the usual spectral norm, i.e. $S^J S^{J\dagger} = I$ or $S^\Lambda S^{\Lambda\dagger} = I$. Only vibrational levels with energy levels below that of the dissociation threshold for the attached electronic state are calculated, and vibrational eigenenergies (channel energies) are real.

The vibronic S-matrix is calculated in the same manner as (4.14). The remaining treatments

to this matrix (4.16, 4.23) are identical, keeping in mind that the matrix $\underline{\beta}(E_{tot})$ (4.22) is real and that only one S-matrix needs to be calculated, instead of two. The cross sections, however, take a slightly different form. Once the physical S-matrix has been obtained, (de-)excitation cross section are obtained from it following

$$\sigma_{n'v'\leftarrow nv}(E_{el}) = \frac{\pi}{2m_e E_{el}} \sum_{ll'} \sum_{\lambda\lambda'} \left| S^{\Lambda,phys}_{n'v'l'\lambda',nvl\lambda} \right|^2 \tag{4.37}$$

without rotational resolution, or by

$$\sigma_{n'v'j'\mu'\leftarrow nvj\mu}(E_{el}) = \frac{\pi}{2m_e E_{el}} \sum_{J} \frac{2J+1}{2j+1} \sum_{ll'} \left| S^{J,phys}_{n'v'j'\mu'l',nvj\mu l} \right|^2 \tag{4.38}$$

with rotational resolution. It should be noted that (4.37, 4.38) apply only to inelastic cross sections. Kinetic state-selected or averaged rate coefficients for (4.37, 4.38) can be obtained following (4.35, 4.34).

The Coulomb-Born approximation

Although DR is driven by short-range processes, rotational excitation is governed by more long-range interactions. The target molecule's permanent dipole moment drives the $\Delta j = \pm 1$ transitions and couples partial waves differing in l by 1. The partial wave expansion, especially when not performed in the molecular CoC, converges more slowly as progressively higher (larger l) partial waves are coupled to each other; the R-matrix calculations only include up to $l = 4$ partial waves. One method of circumventing this issue, implemented in our approach, is to calculate the total and partial contributions of the dipole moment to the excitation cross sections within the Coulomb-Born (CB) approximation[111–113], i.e., the dipole interaction is treated as a perturbation to the Coulomb interaction.

This CB approximation is less valid for low partial-waves scattering, especially s-waves

where the scattering electron is close to the target and the $1/r^2$ dipole potential cannot be considered a perturbation. Therefore, we replace the $l = 0$–2 CB cross sections with our $l = 0$–2 cross sections calculated with the above-mentioned R-matrix method. In a similar method to that of Rabadán and Tennyson [114], the total CB rotational excitation cross sections (σ^{TCB}) and partial CB rotational excitation cross sections ($\sigma^{PCB}_{l=0-2}$) for the partial waves used in our approach are calculated. Then, the contribution of higher partial waves not included in our approach can be accounted for following

$$\sigma^{\text{RVE}} = \sigma^{\text{R-mat}} + \sigma^{\text{TCB}} - \sigma^{\text{PCB}}, \tag{4.39}$$

where $\sigma^{\text{R-mat}}$ is the present rovibronic excitation cross section obtained with out method starting from R-matrix calculations.

The partial CB cross sections are given by

$$\begin{aligned}\sigma^{\text{PCB}}_{j'v'\leftarrow jv} = 16\pi\frac{k'}{k}\left|\langle v'|Q_\xi(R)|v\rangle\right|^2 \frac{2j'+1}{2\xi+1}\begin{pmatrix} j & j' & \xi \\ 0 & 0 & 0\end{pmatrix}^2 \\ \times (2j+1)(2j'+1)\sum_{ll'}^{l_{\text{max}}}\begin{pmatrix} l & l' & \xi \\ 0 & 0 & 0\end{pmatrix}^2 \left|M^\xi_{ll'}\right|^2,\end{aligned} \tag{4.40}$$

where $l_{\text{max}} = 2$ because our R-matrix calculations only include up to $l = 2$ partial waves. The dipole moment function is given by $Q_\xi(R)$ and the matrix elements $M^\xi_{ll'}$ are given by

$$M^\xi_{ll'} = \frac{1}{kk'}\int_0^\infty dr F_l(\eta, r) r^{-\xi-1} F_{l'}(\eta', r), \tag{4.41}$$

where $F_l(\eta, r)$ is the regular radial Coulomb function, $\eta = -1/k$, and $\eta' = -1/k'$. For an approach that does not treat vibration, the integral $\langle v'|Q_\xi(R)|v\rangle$ in (4.40) can be replaced with the dipole moment at the equilibrium geometry of the ion. Considering the dipolar coupling ($\xi = 1$),

the partial CB cross sections (4.40) converge to the following as $l_{\max} \to \infty$:

$$\sigma^{\text{TCB}}_{j'v' \leftarrow jv} = \frac{8}{3}\frac{\pi^3}{k^2} \left|\langle v'|Q_\xi(R)|v\rangle\right|^2 (2j'+1) \begin{pmatrix} j & j' & 1 \\ 0 & 0 & 0 \end{pmatrix}^2 f(\eta, \eta'), \tag{4.42}$$

where

$$\begin{gathered} f(\eta, \eta') = \frac{e^{2\pi\eta}}{(e^{2\pi\eta}-1)(e^{2\pi\eta'}-1)} \chi_0 \frac{d}{d\chi_0} \left|{}_2F_1(-i\eta, -i\eta'; 1; \chi_0)\right|^2, \\ \zeta = \eta' - \eta, \quad \chi_0 = -4\eta\eta'/\zeta^2. \end{gathered} \tag{4.43}$$

The function ${}_2F_1(a, b; c; z)$ is the Gaussian hypergeometric function, defined as:

$${}_2F_1(a, b; c; z) = \sum_{n=0}^{\infty} \frac{(a)_n (b)_n}{(c)_n}, \quad (q)_n = \frac{\Gamma(q+n)}{\Gamma(q)}. \tag{4.44}$$

It should be noted that we only include the CB correction to $\Delta j = \pm 1$ transitions; our $\Delta j = \pm 2$ transitions are obtained purely from our R-matrix method. For further detail in computing (4.43), we invite the reader to read the work of Chu and Dalgarno [113]. Additionally, the work of Rabadán and Tennyson [114] contains minor errors (non-squared Wigner 3-j symbols) in their equations (3) and (4), which are corrected here.

Results

The vibrational excitation state-selected kinetic rate coefficients without rotational resolution, calculated and convolved according to (4.36,4.37), are compared with those of Jiang et al. [115], as shown in Figure 4.16. The left panel compares vibrational excitation rate coefficients within the ground electronic state, which agree well for the plotted transitions ($v = 0 \to v' = 1, 2, 3$). The right panel compares vibronic excitation rate coefficients from the ground vibronic states to the lowest 4 vibrational levels of the fist excited state ($a^3\Pi$). These rate coefficients agree less than those within the ground electronic state. Such differences may be due to the improvements in the

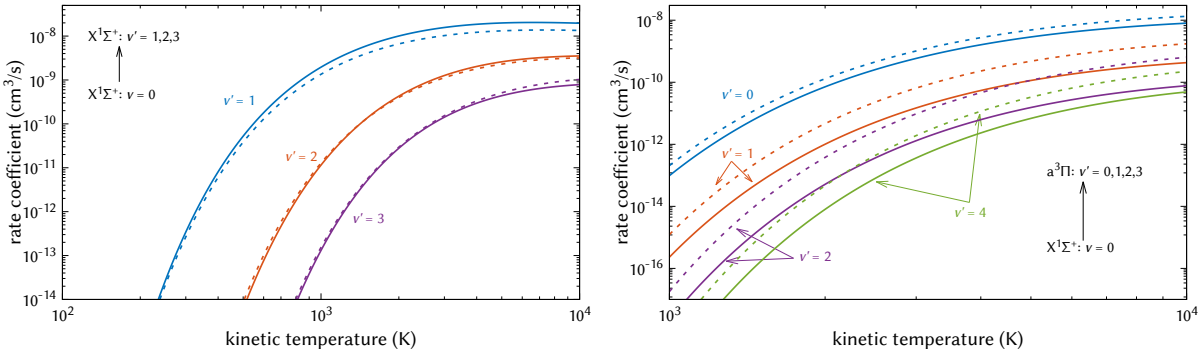

Figure 4.16: State-selected kinetic VE rate coefficients within the ground electronic state of CH^+ (left) and from the ground electronic state to the first excited state of CH^+ (right). Solid lines represent rate coefficients from the present calculations, while dashed lines are taken from a previous calculation [115]. The present cross sections are obtained according to 4.37, corresponding rate coefficients are obtained following (4.34).

present treatment, e.g., using the δ-matrix in a basis of complex spherical harmonics or evaluating K-matrices at much lower energies while considering weakly closed channels.

Rotational excitation cross sections were calculated according to (4.38). These were convolved according to (4.32) to demonstrate the effect of convolution on raw data and convolved according to 4.36 to produce state-selected kinetic rate coefficients. The results of both convolutions are shown in Figure 4.17. The cross sections in the left panel, convolved according to (4.32), show the dominance of the dipole-driven $\Delta j = 1$ transition, which is reflected in the state-selected thermally averaged results in the right panel. The right panel of Figure. 4.17 also compares the present rotational excitation rate coefficients with those obtained by Hamilton et al. [116], who included the CB correction for $\Delta j = \pm 1, \pm 2$ transitions. We only include this correction for $\Delta j = \pm 1$ transitions, but the agreement between the results is good overall. Hamilton et al. [116] also use an R-matrix approach, but use the adiabatic-nuclei-rotation approximation to obtain rotational excitation (RE) cross sections and rate coefficients, while we use a frame transformation (2.81) to describe the rotational structure of the ion.

Figure. 4.18 illustrates the difference between the state-selected RE data with and without

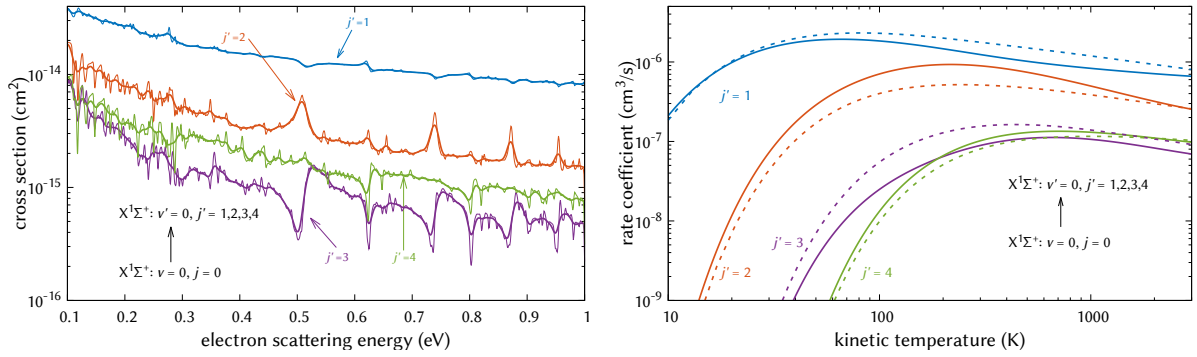

Figure 4.17: Rotational excitation cross sections within the ground vibronic state of CH^+, starting from $j = 0$, obtained according to (4.38) (left). State-selected kinetic RE rate coefficients (right) obtained from the cross sections in the left panel following (4.34) The cross sections are obtained according to (4.32) with $\gamma = 1$ meV (thin lines) and $\gamma = 5$ meV (thick lines). In the right panel, solid lines represent the present theory, while dashed lines represent the results of Hamilton et al. [116].

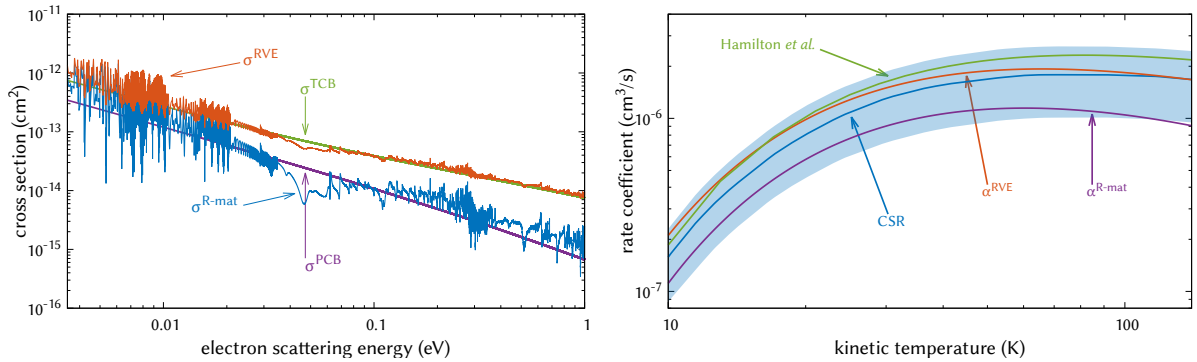

Figure 4.18: Left panel: comparison of cross sections for rotational excitation $j = 0 \to j' = 1$ obtained using the R-matrix approach with s, p, and d partial waves ($\sigma^{\text{R-mat}}$), the closed-form total CB approximation (σ^{TCB}), the partial CB cross section obtained with s, p, and d partial waves (σ^{PCB}), and the cross section where the R-matrix data is combined with the total CB cross section accounting for partial wave with $l > 2$ (σ^{RVE}). Right panel: state-selected kinetic RE rate coefficients from $j = 0$ to $j' = 1$ within the ground vibronic state of CH^+. The measured rates coefficients from the CSR [117] are compared to the results of Hamilton et al. [116] and our kinetic rate coefficients with (α^{RVE}) and without ($\alpha^{\text{R-mat}}$) the CB correction.

the CB approximation for the $\Delta j = 1$ transition. The left panel shows the four cross sections from (4.39). The right panel compares state-selected rate-coefficients from the present work with (α^{RVE}) and without ($\alpha^{\text{R-mat}}$) the CB-approximation to theoretical results from the work of Hamilton et al. [116] and recent experimental results from the work of Kálosi et al. [117] at the CSR. Our present results with the CB correction show the best overall agreement with the CSR measurements, although all theoretical rates are within the provided uncertainty for most of the kinetic temperatures shown (10–140 K).

The work detailed in this chapter on DR has been published:

- Joshua Forer, Dávid Hvizdoš, Xianwu Jiang, Mehdi Ayouz, Chris H Greene, and Viatcheslav Kokoouline. Unified treatment of resonant and nonresonant mechanisms in dissociative recombination: Benchmark study of CH^+. *Physical Review A*, 107(4):042801, 2023

A manuscript covering the RVE portion of this chapter has been submitted to the Monthly Notices of the Royal Astronomical Society and is available at `https://arxiv.org/abs/2309.14370`:

- Joshua Forer, Dávid Hvizdoš, Mehdi Ayouz, Chris H Greene, and Viatcheslav Kokoouline. Kinetic rate coefficients for electron-driven collisions with CH^+: dissociative recombination and rovibronic excitation. *arXiv preprint arXiv:2309.14370*, 2023

CHAPTER 5: CONCLUSIONS

REA to C_3N via dipole-bound states

DBS energies of rotating C_3N^- were calculated and used in our theoretical approach. Six such weakly bound states were found to exist within the V_{ai} potential. REA cross sections, starting from these six DBSs, were obtained for several rotational states of C_3N over a large interval of collision energies, including low, astrochemically relevant energies. The present theoretical REA cross sections are much smaller than those previously calculated by Khamesian et al.[22], which was expected, who concluded that their calculated REA cross section is too small to explain the observed abundance of C_3N^- in the ISM, assuming the species is formed by REA.

The observed C_3N^- abundance in the ISM has been determined to be too large to be explained by the theoretically REA cross sections of Khamesian et al.[22]. We, therefore, draw the same conclusion given our smaller REA cross sections. Vibration was not considered in the present approach. The effect of long-lived vibrational bending resonances could be considered in future studies. Alternative formation mechanisms, such as collisions between carbon anions and atomic nitrogen, should be considered for C_3N^- and possible other similar anions, although they deserve separate studies. A technical result of interest to theorists: the short-range part of the interaction potential significantly influences the REA cross sections below a few eV. The present approach could be applied to study weakly-bound states and electron scattering for systems with a dominant quadrupole interaction at large distances, such as $TCNB^-$ [120].

DR of CH^+ and CF^+

The theoretical approach presented here can simultaneously treat the direct and indirect DR mechanisms. Previous studies in the case of CH^+ [35,110] have accounted for both mechanisms, but the present method is easier to implement in the sense that it does not require bound dissociative states

of the neutral molecule and their associated couplings to be calculated. A similar approach was used to study DR of HeH^+ [121]. The theory can be applied to molecular ions regardless of whether they have low-lying electronic resonances, including open-shell ions, of which DR is challenging to study with previous theoretical methods. The present DR cross sections for CH^+ agree well overall with recent experimental results at the CSR [39], where experimental DR measurements were resolved to the ground rovibronic state of the ion. The overall magnitude of the cross sections and positions of major resonances are well reproduced. An important limitation of the present method is the use of an energy-independent scattering matrix. Accounting for such an energy dependence in the case of HeH^+ DR improved the agreement with experimental results [41].

There is no recent rotationally resolved experimental data against which to compare our rovibronically-resolved DR cross sections for CF^+. However, upon calculating vibronically resolved cross sections — bypassing the rotational frame transformation (2.81) — we obtain overall good agreement with experimental results obtained at the TSR [107]. The treatment used to describe the DR of CF^+ is slightly older, akin to that of [58]; applying the method used with CH^+ may yield more accurate low-energy DR cross sections. Further improvements can be made in the identification of eigenphases across geometries so that the δ-matrix can be properly interpolated with a larger initial number of calculations spanning a wider range of internuclear distances.

RVE of CH^+

In addition to DR, this approach can be used to study electronic, vibrational, or rotational (de-)excitation of diatomic ions, which may be difficult to measure experimentally. Vibrational excitation state-selected kinetic rate coefficients of CH^+ are compared to previous results [115]; we find excellent agreement with vibrational excitation rate coefficients within the first excited state, but differences arise when we consider vibronic excitation to vibrational levels of the first excited electronic state. This difference could be explained by this study's improved treatment of the electronic matrices obtained from the R-matrix scattering calculations, as well as other issues that have been

addressed in the present implementation. The present RE rate coefficients within the ground electronic state of CH^+ are compared to the work of Hamilton et al.[116], which is an R-matrix method that describes RE with the adiabatic-nuclei-rotation approximation and does not treat vibration. They correct their $\Delta j = \pm 1, \pm 2$ transitions with the CB approximation, while we only do so for $\Delta j = \pm 1$ transitions. Results between our approaches agree well over the presented kinetic temperatures. Compared to $j = 0 \rightarrow j' = 1$ rate coefficients recently measured at the CSR[117], our theoretical results using the CB correction agree better over all plotted kinetic temperatures than our theoretical results without the CB correction, and slightly better than the recent theoretically determined rate coefficients of Hamilton et al.[116] over most kinetic temperatures between 10 K and 140 K. However, all theoretically determined rates under 100 K are within the experimental uncertainty.

APPENDIX A: SYMMETRY — POINT GROUPS

Point groups

The *group* is an important mathematical construct used to describe the symmetry of molecules — their electronic wavefunctions, the spatial orientation of their nuclei, their vibration, etc. A group is a nonempty set (G) equipped with some binary operator ($*$) that, when applied to two elements of the set, produced an element of the same set. Such a group, denoted $(G, *)$, satisfies three properties:

associativity:	$(a * b) * c = a * (b * c) \quad \forall a, b, c \in G$
the identity element:	$\exists e \in G$ such that $\forall a \in G$, $e * a = a * e = a$
the inverse element:	$\forall a \in G$, $\exists b \in G$ such that $a * b = b * a = e$.

Any group G satisfying commutativity ($a * b = b * a \ \forall a, b \in G$) is said to be *Abelian*. The set of all real numbers ($\mathcal{R}$), for example, form a group with respect to addition: ($\mathcal{R}$,+). The identity element — always its own inverse — is 0, and the negative numbers are the additive inverses of the positive numbers (and vice versa).

The elements of symmetry groups in the context of scattering theory represent transformations that do not affect the Hamiltonian of a system. The *point group* is type of group whose elements, when applied to some body, have a common fixed point that is left unchanged by the elements. All symmetry axes and planes must all intersect at at least one point.

Two point groups are mentioned explicitly in this manuscript the infinite group $C_{\infty v}$ and one of its finite Abelian subgroups, C_{2v}. Their character tables are given below. The group $C_{\infty v}$ is a linear group with a symmetry axis, about which symmetry-respecting rotations are performed, and a plane of reflection that contains the symmetry axis, about which symmetry-respecting reflections are performed. It is an infinite group, i.e. it contains an infinite amount of elements. There are two non-identity classes of symmetry operations: a rotation about the symmetry axis by some integer multiple of an angle θ ($C(\theta)$), and a reflection about some symmetry plane passing through the symmetry axis σ_v. The former class has two elements per integer multiple of θ — a clockwise

and a counterclockwise rotation. The latter contains an infinite number of elements; there are an infinity number of planes containing the axis of symmetry about which a symmetry-preserving reflection may be performed. The point group C_{2v} contains 3 non-identity elements: a rotation about the symmetry axis by 90° (C_2), and reflections about the two mutually orthogonal planes both containing the symmetry axis (σ_v and σ_v').

A *representation* of a point group describes how symmetry operations affect elements of the system. Representations that cannot be formed by a linear combination of other representations are said to be *irreducible*. Irreducible representations (irreps) have a *character* under the various symmetry operations of a point group. Representations are *group homomorphisms*; they preserve the structure of the group. A group homomorphism, given two groups $(A, *)$ and $(B, \star)$, is a function $\rho : A \to B$ obeying

$$\rho(a_1 * a_2) = \rho(a_1) \star \rho(a_2) \qquad \forall a_1, a_2 \in A. \tag{A.1}$$

The characters of irreps contain important information about the point group. For example, the electronic wavefunction of a molecule belonging to the A_2 irrep would have its sign changed only under a reflection and not under a rotation (see Table A.2). This can be seen by the A_2 irrep having character -1 with respect to the reflection operations σ_v and σ_v'.

Table A.3 is useful for determining the symmetry of the product of irreps. Considering an electron-molecule system whose wavefunction is described by the product of the target's wavefunction and the incident electron's wavefunction, the total wavefunction belongs to the irrep given by the product of the irreps of the target and electron wavefunctions.

Table A.1: Character table of the $C_{\infty v}$ point group.

$C_{\infty v}$	E	$2C(\theta)$	$\infty\sigma_v$
$A_1(\Sigma^+)$	1	1	1
$A_2(\Sigma^-)$	1	1	-1
E_1 (Π)	2	$2\cos(\theta)$	0
E_2 (Δ)	2	$2\cos(2\theta)$	0
$\vdots$	$\vdots$	$\vdots$	$\vdots$
E_n	2	$2\cos(n\theta)$	0

Table A.2: Character table of the C_{2v} point group.

C_{2v}	E	C_2	σ_v	σ_v'
A_1	1	1	1	1
A_2	1	1	-1	-1
B_1	-1	1	1	-1
B_2	-1	1	-1	1

Table A.3: Multiplication table of the C_{2v} point group.

C_{2v}	A_1	A_2	B_1	B_2
A_1	A_1	A_2	B_1	B_2
A_2	A_2	A_1	B_2	B_1
B_1	B_1	B_2	A_1	A_2
B_2	B_2	B_1	A_2	A_1

APPENDIX B: MATHEMATICAL FUNCTIONS

The Gamma function

The gamma function, $\Gamma(z)$, is defined as

$$\Gamma(z) = \int_0^\infty t^{z-1} e^{-t} dt, \quad Re(z) > 0. \tag{B.1}$$

When $z \in \mathbb{Z}_+$, the gamma function reduces to a factorial

$$\Gamma(z) = (z-1)!, \tag{B.2}$$

where, of course, $0! \equiv 1$. The gamma function is undefined only for non-positive integers.

Bessel functions

The Bessel differential equation,

$$r^2 \frac{du^2}{dr^2} + \frac{du}{dr} + \left(r^2 - l^2\right) u = 0, \tag{B.3}$$

for some $l \in \mathbb{C}$, yields two linearly independent solutions: the Bessel function of the first kind $(J_l(r))$ and the Bessel function of the second kind $(N_l(r))$, the latter of which are also known as the Neumann functions. They are given by:

$$\begin{aligned} J_l(r) &= \sum_{k=0}^{\infty} \frac{(-1)^n}{n!\Gamma(n+l+1)} \left(\frac{r}{2}\right)^{2n+l} \\ N_l(r) &= \frac{J_l(r)\cos(l\pi) - J_{-l}(r)}{\sin(l\pi)}, \quad l \in \mathbb{C} \setminus \mathbb{Z} \\ N_n(r) &= \lim_{l \to n} N_l(r), \quad n \in \mathbb{Z}. \end{aligned} \tag{B.4}$$

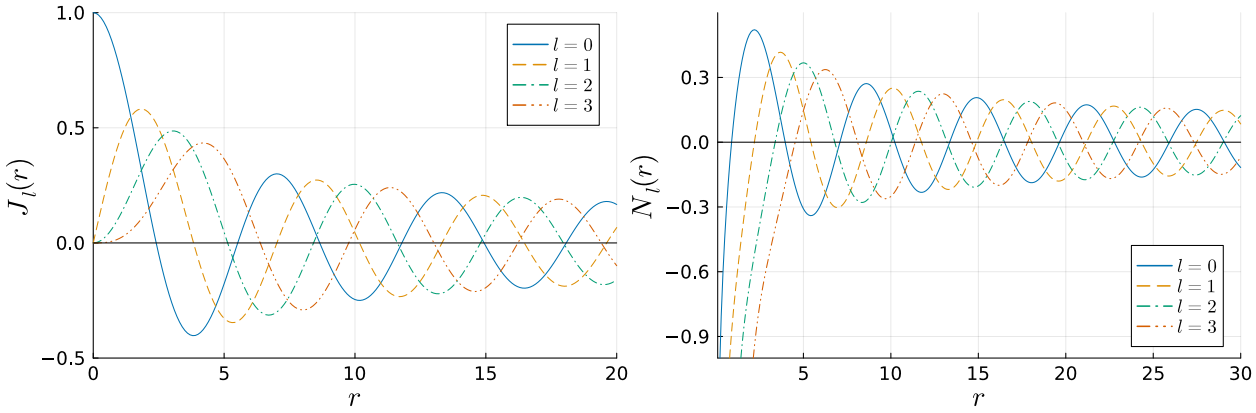

Figure B.1: Bessel functions of the first (left) and second (right) kind.

Whereas $J_l(r)$ remains finite at $r = 0$, $N_l(r)$ diverges as $r \to 0$. The functions $J_l(r) \pm iN_l(r)$ form another set of linearly independent solutions to (B.3).

Spherical Bessel functions

The spherical Bessel functions of the first kind $(j_l(r))$ and the spherical Neumann functions $(n_l(r))$, also known as the spherical Bessel functions of the second kind, solve the spherical Helmholtz equation

$$r^2 \frac{d^2u}{dr^2} + 2r\frac{du}{dr} + \left(x^2 - l(l+1)\right) u = 0. \tag{B.5}$$

and can be defined with the Bessel functions (B.4)

$$\begin{aligned} j_l(r) &= \sqrt{\frac{\pi}{2r}} J_{l+\frac{1}{2}}(r) = (-r)^l \left(\frac{1}{r}\frac{d}{dr}\right)^l \frac{\sin(r)}{r} \xrightarrow{r\to\infty} \frac{1}{r}\sin\left(r - \frac{l\pi}{2}\right) \\ n_l(r) &= \sqrt{\frac{\pi}{2r}} N_{l+\frac{1}{2}}(r) = -(-r)^l \left(\frac{1}{r}\frac{d}{dr}\right)^l \frac{\cos(r)}{r} \xrightarrow{r\to\infty} \frac{-1}{r} cos\left(r - \frac{l\pi}{2}\right). \end{aligned} \tag{B.6}$$

As $r \to 0$, $j_l(r)$ remains finite, but $n_l(r)$ diverges. Their sums $j_l(r) \pm in_l(r)$ also form a set of linearly independent solutions to (B.6).

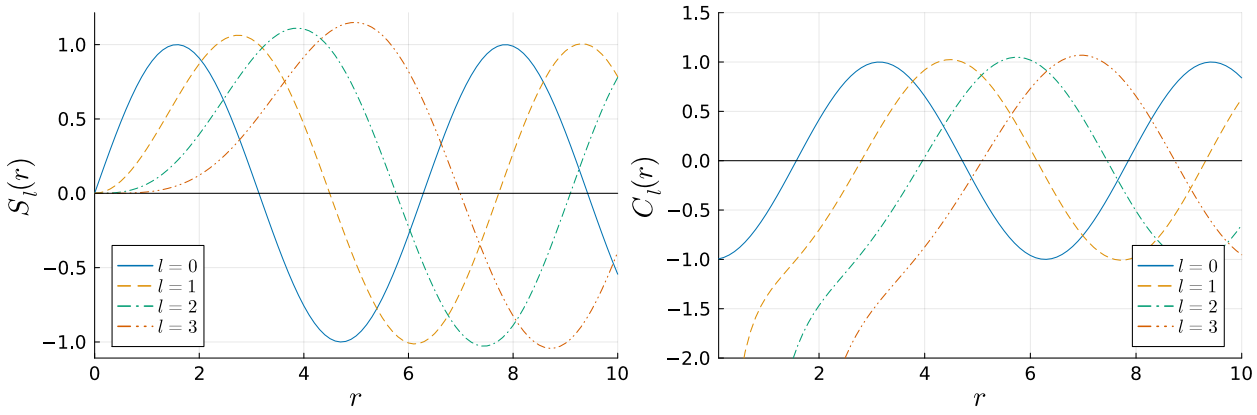

Figure B.2: Riccati-Bessel functions of the first (left) and second (right) kind.

Riccati-Bessel functions

The Riccati-Bessel functions solve the differential equation

$$r^2 \frac{d^2u}{dr^2} + \left(r^2 - l(l+1)\right) u = 0. \tag{B.7}$$

They are only different from the spherical Bessel functions by a multiplicative $\pm r$:

$$\begin{aligned} S_l(r) = r j_l(r) &\xrightarrow{r\to\infty} \sin\left(r - \frac{l\pi}{2}\right) \\ C_l(r) = -r n_l(r) &\xrightarrow{r\to\infty} cos\left(r - \frac{l\pi}{2}\right) \end{aligned} \tag{B.8}$$

As with the other spherical Bessel functions, $j_l(r) \pm i n_l(r)$ form another set of linearly independent solutions to (B.8).

Legendre polynomials

Two special cases of the Legendre differential equation,

$$(1-x^2)\frac{d^2y}{dx^2} - 2x\frac{dy}{dx} = \left(\frac{m^2}{1-x^2} - n(n+1)\right)y, \tag{B.9}$$

are of interest to us. The fist case of (B.9) is when $m = 0$ and the degree is an integer, i.e. $n \in \mathbb{Z}$. The solutions to this special case are the Legendre polynomials, often used to expand potentials behaving as $\left|\vec{r} - \vec{r}'\right|^{-1}$, for which many representations exist, e.g.

$$P_n(x) = \frac{1}{2^n n!}\frac{d^n}{dx^n}(x^2-1) = 2^n \sum_{k=0}^{n} x^k \binom{n}{k}\binom{\frac{n+k-1}{2}}{n}. \tag{B.10}$$

The $P_n(x)$ are defined for real numbers x in the interval $x \in [-1, 1]$. For all degrees n, $P_n(1) \equiv 1$, and for all arguments x, $P_0(x) \equiv 1$. Polynomials of different degrees are orthogonal,

$$\int_{-1}^{1} P_m(x)P_n(x)dx = \delta_{mn}\frac{2}{2n+1}, \tag{B.11}$$

and form a complete set

$$\sum_{n=0}^{\infty} \frac{2n+1}{2} P_n(x)P_n(x') = \delta(x-x'). \tag{B.12}$$

within the interval $[-1, 1]$. Additionally, Legendre polynomials are either even or odd functions:

$$P_n(-x) = (-1)^n P_n(x). \tag{B.13}$$

The second special case of (B.9) is when m and n are both integers. This first case is obviously a subset of this case. The solutions in this case are known as the associated Legendre

polynomials and can be expressed in terms of the Legendre polynomials:

$$P_l^m(x) = (-1)^m(1-x^2)^{m/2}\frac{d^m}{dx^m}P_l(x) = (-1)^m\frac{1}{2^l l!}(1-x^2)^{m/2}\frac{d^{l+m}}{dx^{l+m}}(x^2-1)^l. \tag{B.14}$$

The order m and degree l are both assumed to be non-negative integers in (B.14). Additionally, if the magnitude of m is larger than l, the polynomial P_l^m is by definition 0 for all values of its argument x. For $m < 0$, the associated Legendre polynomials are defined by their $m > 0$ counterpart:

$$P_l^{-m} = (-1)^m\frac{(l-m)!}{(l+m)!}P_l^m. \tag{B.15}$$

Unlike the Legendre polynomials, the associated Legendre polynomials do not form a complete orthogonal set. For the same order They are orthogonal in degree for the same order, i.e.

$$\int_{-1}^{1} P_{l'}^m P_l^m dx = \frac{2(l+m)!}{(2l+1)(l-m)!}\delta_{ll'}, \tag{B.16}$$

and are orthogonal in order for the same degree, i.e.

$$\int_{-1}^{1}\frac{P_l^m P_l^{m'}}{1-x^2}dx = \begin{cases} \frac{(l+m)!}{m(l-m)!}\delta_{mm'} & m \neq 0 \veebar m' \neq 0 \\ \infty & m = m' = 0 \end{cases}. \tag{B.17}$$

The associated Legendre polynomials have the parity condition

$$P_l^m(-x) = (-1)^{l+m}P_l^m(x), \tag{B.18}$$

which of course reduces to (B.13) for $m = 0$.

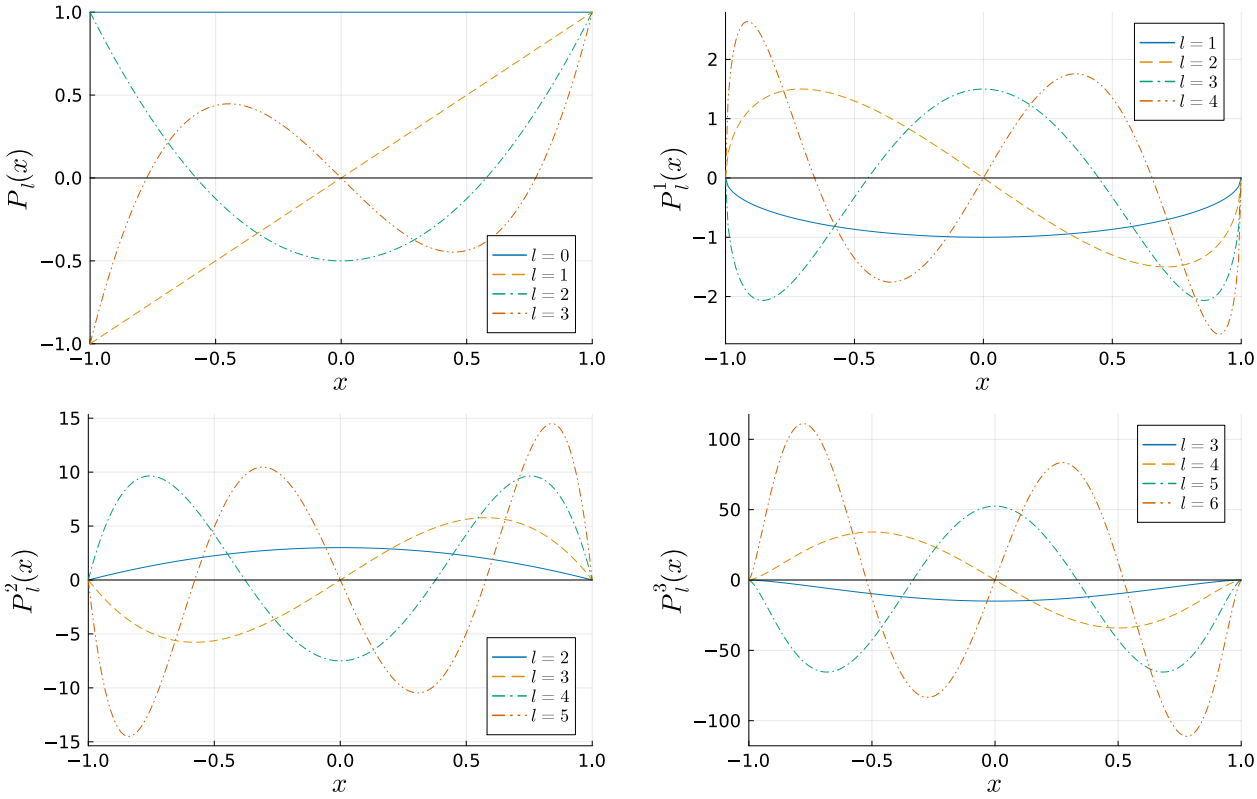

Figure B.3: Associated Legendre polynomials of order m = 0 (top left), 1 (top right), 2 (bottom left), and 3 (bottom right).

Spherical harmonics

The spherical harmonics $Y_l^\lambda(\theta, \phi)$ are the eigenfunctions of the $\widehat{z}$-component and the square of the orbital angular momentum operator:

$$L^2 Y_l^\lambda(\theta, \phi) = l(l+1) Y_l^\lambda(\theta, \phi), \tag{B.19}$$

$$L_z Y_l^\lambda(\theta, \phi) = \lambda Y_l^\lambda(\theta, \phi). \tag{B.20}$$

The spherical harmonics are defined in terms of the associated Legendre polynomials (B.14):

$$Y_l^m(\theta,\phi) = \sqrt{\frac{(2l+1)}{4\pi}\frac{(l-m)!}{(l+m)!}} P_l^\lambda(\cos\theta) e^{i\lambda\phi}. \tag{B.21}$$

The spherical harmonics form a complete, orthonormal set

$$f(\theta,\phi) = \sum_{l=0}^{\infty}\sum_{\lambda=-l}^{l} C_l^\lambda Y_l^\lambda(\theta,\phi), \tag{B.22}$$

$$\int_0^\pi \sin(\theta)d\theta \int_0^{2\pi} d\phi Y_l^\lambda(\theta,\phi) Y_{l'}^{\lambda'}(\theta,\phi). \tag{B.23}$$

Although the spherical harmonics $Y_l^\lambda(\theta,\phi)$ are in general complex, they can be transformed into real-valued spherical harmonics $Y_{l\lambda}(\theta,\phi)$ by the unitary transformation

$$\begin{pmatrix} Y_{l|\lambda|} \\ Y_{l0} \\ Y_{l-|\lambda|} \end{pmatrix} = \begin{pmatrix} (-1)^\lambda & 0 & i(-1)^\lambda \\ 0 & 1 & 0 \\ 1 & 0 & -i \end{pmatrix} \begin{pmatrix} Y_l^{|\lambda|} \\ Y_l^0 \\ Y_l^{-|\lambda|} \end{pmatrix}, \tag{B.24}$$

where the order λ is assumed to be nonzero. By definition (B.21), the spherical harmonics also obey the same parity as the associated Legendre polynomials (B.18).

Coulomb functions

The confluent hypergeometric functions are solutions to the differential equation,

$$z\frac{d^2y}{dz^2} + (b-z)\frac{dy}{dz} - ay = 0. \tag{B.25}$$

Two linearly independent solutions exist:

$$M(a,b;z) = \sum_{n=0}^{\infty} \frac{\Gamma(a+n)}{\Gamma(a)} \frac{\Gamma(b)}{\Gamma(b+n)} \frac{z^n}{n!} \tag{B.26}$$

$$U(a,b;z) = \frac{\Gamma(1-b)}{\Gamma(a+1-b)} M(a,b;z) + \frac{\Gamma(b-1)}{\Gamma(a)} z^{1-b} M(a+1-b, 2-b; z). \tag{B.27}$$

Several special cases exists where the these two solutions reduce to other familiar functions, e.g., e^z, the Laguerre polynomials, Bessel functions, Laguerre polynomials, Hermite polynomials, but they are introduced here to define the *Coulomb functions*, which solve the radial time-independent Schrödinger equation (2.6),

$$\left[-\frac{d^2}{dr^2} + \frac{l(l+1)}{r^2} + \frac{2\eta}{r} \right] y_l(r) = y_l(r), \tag{B.28}$$

which supports two linearly independent solutions, the regular (B.29) and irregular (B.30) Coulomb functions:

$$F_l(\eta, r) = 2^l e^{-\pi\eta/2} \frac{|\Gamma(l+1+i\eta)|}{(2l+1)!} e^{-ir} r^{l+1} M(l+1-i\eta, 2l+2; 2ir), \tag{B.29}$$

$$\begin{aligned} G_l(\eta, r) = {} & iF_l(\eta, r) \\ & + e^{\pi\eta/2} \frac{|\Gamma(l+1+i\eta)|}{\Gamma(l+1+i\eta)} e^{-i(r-l\pi/2)} (2ir)^{l+1} U(l+1-i\eta, 2l+2; 2ir). \end{aligned} \tag{B.30}$$

APPENDIX C: MISCELLANEOUS PROOFS, DEMONSTRATIONS

Energy normalization of radial wavefunctions

For positive energies (unbound, free particle states), a solution $\phi_l(k_i r)$ to the uncoupled radial equation (2.6) is not square-integrable over the interval $r \in (0, \infty)$. The colliding particle here is assumed to be an electrion, so m is taken to be 0. The integral $\langle \phi_l(k_i' r) | \phi_l(k_i r) \rangle$ is 0 for $k_i' = k_i$, i.e. the free-particle solutions to (2.18) are orthogonal for different energies, but diverges otherwise, which can be seen from the asymptotic behavior of the regular and irregular solutions

$$\begin{aligned} \int_{0 \ll r}^{\infty} dr\ \phi_l^{reg}(k_i' r)^* \phi_l^{reg}(k_i r) &\xrightarrow{r \to \infty} \int_{0 \ll r}^{\infty} \sin(k_i' r) \sin(k_i r) = \frac{\pi}{2} \delta(k_i' - k_i) \\ \int_{0 \ll r}^{\infty} dr\ \phi_l^{irr}(k_i' r)^* \phi_l^{irr}(k_i r) &\xrightarrow{r \to \infty} \int_{0 \ll r}^{\infty} \cos(k_i' r) \cos(k_i r) = \frac{\pi}{2} \delta(k_i' - k_i). \end{aligned} \tag{C.1}$$

The divergent part of the integrals in (C.1) is the integration from some arbitrarily large value of r, at which the regular and irregular solutions can be well described by $\sin$ and $\cos$, and determines the multiplicative factor of $\delta(k_i' - k_i)$. However, in the multichannel case, $\delta(k_i' - k_i)$ is not as useful. Looking at, for example, the regular solutions to (2.18)

$$\langle \phi_l^{reg}(k_i' r) | \phi_l^{reg}(k_i r) \rangle = \delta(k_i' - k_i) \neq \delta(k_j' - k_j) = \langle \phi_l^{reg}(k_j' r) | \phi_l^{reg}(k_j r) \rangle \,, \tag{C.2}$$

we see that normalizing each radial channel wavefunction with respect to the channel wavenumber causes the set of solutions to not be normalized at all. Instead, the radial channel wavefunctions can be normalized in energy.

For some function $f(x),\ x \in \mathbb{R}$ with a set of simple roots $\{x_i\} \subset \mathbb{R}$ such that df/dx is nonzero at every x_i, the Dirac delta function has the following property

$$\delta(f(x)) = \sum_i \delta(x - x_i) \left[\frac{df(x)}{dx} \Big|_{x_i} \right]^{-1}. \tag{C.3}$$

Using (C.3) and replacing $x \to k$, $x_i \to k'$, and $f(x) \to f(k) = E - E' = k^2/2 - k'^2/2$, we see that

$$\delta(E - E')\frac{dE}{dk} = \delta(k - k'). \tag{C.4}$$

In (C.4), we recall that we are only interested in positive energies E and use the fact that $f(k) = E - E'$ has only one zero on the open interval $k \in (0 : \infty)$. Using the relation (C.4) and orthogonality condition (C.1), we can now normalize the radial free-particle wavefunctions (2.19) in energy, which is channel independent:

$$\begin{aligned}
\left\langle \sqrt{\frac{2}{\pi k_i'}}\phi_l(k_i' r) \middle| \sqrt{\frac{2}{\pi k_i}}\phi_l(k_i r) \right\rangle &= \delta((E - E_i) - (E' - E_i)) = \delta(E - E') \\
\left\langle \sqrt{\frac{2}{\pi k_j'}}\phi_l(k_j' r) \middle| \sqrt{\frac{2}{\pi k_j}}\phi_l(k_j r) \right\rangle &= \delta((E - E_j) - (E' - E_j)) = \delta(E - E'). \qquad \text{(C.5)}
\end{aligned}$$

□

Channel wavefunctions in terms of the S-matrix

The solutions $\phi^{reg}_{E,l}(k_i r)$ and $\phi^{irr}_{E,l}(k_i r)$ are complex scalars, but solutions to the coupled radial equation (2.18) span the vector space $\mathbb{C}^{n_o}$, where n_o is the number of open channels $|ilm\rangle$ at some given total energy E. We can define several bases for this vector space, one such being the basis of regular and irregular solutions

$$B^{\phi}_{ilm} = \left\{ \phi^{100}_{ilm}(k_{i'} r),\, \phi^{11-1}_{ilm}(k_{i'} r),\, \phi^{110}_{ilm}(k_{i'} r),\, \phi^{111}_{ilm}(k_{i'} r),\, \ldots,\, \phi^{i'l'm'}_{ilm}(k_{i'} r),\, \ldots,\, \phi^{i'_{max} l'_{max} l'_{max}}_{ilm}(k_{i'} r) \right\}$$

$$\begin{aligned}
\phi^{i'l'm'}_{ilm}(k_{i'} r) &= I_{ilm,i'l'm'}\phi^{reg}_{E,l}(k_{i'} r) + K_{ilm,i'l'm'}\phi^{irr}_{E,l}(k_{i'} r), \\
\vec{\phi}_{ilm} &= \vec{\phi}^{reg}_{E,l} + \underline{K}\vec{\phi}^{irr}_{E,l}, \qquad \text{(C.6)}
\end{aligned}$$

where $\underline{I}$ is the identity matrix and $\underline{K}$ is the *reactance matrix* or K-matrix. The vectors in (C.6) are defined as

$$\vec{\phi}_{ilm} = \begin{pmatrix} \phi^{ilm}_{100}(k_1 r) \\ \vdots \\ \phi^{ilm}_{i'l'm'}(k_{i'} r) \\ \vdots \end{pmatrix}, \quad \vec{\phi}^{reg/irreg}_{E,l} = \begin{pmatrix} \phi^{reg/irreg}_{E,l}(k_1 r) \\ \vdots \\ \phi^{reg/irreg}_{E,l}(k_{i'} r) \\ \vdots \end{pmatrix}, \tag{C.7}$$

A slight change of basis, from regular and irregular solutions to free-particle incoming (-) and outgoing (+) radial waves, will allow us to define the multichannel S-matrix in terms of the multichannel K-matrix.

$$\begin{aligned} \underbrace{\phi^{irr}_{E,l}(k_j r) \pm i\, \phi^{reg}_{E,l}(k_j r)}_{\chi^{(\pm)}_{E,l}(k_j r)} &\xrightarrow{r\to\infty} \sqrt{\frac{2}{\pi k_j}} \left[\cos\left(k_j r - \frac{l\pi}{2} \right) \pm i \, \sin\left(k_j r - \frac{l\pi}{2} \right) \right] \\ \chi^{(\pm)}_{E,l}(k_j r) &\xrightarrow{r\to\infty} \sqrt{\frac{2m}{\pi k_j}} e^{\pm\left(k_j r - \frac{l\pi}{2}\right)}. \end{aligned} \tag{C.8}$$

The incoming and outgoing waves, defined in (C.8), allow us to construct the basis of incoming and outgoing waves

$$\begin{aligned} B^{\chi}_{ilm} &= \left\{ \chi^{100}_{ilm}(k^{i'} r),\, \chi^{11-1}_{ilm}(k^{i'} r),\, \chi^{110}_{ilm}(k^{i'} r),\, \chi^{111}_{ilm}(k^{i'} r),\, \ldots,\, \chi^{i'l'm'}_{ilm}(k^{i'} r),\, \ldots,\, \chi^{i'_{max} l'^{max} l'^{max}}_{ilm}(k^{i'} r) \right\} \\ \chi^{i'l'm'}_{ilm}(k_{i'} r) &= I_{ilm,i'l'm'} \chi^{(-)}_{E,l}(k_{i'} r) - S_{ilm,i'l'm'} \chi^{(+)}_{E,l}(k_{i'} r). \end{aligned} \tag{C.9}$$

We can define the S-matrix by expressing our new vector $\vec{\chi}_{ilm}$, defined in analog to (C.7), in terms

of the old vector $\vec{\phi}_{ilm}$.

$$\begin{aligned}
\vec{\chi}_{ilm} &= \vec{\chi}^{(-)}_{E,l} - \underline{S}\vec{\chi}^{(+)}_{E,l} \\
\vec{\chi}_{ilm} &= \vec{\phi}^{irr}_{E,l} - i\,\vec{\phi}^{reg}_{E,l} - \underline{S}\left(\vec{\phi}^{irr}_{E,l} + i\,\vec{\phi}^{reg}_{E,l}\right) \\
\vec{\chi}_{ilm} &= \vec{\phi}^{reg}_{E,l}(-i)\,(\underline{I}+\underline{S}) + \vec{\phi}^{irr}_{E,l}\,(\underline{I}-\underline{S}) \\
\vec{\chi}_{ilm}\,(\underline{I}+\underline{S})^{-1}\,i &= \vec{\phi}^{reg}_{E,l} + \vec{\phi}^{irr}_{E,l}\,(\underline{I}-\underline{S})\,(\underline{I}+\underline{S})^{-1}\,i. \qquad \text{(C.10)}
\end{aligned}$$

Comparing with (C.6), we can finally define the K-matrix:

$$\begin{aligned}
\underline{K} &= (\underline{I}-\underline{S})(\underline{I}+\underline{S})^{-1}i \\
-i\underline{K}(\underline{I}+\underline{S}) &= (\underline{I}-\underline{S}) \\
-i\underline{K} - i\underline{K}\underline{S} &= \underline{I}-\underline{S} \\
(\underline{I}-i\underline{K})\underline{S} &= \underline{I}+i\underline{K} \\
\underline{S} &= (\underline{I}-i\underline{K})^{-1}(I+i\underline{K}). \qquad \text{(C.11)}
\end{aligned}$$

In the case of a single elastic channel, the K-matrix was given by $\underline{K} = \tan(\delta_l)$. Making this substitution in (C.11) yields

$$\underline{S} = \frac{1+i\,\tan(\delta_l)}{(1-i\,\tan(\delta_l))} = \frac{\cos(\delta_l)+i\,\sin(\delta_l)}{\cos(\delta_l)-i\,\sin(\delta_l)} = e^{2i\delta_l}, \qquad \text{(C.12)}$$

which agrees with the single-channel definition of the S-matrix, e.g., (2.10). Expressing the K-

matrix in terms of the S-matrix (C.11) in the basis of regular and irregular solutions (C.6),

$$\begin{aligned}
\vec{\phi}_{ilm} &= \vec{\phi}^{reg}_{E,l} + \underline{K}\vec{\phi}^{irr}_{E,l}, \\
\vec{\phi}_{ilm} &= \vec{\phi}^{reg}_{E,l} + i(\underline{I}-\underline{S})(\underline{I}+\underline{S})^{-1}\vec{\phi}^{irr}_{E,l}, \\
\vec{\phi}_{ilm}(\underline{I}+\underline{S}) &= \vec{\phi}^{reg}_{E,l}(\underline{I}+\underline{S}) + i(\underline{I}-\underline{S})\vec{\phi}^{irr}_{E,l}, \\
\vec{\phi}_{ilm}(\underline{I}+\underline{S})(-i) &= \underbrace{\vec{\phi}^{irr}_{E,l} - i\vec{\phi}^{reg}_{E,l}}_{\vec{\chi}^{(-)}_{E,l}} - \underline{S}\underbrace{\left(\vec{\phi}^{irr}_{E,l} + i\vec{\phi}^{reg}_{E,l}\right)}_{\vec{\chi}^{(+)}_{E,l}}.
\end{aligned} \tag{C.13}$$

Comparing (C.13) with the incoming/outgoing radial-wave basis (C.9), we can define the basis change

$$-i\underline{U}^{\phi}(\underline{I}+\underline{S}) = \underline{U}^{\chi}, \tag{C.14}$$

where the unitary matrices $\underline{U}^{\phi}$ and $\underline{U}^{\chi}$ are built from the orthonormal bases defined in (C.6) and (C.9), respectively. The columns of $\underline{U}^{\phi}$ correspond to the vectors ϕ^{ilm}, and similarly for the columns of $\underline{U}^{\chi}$. Using the multichannel partial-wave expansion (2.17) and its asymptotic form, as well as the decomposition of an incoming plane wave into Legendre polynomials and spherical

Bessel functions (2.8),

$$
\begin{aligned}
\psi_{ii'}(\vec{r}) &= \sum_{l'=0}^{\infty}\sum_{m'=-l'}^{l'}\frac{\phi_{i'l'm'}(r)}{r}Y_{l'}^{m'}(\theta,\phi)\\
\psi_{ii'}(\vec{r}) &\xrightarrow{r\to\infty} e^{ik_iz}\delta_{ii'}+\sum_{l'=0}^{\infty}\sum_{m'=-l'}^{l'}\frac{e^{ik_{i'}r}}{r}f_{ii'}(\theta,\phi)\\
\psi_{ii'}(\vec{r}) &\xrightarrow{r\to\infty} \sum_{l=0}^{\infty}(2l+1)i^l j_l(k_ir)P_l(\cos(\theta))+\frac{e^{ik_{i'}r}}{r}\sum_{l'=0}^{\infty}\sum_{m'=-l'}^{l'}f_{ii'}(\theta,\phi)\\
\psi_{ii'}(\vec{r}) &\xrightarrow{r\to\infty} \sum_{l=0}^{\infty}(2l+1)i^l\frac{sin\left(k_ir-\frac{l\pi}{2}\right)}{k_ir}\sqrt{\frac{4\pi}{2l+1}}Y_l^0(\theta,\phi)+\frac{e^{ik_{i'}r}}{r}\sum_{l'=0}^{\infty}\sum_{m'=-l'}^{l'}f_{ii'}(\theta,\phi)\\
\psi_{ii'}(\vec{r}) &\xrightarrow{r\to\infty} \sum_{l=0}^{\infty}2\sqrt{\pi(2l+1)}i^l\frac{1}{k_ir}\frac{e^{i\left(k_ir-\frac{l\pi}{2}\right)}-e^{-i\left(k_ir-\frac{l\pi}{2}\right)}}{2i}Y_l^0(\theta,\phi)+\frac{e^{ik_{i'}r}}{r}\sum_{l'=0}^{\infty}\sum_{m'=-l'}^{l'}f_{ii'}(\theta,\phi)\\
\psi_{ii'}(\vec{r}) &\xrightarrow{r\to\infty} \sum_{l=0}^{\infty}\sqrt{\pi(2l+1)}i^{l-1}\frac{1}{k_ir}(-1)\left(e^{-i\left(k_ir-\frac{l\pi}{2}\right)}-e^{i\left(k_ir-\frac{l\pi}{2}\right)}\right)Y_l^0(\theta,\phi)\quad\cdots\\
&\cdots\quad+\frac{e^{ik_{i'}r}}{r}\sum_{l'=0}^{\infty}\sum_{m'=-l'}^{l'}f_{ii'}(\theta,\phi).
\end{aligned}
\tag{C.15}
$$

In (C.15), the first term gives us the relation between the basis vectors of U_ϕ and U_χ:

$$
\begin{aligned}
\phi_{i'l'm'}(r) &= \sum_{l=0}^{\infty}-\frac{\sqrt{\pi(2l+1)}}{k_i}i^{l-1}\sqrt{\frac{\pi k_i}{2}}\chi_{i'l'm'}^{ilm=0}(r)\\
\phi_{i'l'm'}(r) &= -\pi\sum_{l=0}^{\infty}\sqrt{\frac{2l+1}{2mk_i}}i^{l-1}\chi_{i'l'm'}^{il0}(r).
\end{aligned}
\tag{C.16}
$$

Now, using (C.16), we can obtain the asymptotic form of (2.17) in terms of the S-matrix and verify

that the behavior satisfies the boundary conditions (2.16):

$$
\begin{aligned}
\psi_{ii'}(\vec{r}) &= \sum_{l'=0}^{\infty}\sum_{m'=-l'}^{l'} \frac{\phi_{i'l'm'}(r)}{r} Y_{l'}^{m'}(\theta,\phi) = -\pi \sum_{l=0}^{\infty}\sum_{l'=0}^{\infty}\sum_{m'=-l'}^{l'} \sqrt{\frac{2l+1}{2mk_i}}\chi^{il0}_{i'l'm'}(r) i^{l-1} Y_{l'}^{m'}(\theta,\phi) \\
\psi_{ii'}(\vec{r}) &\xrightarrow{r\to\infty} \sum_{ll'm'} \sqrt{\frac{2l+1}{2mk_i}}\frac{\pi}{r} i^{l-1} Y_{l'}^{m'}(\theta,\phi) \sqrt{\frac{2m}{k_{i'}r^2\pi}} \left(S_{il0,i'l'm'} e^{i\left(k_{i'}r - \frac{l\pi}{2}\right)} - \delta_{ii'}\delta_{ll'}\delta_{0m'} e^{-i\left(k_{i'}r-\frac{l\pi}{2}\right)} \right) \\
&\xrightarrow{r\to\infty} \sum_{ll'm'} \sqrt{\frac{\pi(2l+1)}{k_i k_{i'}}} Y_{l'}^{m'}(\theta,\phi) \frac{i^{l-1}}{r} \Bigg[S_{il0,i'l'm'} e^{i\left(k_{i'}r-\frac{l\pi}{2}\right)} - \delta_{ii'}\delta_{ll'}\delta_{0m'} e^{-i\left(k_{i'}r-\frac{l\pi}{2}\right)} \quad \cdots \\
&\quad \cdots \quad + 2i\,\delta_{ii'}\delta_{ll'}\delta_{0m'} \sin\left(k_{i'}r - \frac{l\pi}{2}\right) - 2i\,\delta_{ii'}\delta_{ll'}\delta_{0m'} \sin\left(k_{i'}r - \frac{l\pi}{2}\right) \Bigg] \\
&\xrightarrow{r\to\infty} \sum_{l} \sqrt{\frac{\pi(2l+1)}{k_i^2}} Y_l^0(\theta,\phi) 2i^l \frac{\sin(k_i r - \frac{l\pi}{2})}{k_i r} \quad \cdots \\
&\quad \cdots \quad + \sum_{ll'm'} \sqrt{\frac{\pi(2l+1)}{k_i k_{i'}}} Y_{l'}^{m'}(\theta,\phi) i^{l-1} \frac{e^{ik_{i'}r}}{r} e^{-\frac{l\pi}{2}} \quad \cdots (S_{il0,i'l'm'} - \delta_{ii'}\delta_{ll'}\delta_{0m'}) \\
&\xrightarrow{r\to\infty} e^{ik_i z} + \frac{e^{ik_{i'}r}}{r} \sum_{ll'm'} \sqrt{\frac{\pi(2l+1)}{k_i k_{i'}}} Y_{l'}^{m'}(\theta,\phi) i^{l-l'-1} \left(S_{il0,i'l'm'} - \delta_{ii'}\delta_{ll'}\delta_{0m'}\right). \qquad \text{(C.17)}
\end{aligned}
$$

□

Using $S^{\ddagger}$ in lieu of $S^{\dagger}$: the ‡-norm

In the DR method presented in this dissertation, the vibrational frame transformation (2.80) is carried out on the electronic S-matrix (2.78) to obtain the two vibronic S-matrices $\underline{S}^{\Lambda}$ (4.14) and $\underline{S}^{\Lambda\ddagger}$ (4.15). The need for this second matrix and the reason why the usual Hermitian adjoint of the first vibronic S-matrix is insufficient are shown below.

Proof. The first step is to define the bases in use during the vibrational frame transformation. The basis of electronic channels is enumerated by the quantum numbers n, l, and λ: $\{|nl\lambda\rangle\}$. The basis of vibronic channels is enumerated by the quantum numbers n, v, l, and λ and is constructed as the Kronecker products of vectors from the electronic basis $\{|nl\lambda\rangle\}$ and vectors from the vibrational

basis $\{|v\rangle\}$:

$$|nvl\lambda\rangle = |nl\lambda\rangle \otimes |v\rangle\,, \tag{C.18}$$

$$\underline{I}_{nvl\lambda} = \underline{I}_{nl\lambda} \otimes \underline{I}_v. \tag{C.19}$$

$\underline{I}_v$, $\underline{I}_{nl\lambda}$, and $\underline{I}_{nvl\lambda}$ are the identity matrices in the above-mentioned bases. To make the following notation more concise, let:

- $\underline{S}_e$ denote the unitary R-dependent electronic S-matrix (2.78),
- $\underline{S}_{ve}$ denote the vibronic S-matrix (4.14),
- $\underline{S}^\dagger_{ve}$ denote the Hermitian adjoint vibronic S-matrix (4.14),
- $\underline{S}^\ddagger_{ve}$ denote the second vibronic S-matrix (4.15).

An additional distinction is needed in the following. $|\alpha\rangle = |\alpha)$ will denote a column vector in the basis denoted by α. These two ket vector quantities are the same, but a difference arises in their bra counterparts:

$$|\alpha)^\top = (\alpha| \neq (\alpha|^* = \langle\alpha| = |\alpha\rangle^\dagger\,, \tag{C.20}$$

$$(n'v'l'\lambda'|nvl\lambda) = \int dR \phi_{n'v'}(R)\phi_{nv}(R) \neq \int dR \phi^*_{n'v'}(R)\phi_{nv}(R) = \langle n'v'l'\lambda'|nvl\lambda\rangle\,. \tag{C.21}$$

With the above in mind, we can re-examine the vibronic S-matrix (4.14) obtained from the vibrational frame transformation (2.80). To further compress notation, different Greek letters will

be used to represent some combination of vibronic quantum numbers, e.g., $|\alpha) \equiv |nvl\lambda\rangle$.

$$
\begin{aligned}
\underline{S}_{ve} &= \sum_{\alpha\beta} |\alpha)\,(\alpha|\underline{S}_e\otimes\underline{I}_v|\beta)\,(\beta| \quad \underline{S}^{\ddagger}_{ve} = \sum_{\alpha\beta} |\alpha)\,(\alpha|\underline{S}^{\dagger}_e\otimes\underline{I}_v|\beta)\,(\beta|\,, \\
\underline{S}_{ve}\underline{S}^{\ddagger}_{ve} &= \left(\sum_{\alpha\beta} |\alpha)\,(\alpha|\underline{S}_e\otimes\underline{I}_v|\beta)\,(\beta|\right)\left(\sum_{\zeta\eta} |\zeta)\,(\zeta|\underline{S}^{\dagger}_e\otimes\underline{I}_v|\eta)\,(\eta|\right) \\
&= \sum_{\alpha\beta\zeta\eta} |\alpha)\,(\alpha|\underline{S}_e\otimes\underline{I}_v|\beta)\,(\beta|\,|\zeta)\,(\zeta|\underline{S}^{\dagger}_e\otimes\underline{I}_v|\eta)\,(\eta| \\
&= \sum_{\alpha\beta\eta} |\alpha)\,(\alpha|\underline{S}_e\otimes\underline{I}_v|\beta)\,(\beta|\underline{S}^{\dagger}_e\otimes\underline{I}_v|\eta)\,(\eta| \quad \Longleftarrow \quad (\beta|\zeta) = \delta_{\beta\zeta} \\
&= \sum_{\alpha\eta} |\alpha)\,(\alpha|\,(\underline{S}_e\otimes\underline{I}_v)\left(\underline{S}^{\dagger}_e\otimes\underline{I}_v\right)|\eta)\,(\eta| \quad \Longleftarrow \quad \sum_{\beta} |\beta)\,(\beta| = \underline{I}_{nvl\lambda} \\
&= \sum_{\alpha\eta} |\alpha)\,(\alpha|\left(\underline{S}_e\underline{S}^{\dagger}_e\right)\otimes(\underline{I}_v\underline{I}_v)\,|\eta)\,(\eta| \quad \Longleftarrow \quad (\underline{A}\otimes\underline{B})(\underline{C}\otimes\underline{D}) = (\underline{AC})\otimes(\underline{BD}) \\
&= \sum_{\alpha\eta} |\alpha)\,(\alpha|\underline{I}_{nl\lambda}\otimes\underline{I}_v|\eta)\,(\eta| = \sum_{\alpha\eta} (\alpha|\underline{I}_{nvl\lambda}|\eta) \quad \Longleftarrow \quad \text{(C.19)} \\
\underline{S}_{ve}\underline{S}^{\ddagger}_{ve} &= \underline{I}_{nvl\lambda}.
\end{aligned}
\tag{C.22}
$$

However, the above steps do not, in general, result in the identity matrix for the Hermitian adjoint of the vibronic S-matrix:

$$
\begin{aligned}
\underline{S}_{ve} &= \sum_{\alpha\beta} |\alpha\rangle\,\langle\alpha|\underline{S}_e\otimes\underline{I}_v|\beta\rangle\,\langle\beta| \quad \underline{S}^{\ddagger}_{ve} = \sum_{\alpha\beta} |\alpha\rangle\,\langle\alpha|\underline{S}^{\dagger}_e\otimes\underline{I}_v|\beta\rangle\,\langle\beta|\,, \\
\underline{S}_{ve}\underline{S}^{\ddagger}_{ve} &= \left(\sum_{\alpha\beta} |\alpha\rangle\,\langle\alpha|\underline{S}_e\otimes\underline{I}_v|\beta\rangle\,\langle\beta|\right)\left(\sum_{\zeta\eta} |\zeta\rangle\,\langle\zeta|\underline{S}^{\dagger}_e\otimes\underline{I}_v|\eta\rangle\,\langle\eta|\right) \\
&= \sum_{\alpha\beta\zeta\eta} |\alpha\rangle\,\langle\alpha|\underline{S}_e\otimes\underline{I}_v|\beta\rangle\,\langle\beta|\,|\zeta\rangle\,\langle\zeta|\underline{S}^{\dagger}_e\otimes\underline{I}_v|\eta\rangle\,\langle\zeta| \\
&\neq \sum_{\alpha\beta\eta} |\alpha\rangle\,\langle\alpha|\underline{S}_e\otimes\underline{I}_v|\beta\rangle\,\langle\beta|\underline{S}^{\dagger}_e\otimes\underline{I}_v|\eta\rangle\,\langle\beta| \quad \Longleftarrow \quad \langle\beta|\zeta\rangle \neq \delta_{\beta\zeta}
\end{aligned}
\tag{C.23}
$$

The unitarity of the vibronic S-matrix, therefore, cannot be defined by its usual Hermitian adjoint, but instead by its double-dagger counterpart (4.15). □

This double-dagger matrix defines the norm $\|\underline{S}\|_{\ddagger}$, which will be referred to as the ‡-norm. The ‡-norm has the same properties as the spectral norm,

$$\|\underline{A}\|_2 = \sqrt{\lambda_{\max}(\underline{A}\underline{A}^{\dagger})} = \sigma_{\max}(\underline{A}), \tag{C.24}$$

$$\|\underline{A}\|_{\ddagger} = \sqrt{\lambda_{\max}(\underline{A}\underline{A}^{\ddagger})} = \sigma_{\max}(\underline{A}), \tag{C.25}$$

where $\underline{A}$ is some square matrix, $\lambda_{\max}(\underline{A})$ is the largest eigenvalue of a matrix $\underline{A}$, and $\sigma_{\max}(\underline{A})$ is the largest singular value of a matrix $\underline{A}$. The ‡-norm is the same

The above proof hinges on the assumption that the vibronic basis is complete, which would require an infinite number of channels. In practice, of course, this is not achievable. This implies that the vibronic S-matrix is slightly sub-unitary, i.e. $\left\|\underline{S}^{\ddagger}_{ev}\right\|_{\ddagger} < \|\underline{I}_{nvl\lambda}\|_{\ddagger} = \|\underline{I}_{nvl\lambda}\|_2 = 1$. The norm $\|\cdot\|_{\ddagger}$ is similar to the spectral norm, $\|\underline{A}\|_2 = \lambda_{\max}\left(\underline{A}^{\dagger}\underline{A}\right)$, except that the Hermitian adjoint is replaced by the double-daggered matrix, i.e. The spectral norm of a matrix $\underline{A}$ is equal to its largest singular value, $\sigma_{\max}\left(\underline{A}\right)$. Because matrix transposition and element-wise conjugation do not affect the singular values of a matrix, the norm $\|\cdot\|_{\ddagger}$ is then equivalent to the norm $\|\cdot\|_2$. The vibronic S-matrix is subunitary for two reasons: the loss of flux from the continuum states obtained with the CAP (4.11) and the incomplete basis. However, a large enough number of vibrational levels in each electronic state can be used to approach completeness, which can usually be accomplished by including all bound vibrational levels in each electronic states. Additionally, there is no significant distinction between $S^{\dagger}_{ev}$ and $S_{ev^{\ddagger}}$ if we consider only the sub-blocks corresponding to bound states. Their energies and wavefunctions are real, which implies that $\langle nvl\lambda| = \langle nvl\lambda|$, therefore the two matrices are equivalent (assuming, of course, that the vibronic basis is complete).

Finiteness of the MQDT closed-channel elimination procedure

The MQDT closed-channel elimination procedure applied on the S-matrix after the (ro)vibrational frame transformation (4.25, 4.26) is guaranteed to produce a matrix that is not superunitary, i.e. it

is subunitary or unitary at most. This condition is ensured by the non-superunitarity of the frame-transformed S-matrix. In what follows, S will denote the full frame transformed S-matrix that has been partitioned into blocks according to (4.21). S could be either vibronically or rovibronically resolved.

Proof. The first proposition is that the matrix $\underline{S}_{cc} - e^{-2i\underline{\beta}}$ is not singular. Unitarity of the matrix S is defined here with respect to the norm $\|\cdot\|_{\ddagger}$ (C.25), which is equal to the largest singular value of S. The determinant of a matrix is equal to the product of its diagonal elements. Because the S-matrix is unitary, the diagonal elements of the matrix $\underline{S}_{cc} - e^{-2i\underline{\beta}}$ are never 0, unless there are closed channels that are completely decoupled from the others, which is not the case in our calculations. The magnitude of the diagonal elements of $\underline{S}_{cc}$ are strictly less than 1, while the magnitude of the diagonal elements of $e^{-2i\underline{\beta}}$ are at least 1. The sum of two complex quantities of different magnitudes will never be zero. The channel energies in the definition of $\underline{\beta}$ are real or complex. In the case that they are real, the diagonal elements of $e^{-2i\underline{beta}}$ have unitary magnitude. In the case that they are complex, we consider that the channel energies are negative by (4.12). Considering that the square root of a complex number preserves the sign of the imaginary part and that the reciprocal of a complex number changes the sign on its imaginary part, the diagonal elements of $e^{-2i\underline{\beta}}$ must have at least unitary magnitude:

$$\left|e^{-2i\beta_{kk}}\right| = \left|e^{-2i\pi/\sqrt{E_k - E}}\right| = \left|e^{-ia}e^{b}\right| > 1, \quad a, b \in \mathbb{R}, a \geq 0, b > 0. \tag{C.26}$$

n_c is the number of closed channels. The determinant of a matrix being 0 is equivalent to the matrix being singular. Given that $\left|e^{-2i\underline{\beta}}\right| \neq 0$, $e^{-2i\underline{\beta}}$ is not singular and is therefore invertible. A matrix is singular if at least one of its singular values is 0, which implies that all singular values of $e^{-2i\underline{\beta}}$ are greater than 0.

The spectral norm of a block matrix is equal to the spectral norm of its matricial norm (see Theorem 1 (f) in the work of Smoktunowicz [122]). Replacing the spectral norm ($\|\cdot\|_2$) with the norm

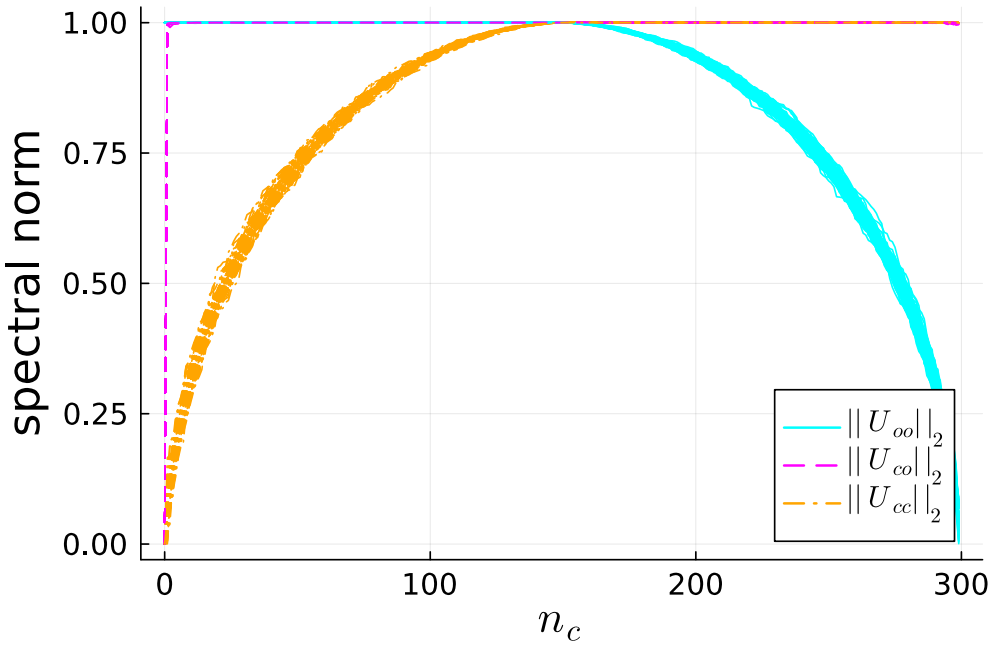

Figure C.1: Spectral norms of the subblocks of 100 random 300×300 unitary matrices U, partitioned as in (4.21) as a function of the number of closed channels, n_c. The norms of U_{oc} and U_{cc} are not defined for $n_c = 0$; the norms of U_{oo} and U_{co} are not defined for $n_o = 0$. In this figure, $n_o + n_c = 300$

$\|\cdot\|_\ddagger$,

$$\|\underline{S}\|_\ddagger = \left\| \begin{matrix} \underline{S}_{oo} & \underline{S}_{oc} \\ \underline{S}_{co} & \underline{S}_{cc} \end{matrix} \right\|_\ddagger = \left\| \begin{matrix} \|\underline{S}_{oo}\|_\ddagger & \|\underline{S}_{oc}\|_\ddagger \\ \|\underline{S}_{co}\|_\ddagger & \|\underline{S}_{cc}\|_\ddagger \end{matrix} \right\|_\ddagger \leq 1, \tag{C.27}$$

we can place some constraints on the norms of the sub-blocks of $\underline{S}$, which is illustrated by Figure C.1. The sub-blocks $\underline{S}_{co}$ and $\underline{S}_{oc}$ are equal because the S-matrix is symmetric, so their norms are

the same. Considering again (4.25, 4.26),

$$\underline{S}^{phys} = \underline{S}_{oo} - \underline{S}_{oc}\left(\underline{S}_{cc} - e^{-2i\beta}\right)^{-1}\underline{S}_{co}, \quad \text{where } \underline{S} = \begin{pmatrix} \underline{S}_{oo} & \underline{S}_{oc} \\ \underline{S}_{co} & \underline{S}_{cc} \end{pmatrix}$$

$$\begin{aligned} \left\|\underline{S}^{phys}\right\|_{\ddagger} &= \left\|\underline{S}_{oo} - \underline{S}_{oc}\left(\underline{S}_{cc} - e^{-2i\beta}\right)^{-1}\underline{S}_{co}\right\|_2 \\ &\leq \|\underline{S}_{oo}\|_{\ddagger} + \left\|\underline{S}_{oc}\left(\underline{S}_{cc} - e^{-2i\underline{\beta}}\right)^{-1}\underline{S}_{co}\right\|_{\ddagger} \iff \|\underline{A}+\underline{B}\|_{\ddagger} \leq \|\underline{A}\|_{\ddagger} + \|\underline{B}\|_{\ddagger} \\ &\leq \|\underline{S}_{oo}\|_{\ddagger} + \|\underline{S}_{oc}\|_{\ddagger}\|\underline{S}_{cc}\|_{\ddagger}\left\|\left(\underline{S}_{cc} - e^{-2i\underline{\beta}}\right)^{-1}\right\|_{\ddagger}\|\underline{S}_{co}\|_{\ddagger} \iff \|\underline{AB}\|_{\ddagger} \leq \|\underline{A}\|_{\ddagger}\|\underline{B}\|_{\ddagger} \end{aligned} \tag{C.28}$$

The spectral norm of a matrix is equal to its largest singular value, so the spectral norm of the inverse of a matrix is equal to the reciprocal of the smallest singular value of the matrix,

$$\|\underline{A}\|_{\ddagger} = \sigma_{\max}(\underline{A}), \quad \left\|\underline{A}^{-1}\right\|_{\ddagger} = \frac{1}{\sigma_{min}(\underline{A})}, \tag{C.29}$$

which implies that $\left\|\left(\underline{S}_{cc} - e^{-2i\underline{\beta}}\right)^{-1}\right\|_{\ddagger}$ is greater than 0 (invertible) and bounded above. This, coupled with the fact that the norm of the sub-blocks of $\underline{S}$ are all at most 1, implies that $\left\|\underline{S}^{phys}\right\|_{\ddagger}$ does not diverge. □

REFERENCES

[1] Christopher F McKee and Eve C Ostriker. Theory of star formation. *Annual Review of Astronomy and Astrophysics*, 45:565–687, 2007.

[2] Marco Padovani, Alexei V Ivlev, Daniele Galli, Stella SR Offner, Nick Indriolo, Donna Rodgers-Lee, Alexandre Marcowith, Philipp Girichidis, Andrei M Bykov, and JM Kruijssen. Impact of low-energy cosmic rays on star formation. *Space Science Reviews*, 216(2): 1–57, 2020.

[3] Mark R Krumholz. The big problems in star formation: the star formation rate, stellar clustering, and the initial mass function. *Physics Reports*, 539(2):49–134, 2014.

[4] Maryvonne Gerin, David A. Neufeld, and Javier R. Goicoechea. Interstellar hydrides. *Annual Review of Astronomy and Astrophysics*, 54(1):181–225, sep 2016.

[5] J Michael Shull, Charles W Danforth, and Katherine L Anderson. A far ultraviolet spectroscopic explorer survey of interstellar molecular hydrogen in the galactic disk. *The Astrophysical Journal*, 911(1):55, 2021.

[6] P Sonnentrucker, Mark Wolfire, David A Neufeld, Nicolas Flagey, Maryvonne Gerin, P Goldsmith, Darek Lis, and Raquel Monje. A herschel/hifi legacy survey of HF and H_2O in the galaxy: Probing diffuse molecular cloud chemistry. *The Astrophysical Journal*, 806 (1):49, 2015.

[7] Maryvonne Gerin, H Liszt, D Neufeld, B Godard, P Sonnentrucker, J Pety, and E Roueff. Molecular ion abundances in the diffuse ISM: CF^+, HCO^+, HOC^+, and C_3H^+. *Astronomy & Astrophysics*, 622:A26, 2019.

[8] Eric Herbst. Molecular ions in interstellar reaction networks. In *Journal of Physics: Conference Series*, volume 4, page 17. IOP Publishing, 2005.

[9] P. Thaddeus, C. A. Gottlieb, H. Gupta, S. Brünken, M. C. McCarthy, M. Agúndez, M. Guélin, and J. Cernicharo. Laboratory and astronomical detection of the negative molecular ion C_3N^-. *Astrophys. J.*, 677(2):1132–1139, apr 2008. doi: 10.1086/528947.

[10] J. Cernicharo, M. Guélin, M. Agúndez, K. Kawaguchi, M. McCarthy, and P. Thaddeus. Astronomical detection of C_4H^-, the second interstellar anion. *Astron. Astrophys.*, 467(2): L37–L40, 2007. doi: 10.1051/0004-6361:20077415.

[11] J. Cernicharo, M. Guélin, M. Agúndez, M. C. McCarthy, and P. Thaddeus. Detection of C_5N^- and vibrationally excited C_6H in IRC +10216. *Astrophys. J.*, 688(2):L83, 2008. doi: 10.1086/595583.

[12] J Cernicharo, JR Pardo, C Cabezas, M Agúndez, B Tercero, N Marcelino, R Fuentetaja, M Guélin, and P de Vicente. Discovery of the C_7N^-anion in TMC-1 and IRC+ 10216. *arXiv preprint arXiv:2301.12819*, 2023.

[13] M. C. McCarthy, C. A. Gottlieb, H. Gupta, and P. Thaddeus. Laboratory and astronomical identification of the negative molecular ion C_6H^-. *Astrophys. J.*, 652(2):L141, 2006. doi: 10.1086/510238.

[14] S. Brünken, H. Gupta, C. A. Gottlieb, M. C. McCarthy, and P. Thaddeus. Detection of the carbon chain negative ion C_8H^- in TMC-1. *Astrophys. J.*, 664(1):L43, 2007. doi: 10.1086/520703.

[15] Anthony Remijan, Haley N Scolati, Andrew M Burkhardt, P Bryan Changala, Steven B Charnley, Ilsa R Cooke, Martin A Cordiner, Harshal Gupta, Eric Herbst, Kin Long Kelvin Lee, et al. Astronomical detection of the interstellar anion $C_{10}H^-$ toward TMC-1 from the

GOTHAM large program on the green bank telescope. *The Astrophysical Journal Letters*, 944(2):L45, 2023.

[16] Eric Herbst. Can negative molecular ions be detected in dense interstellar clouds? *Nature*, 289:656–657, 1981.

[17] J Fulara, D Lessen, P Freivogel, and JP Maier. Laboratory evidence for highly unsaturated hydrocarbons as carriers of some of the diffuse interstellar bands. *Nature*, 366(6454):439–441, 1993.

[18] M Tulej, DA Kirkwood, M Pachkov, and JP Maier. Gas-phase electronic transitions of carbon chain anions coinciding with diffuse interstellar bands. *The Astrophysical Journal*, 506(1):L69, 1998.

[19] Deborah P Ruffle, RPA Bettens, Radoslava Terzieva, and Eric Herbst. The abundance of C_7^- in diffuse clouds. *The Astrophysical Journal*, 523(2):678, 1999.

[20] R Terzieva and Eric Herbst. Radiative electron attachment to small linear carbon clusters and its significance for the chemistry of diffuse interstellar clouds. *International Journal of Mass Spectrometry*, 201(1-3):135–142, 2000.

[21] Brian Eichelberger, Theodore P Snow, Cynthia Barckholtz, and Veronica M Bierbaum. Reactions of H, N, and O atoms with carbon chain anions of interstellar interest: An experimental study. *The Astrophysical Journal*, 667(2):1283, 2007.

[22] Marjan Khamesian, Nicolas Douguet, Samantha Fonseca dos Santos, Olivier Dulieu, Maurice Raoult, Will J. Brigg, and Viatcheslav Kokoouline. Formation of CN^-, C_3N^-, and C_5N^- molecules by radiative electron attachment and their destruction by photodetachment. *Phys. Rev. Lett.*, 117:123001, 2016.

[23] Stephen Harrison and Jonathan Tennyson. Bound and continuum states of molecular anions C_2H^- and C_3N^-. *J. Phys. B.* , 44(4):045206, feb 2011. doi: 10.1088/0953-4075/44/4/045206.

[24] Miguel Lara-Moreno, Thierry Stoecklin, Philippe Halvick, and Jean-Christophe Loison. Single-center approach for photodetachment and radiative electron attachment: Comparison with other theoretical approaches and with experimental photodetachment data. *Phys. Rev. A*, 99:033412, Mar 2019. doi: 10.1103/PhysRevA.99.033412.

[25] Miguel Lara-Moreno, Thierry Stoecklin, and Philippe Halvick. Radiative electron attachment and photodetachment rate constants for linear carbon chains. *ACS Earth Space Chem.*, 3(8):1556–1563, 2019. doi: 10.1021/acsearthspacechem.9b00098.

[26] Malcolm Simpson, Markus Nötzold, Tim Michaelsen, Robert Wild, Franco A. Gianturco, and Roland Wester. Influence of a supercritical electric dipole moment on the photodetachment of C_3N^-. *Phys. Rev. Lett.*, 127:043001, Jul 2021. doi: 10.1103/PhysRevLett.127.043001.

[27] E. Fermi and E. Teller. The capture of negative mesotrons in matter. *Phys. Rev.*, 72:399–408, Sep 1947. doi: 10.1103/PhysRev.72.399.

[28] Cate S. Anstöter, Golda Mensa-Bonsu, Pamir Nag, Milo š Ranković, Ragesh Kumar T. P., Anton N. Boichenko, Anastasia V. Bochenkova, Juraj Fedor, and Jan R. R. Verlet. Mode-specific vibrational autodetachment following excitation of electronic resonances by electrons and photons. *Phys. Rev. Lett.*, 124:203401, May 2020. doi: 10.1103/PhysRevLett.124.203401.

[29] Elizabeth A. Brinkman, Susan Berger, Jeffrey Marks, and John I. Brauman. Molecular rotation and the observation of dipole-bound states of anions. *J. Chem. Phys.*, 99(10):7586–7594, 1993. doi: 10.1063/1.465688.

[30] David A. Walthall, Joel M. Karty, and John I. Brauman. Molecular rotations and dipole-bound state lifetimes. *J. Phys. Chem. A*, 109(39):8794–8799, 2005. doi: 10.1021/jp050025q. PMID: 16834282.

[31] Ritchie Thomson and FW Dalby. Experimental determination of the dipole moments of the X($^2\Sigma^+$) and B($^2\Sigma^+$) states of the CN molecule. *Canadian Journal of Physics*, 46(24): 2815–2819, 1968.

[32] Robert von Hahn, Arno Becker, Felix Berg, Klaus Blaum, Christian Breitenfeldt, Hisham Fadil, Florian Fellenberger, Michael Froese, Sebastian George, Jürgen Göck, et al. The cryogenic storage ring CSR. *Review of Scientific Instruments*, 87(6):063115, 2016.

[33] Oldřich Novotný, Patrick Wilhelm, Daniel Paul, Ábel Kálosi, Sunny Saurabh, Arno Becker, Klaus Blaum, Sebastian George, Jürgen Göck, Manfred Grieser, et al. Quantum-state–selective electron recombination studies suggest enhanced abundance of primordial HeH^+. *Science*, 365(6454):676–679, 2019.

[34] Nick Indriolo, David A. Neufeld, Maryvonne Gerin, Peter Schilke, Arnold O Benz, Benjamin Winkel, Karl M Menten, Edward T Chambers, John H Black, Simon Bruderer, et al. Herschel survey of galactic OH^+, H_2O^+, and H_3O^+: Probing the molecular hydrogen fraction and cosmic-ray ionization rate. *The Astrophysical Journal*, 800(1):40, 2015.

[35] H Takagi, N Kosugi, and M Le Dourneuf. Dissociative recombination of CH^+. *Journal of Physics B*, 24(3):711, 1991.

[36] Hidekazu Takagi. Rotational effects in the dissociative recombination process of H_2^+ + e. *Journal of Physics B: Atomic, Molecular and Optical Physics*, 26(24):4815, 1993.

[37] AE Douglas and G Herzberg. Note on CH^+ in interstellar space and in the laboratory. *Astrophys. J.*, 94:381, 1941.

[38] David A Neufeld, Peter Schilke, Karl M Menten, Mark G Wolfire, John H Black, Frédéric Schuller, Holger SP Müller, Sven Thorwirth, Rolf Güsten, and Sabine Philipp. Discovery of interstellar CF^+. *Astronomy & Astrophysics*, 454(2):L37–L40, 2006.

[39] Daniel Paul, Manfred Grieser, Florian Grussie, Robert von Hahn, Leonard W Isberner, Ábel Kálosi, Claude Krantz, Holger Kreckel, Damian Müll, David A Neufeld, et al. Experimental determination of the dissociative recombination rate coefficient for rotationally cold CH^+ and its implications for diffuse cloud chemistry. *The Astrophysical Journal*, 939(2):122, 2022.

[40] Roman Čurík and Chris H Greene. Inelastic low-energy collisions of electrons with HeH^+: Rovibrational excitation and dissociative recombination. *The Journal of Chemical Physics*, 147(5):054307, 2017.

[41] Roman Čurík, Dávid Hvizdoš, and Chris H Greene. Dissociative recombination of cold HeH^+ ions. *Physical Review Letters*, 124(4):043401, 2020.

[42] Edward L Hamilton and Chris H Greene. Competition among molecular fragmentation channels described with siegert channel pseudostates. *Physical Review Letters*, 89(26): 263003, 2002.

[43] Viatcheslav Kokoouline and Chris H Greene. Unified theoretical treatment of dissociative recombination of D_{3h} triatomic ions: application to $H_3{}^+$ and $D_3{}^+$. *Physical Review A*, 68(1): 012703, 2003.

[44] R Čurík and Chris H Greene. Rates for dissociative recombination of LiH^+ ions. In *Journal of Physics: Conference Series*, volume 115, page 012016. IOP Publishing, 2008.

[45] AE Orel and KC Kulander. Resonant dissociative recombination of $H_3{}^+$. *Physical review letters*, 71(26):4315, 1993.

[46] AE Orel. Time-dependent wave-packet study of the direct low-energy dissociative recombination of HD^+. *Physical Review A*, 62(2):020701, 2000.

[47] Åsa Larson and AE Orel. Wave-packet study of the products formed in dissociative recombination of HeH^+. *Physical Review A*, 72(3):032701, 2005.

[48] Sabine Morisset, Lukáš Pichl, Ann E Orel, and Ioan F Schneider. Wave-packet approach to rydberg resonances in dissociative recombination. *Physical Review A*, 76(4):042702, 2007.

[49] A Giusti-Suzor and H Lefebvre-Brion. The dissociative recombination of ch/plus/ions. *Astrophys. J.*, 214:L101–L103, 1977.

[50] A Giusti. A multichannel quantum defect approach to dissociative recombination. *J. Phys. B*, 13(19):3867, 1980.

[51] Steven L Guberman and Annick Giusti-Suzor. The generation of $O(^1S)$ from the dissociative recombination of $O_2{}^+$. *J. Chem. Phys.*, 95(4):2602–2613, 1991.

[52] Steven L Guberman. The dissociative recombination of OH^+. *The Journal of Chemical Physics*, 102(4):1699–1704, 1995.

[53] Steven L Guberman. Mechanism for the green glow of the upper ionosphere. *Science*, 278 (5341):1276–1278, 1997.

[54] L Carata, A E Orel, M Raoult, I F Schneider, and A Suzor-Weiner. Core-excited resonances in the dissociative recombination of CH^+ and CD^+. *Physical Review A*, 62(5):052711, 2000.

[55] Steven L Guberman. Role of excited core rydberg states in dissociative recombination. *J. Phys. Chem. A*, 111(44):11254–11260, 2007.

[56] Hidekazu Takagi. Cross sections of the processes induced by electron collisions with H_2^+, HeH^+, and their isotopes. *Fusion Sci. Technol.*, 63(3):406–412, 2013.

[57] K Chakrabarti, J Zs Mezei, O Motapon, A Faure, O Dulieu, K Hassouni, and IF Schneider. Dissociative recombination of the CH^+ molecular ion at low energy. *Journal of Physics B*, 51(10):104002, 2018.

[58] Xianwu Jiang, Josh Forer, Chi Hong Yuen, Mehdi Ayouz, and Viatcheslav Kokoouline. Theory of dissociative recombination of molecular ions with competing direct and indirect mechanisms applied to CH^+. *Phys. Rev. A*, 104(4):042801, 2021.

[59] Lev Davidovich Landau and Evgenii Mikhailovich Lifshitz. *Quantum mechanics: non-relativistic theory*, volume 3. Elsevier, 2013.

[60] Harald Friedrich. *Scattering theory*, volume 872. Springer, 2013.

[61] MJ Seaton. Coulomb functions for attractive and repulsive potentials and for positive and negative energies. *Computer physics communications*, 146(2):225–249, 2002.

[62] Harald Friedrich. *Theoretical atomic physics*, volume 3. Springer, 2006.

[63] Eugene P Wigner. Resonance reactions. *Phys. Rev.*, 70(9-10):606, 1946.

[64] Eugene Paul Wigner. Reaction and scattering cross-sections. *Proceedings of the National Academy of Sciences*, 32(12):302–306, 1946.

[65] MJ Seaton. Quantum defect theory I. general formulation. *Proc. Phys. Soc.*, 88(4):801, 1966.

[66] MJ Seaton. Quantum defect theory. *Rep. Prog. Phys.*, 46(2):167, 1983.

[67] MJ Seaton. The quantum defect method. *Monthly Notices of the Royal Astronomical Society*, 118(5):504–518, 1958.

[68] Leonard Rosenberg. Levinson-seaton theorem for potentials with an attractive coulomb tail. *Physical Review A*, 52(5):3824, 1995.

[69] Mireille Aymar, Chris H Greene, and Eliane Luc-Koenig. Multichannel rydberg spectroscopy of complex atoms. *Reviews of Modern Physics*, 68(4):1015, 1996.

[70] C Greene, U Fano, and G Strinati. General form of the quantum-defect theory. *Physical Review A*, 19(4):1485, 1979.

[71] MJ Seaton. Quantum defect theory II. illustrative one-channel and two-channel problems. *Proc. Phys. Soc.*, 88(4):815, 1966.

[72] Eugene P. Wigner. Resonance reactions and anomalous scattering. *Phys. Rev.*, 70:15–33, Jul 1946. doi: 10.1103/PhysRev.70.15.

[73] Eugene P. Wigner. Resonance reactions. *Phys. Rev.*, 70:606–618, Nov 1946. doi: 10.1103/PhysRev.70.606.

[74] Eugene Paul Wigner and Leonard Eisenbud. Higher angular momenta and long range interaction in resonance reactions. *Phys. Rev.*, 72(1):29, 1947.

[75] T. Teichmann and E. P. Wigner. Sum rules in the dispersion theory of nuclear reactions. *Phys. Rev.*, 87:123–135, Jul 1952. doi: 10.1103/PhysRev.87.123.

[76] Edmund Taylor Whittaker and George Neville Watson. *A course of modern analysis: an introduction to the general theory of infinite processes and of analytic functions; with an acount of the principal transcendental functions*. University Press, 1927.

[77] ES Chang and U Fano. Theory of electron-molecule collisions by frame transformations. *Phys. Rev. A*, 6(1):173, 1972.

[78] Chris H Greene and Ch Jungen. Molecular applications of quantum defect theory. *Adv. Atom. Mol. Phys.*, 21:51–121, 1985.

[79] U Fano. Quantum defect theory of l uncoupling in H_2 as an example of channel-interaction treatment. *Physical Review A*, 2(2):353, 1970.

[80] N Y Du and C H Greene. Quantum defect analysis of HD-photoionization. *J. Chem. Phys.*, 85:5430, 1986.

[81] Marjan Khamesian, Mehdi Ayouz, Jasmeet Singh, and Viatcheslav Kokoouline. Cross sections and rate coefficients for rotational excitation of HeH^+ molecule by electron impact. *Atoms*, 6(3):49, 2018.

[82] C. Desfrançois, H. Abdoul-Carime, N. Khelifa, and J. P. Schermann. From $\frac{1}{r}$ to $\frac{1}{r^2}$ potentials: Electron exchange between rydberg atoms and polar molecules. *Phys. Rev. Lett.*, 73:2436–2439, Oct 1994. doi: 10.1103/PhysRevLett.73.2436.

[83] Abdoul-Carime, H. and Desfrançois, C. Electrons weakly bound to molecules by dipolar, quadrupolar or polarization forces. *Eur. Phys. J. D*, 2(2):149–156, 1998. doi: 10.1007/s100530050124.

[84] Michael A. Morrison and Lee A. Collins. Exchange in low-energy electron-molecule scattering: Free-electron-gas model exchange potentials and applications to e – H_2 and e – N_2 collisions. *Phys. Rev. A*, 17:918–938, Mar 1978. doi: 10.1103/PhysRevA.17.918.

[85] N. T. Padial and D. W. Norcross. Parameter-free model of the correlation-polarization potential for electron-molecule collisions. *Phys. Rev. A*, 29:1742–1748, Apr 1984. doi: 10.1103/PhysRevA.29.1742.

[86] Lue-yung Chow Chiu and Mohammad Moharerrzadeh. Translational and rotational expansion of spherical gaussian wave functions for multicenter molecular integrals. *J. Chem. Phys*, 101(1):449–458, 1994. doi: 10.1063/1.468154.

[87] F A Gianturco and T Stoecklin. Electron scattering from acetylene: elastic integral and differential cross sections at low energies. *J.Phys.B.*, 27(24):5903–5921, dec 1994. doi: 10.1088/0953-4075/27/24/014.

[88] H.-J. Werner, P. J. Knowles, G. Knizia, F. R. Manby, and M. Schütz. Molpro: a general-purpose quantum chemistry program package. *WIREs Comput Mol Sci*, 2:242–253, 2012.

[89] H.-J. Werner, P. J. Knowles, P. Celani, W. Györffy, A. Hesselmann, D. Kats, G. Knizia, A. Köhn, T. Korona, D. Kreplin, R. Lindh, Q. Ma, F. R. Manby, A. Mitrushenkov, G. Rauhut, M. Schütz, K. R. Shamasundar, T. B. Adler, R. D. Amos, S. J. Bennie, A. Bernhardsson, A. Berning, J. A. Black, P. J. Bygrave, R. Cimiraglia, D. L. Cooper, D. Coughtrie, M. J. O. Deegan, A. J. Dobbyn, K. Doll, M. Dornbach, F. Eckert, S. Erfort, E. Goll, C. Hampel, G. Hetzer, J. G. Hill, M. Hodges, T. Hrenar, G. Jansen, C. Köppl, C. Kollmar, S. J. R. Lee, Y. Liu, A. W. Lloyd, R. A. Mata, A. J. May, B. Mussard, S. J. McNicholas, W. Meyer, T. F. Miller III, M. E. Mura, A. Nicklass, D. P. O'Neill, P. Palmieri, D. Peng, K. A. Peterson, K. Pflüger, R. Pitzer, I. Polyak, M. Reiher, J. O. Richardson, J. B. Robinson, B. Schröder, M. Schwilk, T. Shiozaki, M. Sibaev, H. Stoll, A. J. Stone, R. Tarroni, T. Thorsteinsson, J. Toulouse, M. Wang, M. Welborn, and B. Ziegler. Molpro, version , a package of ab initio programs. see.

[90] RW Heather and JC Light. Discrete variable theory of triatomic photodissociation. *The Journal of Chemical Physics*, 79(1):147–159, 1983.

[91] RW Heather and JC Light. Photodissociation of triatomic molecules: Rotational scattering effects[a)]. *The Journal of Chemical Physics*, 78(9):5513–5530, 1983.

[92] G Guillon and T Stoecklin. Analytical calculation of the smith lifetime Q matrix using a magnus propagator: Applications to the study of resonances occurring in ultracold inelastic

collisions with and without an applied magnetic field. *The Journal of chemical physics*, 130 (14):144306, 2009.

[93] CA Gottlieb, EW Gottlieb, P Thaddeus, and H Kawamura. Laboratory detection of the C_3N an C_4H free radicals. *Astrophys. J.*, 275:916–921, 1983.

[94] Stanka V. Jerosimić, Milan Z. Milovanović, Roland Wester, and Franco A. Gianturco. Chapter three - dipole-bound states contribution to the formation of anionic carbonitriles in the ism: Calculations using multireference methods for C_3N^-. In John R. Sabin and Jens Oddershede, editors, *Rufus Ritchie, A Gentleman and A Scholar*, volume 80 of *Advances in Quantum Chemistry*, pages 47–86. Academic Press, 2019. doi: https://doi.org/10.1016/bs.aiq.2019.06.006.

[95] M. Ayouz, R. Lopes, M. Raoult, O. Dulieu, and V. Kokoouline. Formation of H_3^- by radiative association of H_2 and H^- in the interstellar medium. *Phys. Rev. A*, 83(5):052712, 2011. doi: 10.1103/PhysRevA.83.052712.

[96] T. Stoecklin, F. Lique, and M. Hochlaf. A new theoretical method for calculating the radiative association cross section of a triatomic molecule: application to $N_2 - H^-$. *Phys. Chem. Chem. Phys.*, 15:13818–13825, 2013. doi: 10.1039/C3CP50934F.

[97] N. Douguet, S. Fonseca dos Santos, M. Raoult, O. Dulieu, Ann E. Orel, and V. Kokoouline. Theory of radiative electron attachment to molecules: Benchmark study of CN^-. *Phys. Rev. A*, 88(5):052710, 2013.

[98] Nicolas Douguet, S. Fonseca dos Santos, Maurice Raoult, Olivier Dulieu, Ann E. Orel, and Viatcheslav Kokoouline. Theoretical study of radiative electron attachment to CN, C_2H, and C_4H radicals. *J. Chem. Phys.*, 142(23):234309, 2015.

[99] F. Carelli, F. A. Gianturco, R. Wester, and M. Satta. Formation of cyanopolyyne anions

in the interstellar medium: The possible role of permanent dipoles. *J. Chem. Phys.*, 141: 054302, 2014.

[100] Joshua Forer, Viatcheslav Kokoouline, and Thierry Stoecklin. Radiative electron attachment to rotating C_3N through dipole-bound states. *Physical Review A*, 107(4):043117, 2023.

[101] Z Amitay, D Zajfman, P Forck, U Hechtfischer, B Seidel, M Grieser, D Habs, R Repnow, D Schwalm, and A Wolf. Dissociative recombination of CH^+: Cross section and final states. *Phys. Rev. A*, 54(5):4032, 1996.

[102] A Vibok and GG Balint-Kurti. Parametrization of complex absorbing potentials for time-dependent quantum dynamics. *J. Phys. Chem.*, 96(22):8712–8719, 1992.

[103] S. Fonseca dos Santos, V. Kokoouline, and C. H. Greene. Dissociative recombination of H_3^+ in the ground and excited vibrational states. *J. Chem. Phys.*, 127:124309, 2007.

[104] J. M. Carr, P. G. Galiatsatos, J. D. Gorfinkiel, A. G. Harvey, M. A. Lysaght, D. Madden, Z. Mašín, M. Plummer, J. Tennyson, and H. N. Varambhia. Ukrmol: a low-energy electron- and positron-molecule scattering suite. *The European Physical Journal D*, 66(3):58, Mar 2012. ISSN 1434-6079. doi: 10.1140/epjd/e2011-20653-6.

[105] Jonathan Tennyson and Cliff J. Noble. Reson—a program for the detection and fitting of breit-wigner resonances. *Computer Physics Communications*, 33(4):421–424, 1984. ISSN 0010-4655. doi: https://doi.org/10.1016/0010-4655(84)90147-4.

[106] Jonathan Tennyson, Daniel B Brown, James J Munro, Iryna Rozum, Hemal N Varambhia, and Natalia Vinci. Quantemol-N: an expert system for performing electron molecule collision calculations using the R-matrix method. *Journal of Physics: Conference Series*, 86(1): 012001, oct 2007. doi: 10.1088/1742-6596/86/1/012001.

[107] O Novotný, O Motapon, Max H Berg, D Bing, H Buhr, H Fadil, M Grieser, J Hoffmann, AS Jaroshevich, B Jordon-Thaden, C Krantz, M Lange, M Lestinsky, M Mendes, S Novotný, D A Orlov, A Petrignani, I F Schneider, A Orel, and A Wolf. Dissociative recombination of cf+: Experiment and theory. *J. Phys. Conf. Ser.*, 192:012021, 2009.

[108] Jonathan Tennyson. Electron–molecule collision calculations using the R-matrix method. *Physics Reports*, 491(2):29–76, 2010. ISSN 0370-1573. doi: https://doi.org/10.1016/j.physrep.2010.02.001.

[109] PM Mul, JBA Mitchell, VS D'Angelo, P Defrance, J Wm McGowan, and HR Froelich. Merged electron-ion beam experiments. IV. dissociative recombination for the methane group CH^+,..., CH_5^+. *J. Phys. B: At. Mol. Phys.*, 14(8):1353, 1981.

[110] Zsolt J Mezei, Michel D Epée Epée, Ousmanou Motapon, and Ioan F Schneider. Dissociative recombination of CH^+ molecular ion induced by very low energy electrons. *Atoms*, 7 (3):82, 2019.

[111] RF Boĭkova et al. Rotational and vibrational excitation of molecular ions by electrons. *Soviet Journal of Experimental and Theoretical Physics*, 27:772, 1968.

[112] M Gailitis. New forms of asymptotic expansions for wavefunctions of charged-particle scattering. *J. Phys. B*, 9(5):843, 1976.

[113] Shih-I Chu and A. Dalgarno. Rotational excitation of CH^+ by electron impact. *Phys. Rev. A*, 10:788–792, Sep 1974. doi: 10.1103/PhysRevA.10.788.

[114] Ismanuel Rabadán and Jonathan Tennyson. Rotions: A program for the calculation of rotational excitation cross sections in electron—molecular ion collisions. *Computer physics communications*, 114(1-3):129–141, 1998.

[115] Xianwu Jiang, Chi Hong Yuen, Pietro Cortona, Mehdi Ayouz, and Viatcheslav Kokoouline. Cross sections for vibronic excitation of CH^+ by low-energy electron impact. *Physical Review A*, 100(6):062711, 2019.

[116] James R Hamilton, Alexandre Faure, and Jonathan Tennyson. Electron-impact excitation of diatomic hydride cations–I. HeH^+, CH^+, ArH^+. *Monthly Notices of the Royal Astronomical Society*, 455(3):3281–3287, 2016.

[117] Ábel Kálosi, Manfred Grieser, Robert von Hahn, Ulrich Hechtfischer, Claude Krantz, Holger Kreckel, Damian Müll, Daniel Paul, Daniel W Savin, Patrick Wilhelm, Andreas Wolf, Mark G. Wolfire, and Oldrich Novotný. Laser probing of the rotational cooling of molecular ions by electron collisions. *Phys. Rev. Lett.*, 128(18):183402, 2022.

[118] Joshua Forer, Dávid Hvizdoš, Xianwu Jiang, Mehdi Ayouz, Chris H Greene, and Viatcheslav Kokoouline. Unified treatment of resonant and nonresonant mechanisms in dissociative recombination: Benchmark study of CH^+. *Physical Review A*, 107(4):042801, 2023.

[119] Joshua Forer, Dávid Hvizdoš, Mehdi Ayouz, Chris H Greene, and Viatcheslav Kokoouline. Kinetic rate coefficients for electron-driven collisions with CH^+: dissociative recombination and rovibronic excitation. *arXiv preprint arXiv:2309.14370*, 2023.

[120] Yuan Liu, Guo-Zhu Zhu, Dao-Fu Yuan, Chen-Hui Qian, Yue-Rou Zhang, Brenda M Rubenstein, and Lai-Sheng Wang. Observation of a symmetry-forbidden excited quadrupole-bound state. *J. Am. Chem. Soc.*, 142(47):20240–20246, 2020.

[121] Daniel J Haxton and Chris H Greene. Ab initio frame-transformation calculations of direct and indirect dissociative recombination rates of $HeH^+ + e^-$. *Phys. Rev. A*, 79(2):022701, 2009.

[122] Alicja Smoktunowicz. Block matrices and symmetric perturbations. *Linear algebra and its applications*, 429(10):2628–2635, 2008.